

# UC Berkeley

## UC Berkeley Electronic Theses and Dissertations

### Title

Explorations of Novel Energy Conversion and Storage Systems

### Permalink

<https://escholarship.org/uc/item/9dq8j6zb>

### Author

Duffin, Andrew Mark

### Publication Date

2010

Peer reviewed|Thesis/dissertation

Explorations of Novel Energy Conversion and Storage Systems

By

Andrew Mark Duffin

A dissertation submitted in partial satisfaction of the

requirements for the degree of

Doctor of Philosophy

in

Chemistry

in the Graduate Division

of the

University of California, Berkeley

Committee in charge:

Professor Richard J. Saykally, Chair

Professor Gabor Somorjai

Professor Dorian Liepmann

Fall 2010



## Abstract

### Explorations of Novel Energy Conversion and Storage Systems

by

Andrew Mark Duffin

Doctor of Philosophy in Chemistry

University of California, Berkeley

Professor Richard Saykally, Chair

At present, the majority of the world's energy demand is met by the consumption of exhaustible fuel supplies. Consequently, it is urgent to research and develop viable alternatives. In this dissertation, I present research that addresses fundamental questions concerning how water interacts with surfaces and solutes, with the goal of identifying novel systems for energy production and storage.

Electrokinetic currents are created when moving fluid entrains charge from the diffuse portion of an electric double layer and carries that charge downstream. The potential difference that develops on either end of the channel is known as the streaming potential. Chapter 2 of this dissertation focuses on electrokinetic energy production and conversion efficiency of liquid microjets. Section 1 of Chapter 2 presents proof-of-principle research demonstrating that molecular hydrogen is generated from electrokinetic currents in liquid water microjets. Hydrogen is generated when hydrated protons are preferentially carried downstream and recombine with electrons at a grounded target electrode. Both the current and hydrogen production scale nearly quadratically with flow rate, as predicted by equations derived from simple double layer theory and fluid mechanics. The efficiency is currently very low (ca  $10^{-6}$ ) and is limited by the low electrokinetic current ( $\sim$ nA). Designs to improve this efficiency are considered.

Rather than chemical conversion efficiency, Section 2 of Chapter 2 investigates the electrical conversion efficiency of liquid water microjets. Typical electrokinetic energy conversion schemes measure current or voltage via electrodes in the fluid reservoirs on either side of a channel. With this design, the streaming potential drives a current against the flow of the fluid and, consequently, limits the conversion efficiency. In contrast, liquid microjets break up into droplets before reaching the downstream electrode and this eliminates the possibility for back conduction. As a result, liquid microjets yield conversion efficiencies exceeding 10%, much larger than channel-dependent measurements ( $\sim$ 3%).

It is the large potentials obtainable with electrokinetic currents (tens of kilovolts) that drive up the electrical conversion efficiency. Unfortunately, low currents with high

voltages are inconvenient for application. Section 3 of Chapter 2 describes efforts to utilize the high voltage of electrokinetic currents by coupling light into the process. More specifically, the streaming potential is used to modify the space charge layer in a semiconductor and, consequently, the light harvesting characteristics of that semiconductor. To this end, microchannel jets fabricated out of glass and silicon were built to allow light to impinge on the current generating surface. Although plagued with inconsistent results, streaming currents were found to increase upon illumination and some channels even gave measurable responses to ambient room lights.

Chapter 3 of this dissertation addresses the details of hydration of boron-oxides and sodium borohydride as studied by near edge x-ray absorption fine structure spectroscopy (NEXAFS) and associated theory. Boron-oxides and molecular hydrogen are products of borohydride hydrolysis which has been intensely studied for hydrogen storage purposes. In spite of their hydroxide moieties, boron-oxides turn out to not be strongly hydrated by water. The experimental spectra, as well as attending calculations, show no evidence for electronic coupling that would indicate strong hydrogen bonding between the boron-oxides and water. On the other hand, the NEXAFS spectrum of sodium borohydride is significantly altered by water. The experiment and calculations show strong evidence for short dihydrogen bonds between water hydrogens and borohydride hydrogens. Molecular dynamics simulations indicate that borohydride is hydrated at the tetrahedral corners and edge.

## **Acknowledgements**

To begin, I would like to thank my wonderful wife Melissa whose encouragement and support sustained me throughout graduate school. I would also like to express gratitude to my parents, Mark and Laura, for being life long advocates. As well, my appreciation goes to my wife's parents, Doug and Kristin, for their reassurance in the process.

My advisor, Rich, has been fantastic to work with and I am grateful for his optimism and ability to see more potential in me than I see in myself. More significantly, Rich is a genuine and compassionate person and I prize the opportunity I had to work with him. I would also like to thank David Prendergast for being an integral part of my more recent research. David was a huge scientific help and was wonderful at patiently teaching and providing new perspectives. There are, of course, many others to thank, including all the members of the Saykally group, especially those that I am glad to call my friends.

This dissertation was supported by the Office of Basic Energy Science, Office of Science, U.S. Department of Energy (DOE) through the Lawrence Berkeley National Laboratory Chemical Sciences Division. Computational resources were provided by NERSC, a DOE Advanced Scientific Computing Research User Facility.

## Table of Contents

<b>CHAPTER 1: INTRODUCTION</b>	<b>1</b>
<b>CHAPTER 2: ELECTROKINETICS</b>	<b>7</b>
<b>2.1 Electrokinetic Hydrogen Generation from Liquid Water Microjets</b>	<b>7</b>
Introduction	7
Theoretical background	7
Experimental	10
Results and Discussion	11
Conclusion	15
Figures	16
References	24
<b>2.2 Electrokinetic Power Generation from Liquid Water Microjets</b>	<b>26</b>
Introduction	26
Experimental	27
Results and Discussion	28
Conclusions	31
Figures	32
References	37
<b>2.3 Photoelectrokinetics and Electrokinetic Spectroscopy</b>	<b>39</b>
Introduction	39
Experimental	40
Results and Discussion	41
Conclusions and Future Work	43
Figures	45
References	53
<b>CHAPTER 3: BORON HYDRATION</b>	<b>54</b>
<b>3.1 pH-Dependent X-ray Absorption Spectra of Aqueous Boron-Oxides</b>	<b>54</b>
Introduction	54
Methods	55
Results and discussion	57
Conclusions	60
Figures	61
References	67
<b>3.2 Borohydride-Water Interactions Characterized by X-ray Absorption Spectroscopy</b>	<b>69</b>
Introduction	69
Methods	70
Results and Discussion	72
Conclusions	74
Figures	76
References	84
<b>CHAPTER 4: CONCLUSION</b>	<b>87</b>

# Chapter 1: Introduction

World energy production is currently based on consumption of exhaustible fossil fuels. Developing renewable, inexpensive, and clean sources of energy is clearly imperative. There are, of course, many schemes being researched for the creation and transformation of energy, such as biofuel, solar, and fusion-based methods. There are also many designs for the associated storage of energy, one of the most promising being chemical storage in the form of molecular hydrogen. Energy storage via molecular hydrogen is, of course, desirable because hydrogen combustion releases a large amount of energy per gram (144 kJ/gram vs 48 kJ/gram for octane) and the only reaction products are energy and water. Unfortunately, this scenario has some formidable obstacles. Firstly, current hydrogen generation techniques involve either the use of hydrocarbons or more expensive techniques such as electrolysis[1, 2]. Second, the weight of current hydrogen storage materials and schemes is prohibitive for mobile applications[3]. Fundamental advances are needed before cost-effective hydrogen production and practical hydrogen storage can be realized.

The research described in this dissertation is fundamentally directed to ascertain how water interacts with surfaces and solutes, but is specifically focused on systems that are energy relevant. By measuring electrokinetic currents, I have studied electrokinetic hydrogen production and energy conversion with pure water liquid microjets. I have also employed x-ray absorption spectroscopy (XAS) to characterize borohydride-water interactions, noting that aqueous borohydride systems have been intensely studied as potential hydrogen storage medium.

Electrokinetic phenomena derive from the formation of an electric double layer at a solid-liquid interface, as depicted in Figure 1. The driving force behind double layer formation is minimization of the electrochemical potential of the species at the interface[4]:

$$\bar{\mu}_i = \mu_i + z_i F \Phi \quad 1$$

Here  $\bar{\mu}_i$  is the electrochemical potential of species  $i$ ,  $\mu_i$  is the chemical potential of species  $i$ ,  $z_i$  is the sign and charge on ion  $i$ ,  $F$  is Faraday's constant, and  $\Phi$  is the local electrostatic potential. It is the interplay between the chemical potential and electrostatics that creates the anisotropic charge distribution. For example, at a charged surface, ions of opposite charge will be attracted to the surface, while ions of the same sign (co-ions) will be repelled. This creates a concentration gradient that counteracts the electrostatic forces. Alternatively, an initially uncharged surface could have a higher affinity for one ion over another. In this case, adsorption based on chemical potential will lead to an electrical potential at the interface. Thermal motion will spread the counter-ions (ions opposite in sign to the ions adsorbed on the surface) out in solution, which gives rise to exponential decay in the potential as a function of distance from the interface. The stability of colloids in solution, as well as applications such as electrophoresis and electro-osmotic pumps, all rely on such electric double layer formation.



Electrokinetic streaming currents are another manifestation of electric double layer phenomena. Streaming current generation relies not only on double layer formation, but also on a pressure driven liquid flow that overlaps the anisotropic charge distribution[5-7]. Velocity profiles of liquids are typically zero at the interface, due to the “no-slip condition,” and they increase sharply moving into the liquid. When this velocity profile overlaps with the electric double layer, the flowing liquid entrains the counter-ions and carries them downstream. The entrained ions engender a streaming current.

Streaming currents are typically measured with electrodes situated in reservoirs on either end of a channel[8-10]. The ions carried downstream discharge into a downstream electrode and the ions remaining in the channel typically migrate upstream to discharge into an upstream electrode. Alternatively, the streaming potential can be measured at the upstream and downstream electrodes. When no current passes through the electrodes, the potential causes charges to migrate upstream, against the streaming current. At equilibrium the currents in the upstream and downstream directions are equal.

In the case where pure water is the electrolyte used to create the streaming current, the charges separated are hydroxide and hydrated protons. In this case, neutralization of the protons at the downstream electrode creates molecular hydrogen. Section 1 of Chapter 2 demonstrates the production and characterization of hydrogen from electrokinetic streaming currents. In these experiments, a liquid water microjet is used to spatially separate the upstream and downstream electrodes. In addition, the liquid jet allows for injection of pure water into a vacuum environment, necessary for mass selective detection of hydrogen molecules. The streaming currents and hydrogen production are shown to follow simple equations derived from the overlap of the fluid velocity profile and anisotropic charge distribution.

The liquid microjets demonstrating hydrogen generation also offer marked advantages over other techniques for measuring energy conversion efficiency. As previously mentioned, when measured in a reservoir, the streaming potential causes charge to migrate opposite the streaming current. This back conduction is particularly efficient along the channel surfaces and limits the achievable electrical conversion efficiency[9, 11]. However, liquid microjets break up into a droplet train before reaching the downstream electrode. Consequently, there is no means for back conduction of ions against the flow. As a result, the conversion efficiency is greatly enhanced. Section 2 of Chapter 2 discusses the results of energy conversion efficiency experiments with liquid water microjets. Electrical energy conversion efficiencies over 10% were measured with this technique whereas previous, reservoir based experiments only achieved efficiencies of 3%.

Unfortunately, hydrogen generation and conversion efficiency are both limited by the low electrokinetic currents. Typical microjets (5-20  $\mu\text{m}$  in diameter) can produce currents from 1-700 nA depending on the flow rate. Currents of this magnitude are prohibitively small for realistic application. The potentials associated with these currents can be very high (measured over 20 kilovolts), but high voltage, low current sources are not readily amenable to application. Photoelectrokinetics, presented in Section 3 of Chapter 2, represents an attempt to exploit the high voltage and low currents associated with liquid jet electrokinetics. When the solid is a metal, the potential drop across a solid-liquid interface is almost entirely on the solution side. However, when the solid is a

semiconductor, part of the interfacial potential drop, i.e. a space charge layer, is located within the semiconductor itself. Photo-generated electron-hole pairs that are separated in the electric field of this space charge layer can be used for photo-electrochemistry or current generation. This is the basis for dye-sensitized solar cells and many solar water splitting schemes[12, 13].

With electrokinetic currents, the potential from the unbalanced charges at a channel surface, after the balancing charges have been sheared away with the flowing liquid, would increase the width of the space charge layer. Consequently, with illumination, more electron-hole pairs can be separated. Section 3 of Chapter 2 describes experiments and results aimed at characterizing these photoelectrokinetic currents. In general, electrokinetic currents on silicon surface can be highly sensitive to illumination; however, these experiments were plagued with irreproducibility. The section on photoelectrokinetics also discusses possible schemes for photoelectrokinetic interfacial spectroscopy. Photoelectrokinetic spectroscopy takes advantage of the fact that electrokinetic currents are only generated near an interface in order to measure a surface sensitive spectrum.

Liquid microjets conveniently allow the injection of a thin filament of volatile liquid into a high vacuum environment. This technique opens up a broad range of high vacuum techniques for studying volatile liquids, such as photoelectron and x-ray absorption spectroscopies, including near edge x-ray absorption fine structure (NEXAFS) spectroscopy[14]. NEXAFS involves the promotion of a core level electron to low lying anti-bonding and continuum states within 50 eV of the absorption edge. Because such nonbonding and antibonding states are generally quite diffuse, NEXAFS spectra are typically very sensitive to environmental effects such as hydrogen bonding[15]. Consequently, it is an excellent technique for studying solvation. Our melding of liquid microjet technology with X-ray techniques opened the door to studies of aqueous and other volatile systems.[16]

Chapter 3 describes near edge x-ray absorption spectroscopy studies of boron compounds in water. Sodium borohydride has been intensely studied as a hydrogen storage material[17, 18]. It reacts with water to produce neutral boric acid or the borate anion and molecular hydrogen. Sodium borohydrides is attractive for hydrogen storage materials because it has a high theoretical wt% hydrogen storage capacity (10.8%). Unfortunately, the oxides produced in the hydrolysis reaction are generally much less soluble than the reactants and this low solubility of boron-oxides is one reason borohydrides have not realized more applications as hydrogen storage materials.

The first section of Chapter 3 presents experimental and theoretical NEXAFS results for boric acid, borate ion, and a few polyborate ions. Boric acid and borate form an interesting acid-base pair because there is not a simple deprotonation reaction connecting acid to base. Rather, trigonal boric acid reacts with water to form the tetrahedral borate anion. In spite of the hydroxide moieties on these oxides, they turn out to be not strongly hydrated in water. For example, as the experimental spectra of boric acid, and the theoretical spectra corroborate, that there is no observable change in the pre-edge feature of solvated and solid boric acid. Molecular dynamics simulations of these systems indicate that water arranges itself isotropically around these oxides, similar to the case of hydrophobic systems. This observation correlates with the tendency of boron-oxides to collapse into polyborate ions in solution and with their relatively low solubility.

NEXAFS spectra and calculations of sodium borohydride, presented in Section 2 of Chapter 3, present quite a different story. The spectrum of solvated sodium borohydride is shifted to lower energy and narrowed compared to the spectrum of the solid sample. The spectral changes in this case are directly related to the formation of strong dihydrogen ( $\text{H}\cdots\text{H}$ ) bonds between water and borohydride. The dihydrogen bonds weaken the B-H bonds of the borohydride and the antibonding orbitals are repelled to a lower energy. Consequently, the NEXAFS peak shifts to lower energy. Molecular dynamics simulations suggest that water mainly coordinates to the borohydride along the tetrahedral corners and edge, consistent with previous studies of dihydrogen bonds[19]. Figure 2 shows a snapshot illustrating corner and edge hydration.

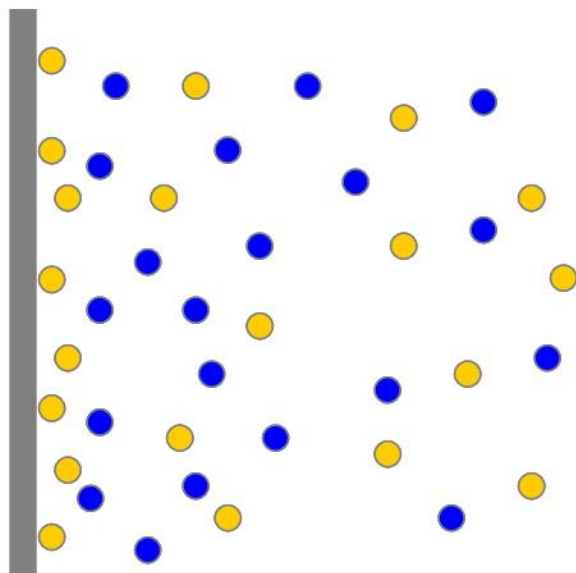


**Figure 1:** Depiction of an electric double layer formed at a solid-liquid interface. The yellow and blue points represent charged solutes of opposite sign. Equilibration of the electrochemical potential for the ions results in an anisotropic charge distribution near the interface.

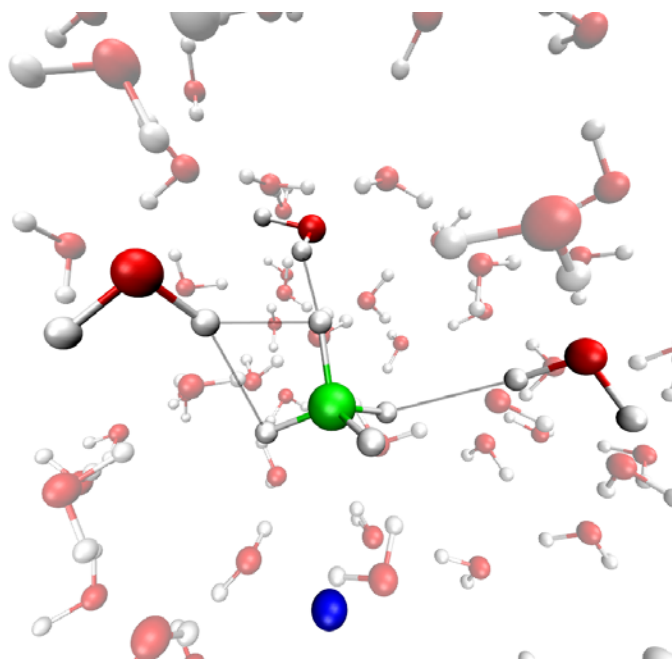


**Figure 2:** Snapshot from a molecular dynamics simulation illustrating the corner and edge dominated hydration for borohydride in water. green – boron; red – oxygen; blue – sodium; white - hydrogen

## References:

1. Service, R.F., *The hydrogen backlash*. Science, 2004. **305**(5686): p. 958-961.
2. Stojic, D.L., et al., *Hydrogen generation from water electrolysis - possibilities of energy saving*. Journal of Power Sources, 2003. **118**(1-2): p. 315-319.
3. *Go/No-Go Recommendation for Hydrolysis of Sodium Borohydride for On-Board Vehicular Hydrogen Storage* <http://www.hydrogen.energy.gov/pdfs/42220.pdf>. 2007.
4. Lyklema, *Fundamentals of Interface and Colloid Science Vol. 2. Solid-Liquid Interfaces*. Vol. 2. 1995.
5. Gavis, J. and I. Koszman, *Development of Charge in Low Conductivity Liquids Flowing Past Surfaces - Theory of Phenomenon in Tubes*. Journal of Colloid Science, 1961. **16**(4): p. 375-&.
6. Rice, C.L. and R. Whitehead, *Electrokinetic Flow in a Narrow Cylindrical Capillary*. Journal of Physical Chemistry, 1965. **69**(11): p. 4017-&.
7. Osterle, J.F., *Unified Treatment of Thermodynamics of Steady-State Energy Conversion*. Applied Scientific Research Section a-Mechanics Heat Chemical Engineering Mathematical Methods, 1964. **12**(6): p. 425-&.
8. van der Heyden, F.H.J., et al., *Electrokinetic energy conversion efficiency in nanofluidic channels*. Nano Letters, 2006. **6**(10): p. 2232-2237.
9. van der Heyden, F.H.J., D. Stein, and C. Dekker, *Streaming currents in a single nanofluidic channel*. Physical Review Letters, 2005. **95**(11).
10. Yang, J., et al., *Electrokinetic microchannel battery by means of electrokinetic and microfluidic phenomena*. Journal of Micromechanics and Microengineering, 2003. **13**(6): p. 963-970.
11. Lyklema, J., *Surface conduction*. Journal of Physics-Condensed Matter, 2001. **13**(21): p. 5027-5034.
12. Licht, S., *Semiconductor electrodes and photoelectrochemistry*. 2002, Weinheim: Wiley-VCH.
13. Maeda, K. and K. Domen, *Photocatalytic Water Splitting: Recent Progress and Future Challenges*. Journal of Physical Chemistry Letters, 2010. **1**(18): p. 2655-2661.
14. Wilson, K.R., et al., *Investigation of volatile liquid surfaces by synchrotron x-ray spectroscopy of liquid microjets*. Review of Scientific Instruments, 2004. **75**(3): p. 725-736.
15. Stöhr, J., *NEXAFS spectroscopy*. 1992, Berlin; New York: Springer-Verlag.
16. Wilson, K.R., et al., *X-ray spectroscopy of liquid water microjets*. Journal of Physical Chemistry B, 2001. **105**(17): p. 3346-3349.
17. Demirci, U.B., et al., *Sodium Borohydride Hydrolysis as Hydrogen Generator: Issues, State of the Art and Applicability Upstream from a Fuel Cell*. Fuel Cells, 2010. **10**(3): p. 335-350.
18. Demirci, U.B. and P. Miele, *Sodium tetrahydroborate as energy/hydrogen carrier, its history*. Comptes Rendus Chimie, 2009. **12**(9): p. 943-950.
19. Epstein, L.M. and E.S. Shubina, *New types of hydrogen bonding in organometallic chemistry*. Coordination Chemistry Reviews, 2002. **231**(1-2): p. 165-181.

## Chapter 2: Electrokinetics

### 2.1 Electrokinetic Hydrogen Generation from Liquid Water Microjets

#### Introduction

The increasing financial and environmental costs of fossil fuel usage have stimulated a renewed campaign to develop economical alternative energy sources. Hydrogen has been investigated to become a major component of world energy solutions due to its high combustion efficiency, nonpolluting chemistry, and renewability. While several major technical problems remain to be solved, including efficient hydrogen storage, the principal obstacle to widespread implementation of “The Hydrogen Economy” is arguably the high cost of production.[1] There are about 90 currently available hydrogen production routes that can be classified into biological, chemical, electrochemical, and thermal categories.[2] Most hydrogen is presently made through coal gasification and by steam reformation of natural gas. Electrochemical hydrogen production methods are quite advanced and straightforward, but are currently very expensive.[2]

This section describes a method for the production of molecular hydrogen from liquid water by exploiting the electrokinetic charge separation that can be effected in fast-flowing liquid microjets. The requisite apparatus is very simple, and involves no moving parts. The input energy is a hydrostatic pressure source and the hydrogen is produced by potential-driven reduction of water enriched in protons. Proton-enriched water is obtained via the electrical charge separation effected by rapid flow of liquid water through a metal orifice. The electrokinetic charge separation process also generates electrical power, which could be harnessed for further electrochemical water splitting.

The principle of electrokinetic current generation is well known.[3-6] By rapidly flowing liquids, e.g. water, through an channel, charges can be separated and transported in the liquid to create an electrokinetic (streaming) current. Early in the 20<sup>th</sup> century, Dolezalek investigated the electrification of benzene in metal pipes.[5, 7] By mid-century, streaming currents were identified as the cause of otherwise mysterious petroleum industry explosions.[5, 8] More recently, Kwok and others have used streaming currents to generate electrical power,[9-11] with Kwok describing the design of an “electrokinetic microchannel battery.” In the present study, streaming currents are used to convert hydrostatic pressure directly into both electrical energy as well as stored chemical energy in the form of molecular hydrogen.

#### Theoretical background

Near the metal-water interface, selective adsorption of one type of charge carrier (hydroxide, in the case of pure water)[12-15] to the metal nozzle surface creates a potential (zeta potential). To maintain charge neutrality, counterions (hydrated protons, in pure water) generate a diffuse layer of charge near the liquid-solid interface. The rapid flow of water through the metal nozzle sweeps away the diffuse, mobile layer, such that

the emerging liquid water jet is positively charged via the unbalanced proton concentration. Figure 1 depicts the electrical double layer (EDL) at the unbiased metal nozzle-water interface as well as the overlap of the EDL with the velocity profile of the flowing water. Physically, it is the overlap of the charge distribution and velocity profile near the solid-liquid interface that is responsible for the streaming current.

Quantitatively, as seen in equation 1, streaming currents in a circular channel of radius  $R$  are described by the integral of the velocity profile,  $v(r)$ , and the net charge distribution,  $\rho(r)$ , where fluid velocity and charge distribution are both functions of the radial distance,  $r$ , from the interface. Both  $v(r)$  and  $\rho(r)$  can be approximated with standard models. [3-6, 8, 16, 17]

$$I_s = 2\pi R \int_0^R \rho(r) v(r) dr \quad (1)$$

The anisotropic charge distribution is the result of the formation of an electrical double layer (EDL) at the metal nozzle-water interface. For a biased surface surrounded by an electrolyte, i.e. an electrochemical electrode, the EDL forms as ions of opposite sign are attracted to the surface while ions of the same sign are correspondingly repelled. In the absence of any electron transfer reactions, overall charge neutrality is maintained across the EDL. However, at an unbiased surface, the EDL is formed as a result of preferential adsorption of one ion over another. Due to thermal fluctuations, the counterions to the adsorbed ions do not remain localized near the surface and form the diffuse component of the double layer. Electrostatic interactions contract the diffuse layer, while thermal motion tends to expand it. As a result, ions are arranged according to a Boltzmann distribution, given in equation 2, where  $n_o$  is the bulk solution ion number density,  $z_i$  is the valency and associated sign of ion  $i$ ,  $e_c$  is the fundamental charge constant,  $\psi(r)$  is the position-dependent potential,  $k_b$  is Boltzmann's constant, and  $T$  is the absolute temperature.

$$n_i(r) = n_{o(i)} e^{\left( -z_i e_c \psi(r) / k_b T \right)} \quad (2)$$

The net charge density  $\rho(r)$ , equation 3, at a given point is the sum of the individual ion number densities.

$$\rho(r) = e_c \sum_i z_i n_i(r). \quad (3)$$

For pure water, a very weak 1:1 electrolyte,  $n_{o(+)} = n_{o(-)} = n_o$  with  $n_o$  being governed by the autoionization constant of water. At 298 K,  $n_o$  has the familiar value of  $1.0 \times 10^{-7}$  mole/L or  $6.02 \times 10^{13} \text{ cm}^{-3}$ . Combining equations 2 and 3, the position dependent charge density of water is given by equation 4.

$$\rho(r) = e_c (n_+ - n_-) = e_c \left[ n_o e^{\left( -e_c \psi(r) / k_b T \right)} - n_o e^{\left( e_c \psi(r) / k_b T \right)} \right] = -2e_c n_o \sinh \left( e_c \psi(r) / k_b T \right) \quad (4)$$

Poisson's equation, equation 5, can then be used to relate the position-dependent potential and the charge distribution.

$$\nabla^2 \psi(r) = -\frac{\rho(r)}{\epsilon} \quad (5)$$

Here  $\epsilon$  is permittivity of the medium times the permittivity of free space. Combining Equations 4 and 5, while making a flat plate approximation (change from radial

coordinate,  $r$ , to linear coordinate,  $x$ ) as well as the Debye-Huckel approximation, leads to a differential equation for the potential as a function of position.

$$\frac{d^2\psi(x)}{dx^2} = \kappa^2\psi(x) \quad (6)$$

$\kappa$  in equation 6 is the inverse Debye length, viz. the inverse of the characteristic double layer thickness, and is given in equation 7.

$$\kappa = \sqrt{\frac{2e_c^2 n_o}{\epsilon k_b T}} \quad (7)$$

This simple differential equation for the potential can be readily solved and implemented to yield the net charge density distribution,  $\rho(x)$ .

Considering the limited thickness of the aperture, the position dependent velocity  $v(x)$  can be easily modeled with a “top hat” profile. This model employs the dimensionless Reynolds number, given in equation 8, which is used to gauge the turbulence of a stream.  $\bar{v}$  is the average bulk velocity,  $d$  is the aperture diameter,  $\rho_w$  is the fluid density and  $\eta_w$  is the fluid viscosity. In micro-channels, the Reynolds number typically remains below the commonly accepted value of 2300 for incipient turbulent flow.

$$R_e = \frac{\bar{v} \cdot d \cdot \rho_w}{\eta_w} \quad (8)$$

However, under fast flowing conditions this criterion may not always hold true. Fortunately, we do not need to specifically consider laminar vs. turbulent flow regimes here because the situation is simplified due to the small thickness of the Pt/Ir aperture that create the liquid jet. At the actual orifice, the Pt/Ir disk (electron microscope aperture: Ted Pella Inc.) thickness is between 0.09 – 0.12 mm. For both laminar and turbulent flow regimes, Equations 9a and 9b give the characteristic length,  $L$ , over which developed flow can be expected to form:[18]

$$\frac{L}{d} \approx 0.06R_e \quad \text{laminar (a)} \quad \frac{L}{d} \approx 4.4R_e^{1/6} \quad \text{turbulent (b)} \quad (9)$$

For all aperture diameters and fluid velocities measured here, the aperture thickness was insufficient to develop either completely turbulent or laminar flow. Consequently, entrance effects dominate, engendering “top hat” velocity profile characteristics. Figure 1b shows the velocity profile near the metal-water interface. The fluid velocity at the water-metal interface is zero and there is a laminar sub-layer near the wall. The fluid velocity increases linearly across this laminar sublayer until it reaches bulk fluid velocity. Equation 10 describes a gradient used to model the slope of the velocity increase near the interface.[3, 16, 19, 20]

$$\frac{dv}{dx} = \frac{\bar{v}}{\delta x} \quad (10)$$

Here  $\bar{v}$  is the average bulk velocity and  $\delta x$  is a measure of the laminar sublayer thickness ( $\delta x = 116 \cdot R_e^{(-7/8)}$ ). Figure 1b also depicts the overlap of the net charge density with the velocity profile.



Combining the equations for net charge density and velocity profile into Equation 1 and integrating with the appropriate boundary conditions leads to a compact equation for the streaming current, equation 11.[3]

$$I_{s1} = \frac{-2\pi R \epsilon \bar{v} \zeta}{\delta x} \quad (11)$$

In equation 11 the surface potential  $\psi_s$  has been replaced by the potential at the shear plane  $\zeta$ , i.e. the potential at the position of the immobile adsorbed layer rather than at the metal surface itself. Plugging in the constants for pure water, the streaming current equation reduces to  $I_s = -6.8 \cdot 10^{-6} \cdot \zeta \cdot d^{0.875} \cdot \bar{v}^{1.875} \text{ Amps}$  where all units have been previously combined to yield amps.

## Experimental

Liquid microjets are generated by using a Jasco PU-2089 HPLC pump to supply pressurized water to a jet nozzle. The jet nozzle apparatus is stainless steel and consists of a base unit and a compression disk, each with mm-scale orifices. The micron-sized jet aperture is positioned over the base orifice and sealed by tightening the compression disk to the base. Jet apertures are platinum/iridium electron microscope apertures (5-20  $\mu\text{m}$  diameter) purchased from Ted Pella Inc. Water is fed to the nozzle through PEEK tubing that is vacuum sealed across a 2  $\frac{3}{4}$ " Conflat flange. The nozzle unit is electrically isolated on the vacuum side of the flange. Flow rates from the pump range from 0-3 mL/min with pressures from 0-48 MPa (ca. 0 – 500 atm). Jet velocities are calculated from the volume flow rate in conjunction with nominal aperture diameter (velocity (m/s) = flow (m<sup>3</sup>/s)  $\div$  area (m<sup>2</sup>)). The water in all experiments is Millipore-filtered with a resistivity of 18.2 M $\Omega$  cm. D<sub>2</sub>O (99.9% D at 0.77 M $\Omega$  cm) for all requisite experiments is purchased from Cambridge Isotope Laboratories Inc. and is used without further purification. Both H<sub>2</sub>O and D<sub>2</sub>O are nitrogen-purged and degassed prior to introduction into the HPLC pump.

Streaming currents are measured by connecting the nozzle to electrical ground through a Keithley 428 Current Amplifier. The amplifier output voltage is read from a digital multimeter. Current is measured as a function of jet velocity by changing the volumetric flow rate, and consequently the backing pressure, at the HPLC pump. Streaming currents can be measured both in ambient air and in vacuum. When measurements are made in air, current can be measured both at the nozzle as well as at an isolated copper target in the path of the jet. When current is measured at the target, it is equal in magnitude but opposite in sign to the current at the nozzle.

In order to measure hydrogen production, the streaming current experiments are conducted in vacuum. The experimental setup, diagramed in Figure 2, consists of a jet chamber and an analysis chamber connected by a Varian precision leak valve. The Conflat flange with the isolated jet nozzle is attached to the top of the jet chamber. The liquid jet from the nozzle travels vertically downward ~1 m in vacuum before striking a sealed off half-nipple, which is immersed in liquid nitrogen to cryotrap liquid water. Three in-line liquid nitrogen traps separate the main part of the jet chamber from the leak valve. A Leybold-Heraeus turbo pump (~140 l/s) is used to pump the jet chamber. The three in-line liquid nitrogen traps effectively remove all water and other condensables before they reach the analysis chamber. Hydrogen produced in the jet chamber can traverse the cryotrap in diffusing to the analysis chamber. The pressure above the jet is

in the sub-millitorr range and drops across the in-line traps to  $\sim 10^{-6}$  torr near the leak valve. To avoid the complicating influence of hot filaments, neither ion gauge nor thermocouple pressure sensors are used during experimental runs.

The analysis chamber contains a Hiden Analytical PSM003 quadrupole mass spectrometer used for residual gas analysis and this chamber is pumped by a BOC Edwards turbopump ( $\sim 70$  l/s) that maintains a base pressure of  $2 \times 10^{-8}$  torr. Gases from the jet chamber are leaked into the analysis chamber for mass separation and detection. Before mass separation, molecules are ionized with 70 eV electrons from the mass spectrometer's internal ionization filament. The mass spectrometer is set for multiple ion detection and repeatedly scans specified masses. A typical scan cycles between masses 2, 3, 4, 18, 19, and 20 ( $\text{H}_2^+$ ,  $\text{HD}^+$ ,  $\text{D}_2^+$ ,  $\text{H}_2\text{O}^+$ ,  $\text{HDO}^+$ , and  $\text{D}_2\text{O}^+$  respectively). Each ion is collected on a Secondary Electron Multiplier (SEM) for 100 ms and the signal is then scaled to output counts per second. The ion signals are also adjusted to account for differences in electron impact cross section. Counts/s for each charge to mass ratio are plotted against the time at which each measurement was collected.

For hydrogen generation experiments, the composition ( $\text{H}_2\text{O}/\text{D}_2\text{O}$ ) and the velocity of the liquid jet are varied while the mass spectrometer collects data for the specified masses. An electrical feedthrough allows for simultaneous measurement of the current at the nozzle. The relatively large  $\text{H}_2$  background present in any UHV chamber interferes with the detection of  $\text{H}_2$  generated by the liquid microjet. However, there is no corresponding  $\text{D}_2$  or  $\text{HD}$  background and  $\text{D}_2\text{O}$  jets can be employed to effectively characterize electrokinetically generated hydrogen.

## Results and Discussion

Figure 3 shows the results for streaming current measurements from a  $5\text{ }\mu\text{m}$  diameter water jet running in air, with Equation 11 used to fit the experimental data. Although the fit to the experimental data is excellent, the  $\zeta$  potential is not faithfully reproduced between different jets and apertures. However, it should be noted that these experiments are not well-suited to obtain an accurate measure of the zeta potential for a water-Pt/Ir interface. Unfortunately, large uncertainties in aperture diameter, and therefore velocity, require the zeta potential to be treated as a fitting parameter rather than as a meaningful physical measurement.

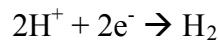
Gavis and Kosman as well as Faubel indicate that,[5, 21] under dynamic conditions, the distance over which charge separation exists is contained within the laminar sublayer; that is, the charge density distribution used to derive the streaming current equation may not be rigorously correct. It is unclear whether or not the double layer thickness is contracted under dynamic conditions, or whether it overestimated even under static conditions, but in either case, it is unlikely that the EDL extends beyond the laminar sublayer adjacent to the metal-water interface. However, since the value for the zeta potential is adjusted to fit the experimental data, it is also adjusted to compensate for any charge distribution contraction.

A thinner double layer or double layer contraction can also be invoked to justify the use of the flat plate approximation rather than cylindrical coordinates. For the present conditions, the radius of curvature of all apertures ( $>5\text{ }\mu\text{m}$ ) is likely to be large compared to the contracted or true double layer thickness ( $<1\text{ }\mu\text{m}$ ). As attempts to fit the streaming current data using cylindrical coordinates failed to yield an improvement, a one

dimensional model is presumed adequate in describing the charge distribution. Although the structure of Equation 11 was first derived for more macroscopic fluid flows, it faithfully reproduces our experimental data for liquid water microjets. In spite of the difficulties in measuring the actual zeta potential, Equation 11, as well as analogous equations using similar velocity profiles, fit the experimental data very well and confirm that the streaming current scales nearly quadratically with flow velocity. It should be noted that Equation 11 is independent of channel length. This observation is consistent with the fact that the timescale for double layer formation (<ns) is much faster than the time it takes the water to traverse the channel ( $\sim\mu\text{s}$ ) [5, 22] i.e. the excess charge shorn from the interface builds up and reaches a steady level very early in the channel. The excess ions in the fluid flow are able to equilibrate with the EDL further down the channel to inhibit further electrification and preclude any streaming current length dependence.

The model for streaming currents from liquid jets, equation 11, has natural temperature dependence in the form of changes in the density, viscosity, and permittivity of water. Table 1[23] shows the variations of viscosity, density, and permittivity of water with temperature. Using values from Table 1, the streaming current is predicted to increase with temperature. Experimentally, the effect is just the opposite. Figure 4 shows the temperature dependent streaming current from two jets with slightly different aperture diameters. The current clearly decreases with temperature in each case. It is the changes in viscosity that leads to an incorrect increase in the predicted streaming current with temperature. Recalculating the streaming current at a fixed viscosity with temperature dependent density and dielectric constant reproduces the correct downward trend with temperature. Figure 4 also shows currents calculated from Equation 11 with a fixed rather than temperature dependent viscosity. Water is more structured near the wall and, consequently, in the region of electrokinetic current generation. The viscosity of the structured water near the wall is less susceptible to changes in viscosity due to temperature. This observation is in line with previous studies in narrow capillaries.[24]

When pure water is used as the electrolytic solution, streaming currents are inevitably produced from the separation of hydronium (or other forms of the hydrated proton) and hydroxide ions. As the current from ground to nozzle is positive, the zeta potential must be negative, with excess negative charge existing at the metal/water interface. Thus, it is the hydroxide ions that preferentially collect at the interface, with excess hydronium ions in the diffuse layer. Fluid movement carries hydronium ions downstream and concentrates hydroxide ions in the nozzle. The excess charge creates a potential in the nozzle that induces these hydroxide ions to discharge at the Pt/Ir interface. Anion discharge at the interface forces electrons from the nozzle to electrical ground and gives rise to the positive currents observed. The liquid emerging from the aperture is positively charged due to excess hydronium ions. When this charged liquid beam encounters a grounded metal target electrode downstream, electrons flow from the electrode into the solution, reduce the hydronium, and generate hydrogen, according to the process:



Hydroxide ions that remain in the jet aperture may generate the observed positive nozzle current from ground to nozzle via the process:



However, we have no direct measurements to support this at the present time, and more complicated reactions may well be involved. It is observed that a single jet can be run for approximately 10 hours before there is a noticeable increase in diameter. The diameter increase may be due to electrochemical corrosion of the metal or it may be simple erosion.

Figure 5 shows mass spectrometer signals for an experiment using a 10  $\mu\text{m}$  diameter jet with a constant flow rate of 0.5 mL/min. During the course of the experiment, the jet composition was varied from pure  $\text{H}_2\text{O}$  to pure  $\text{D}_2\text{O}$  and then back to  $\text{H}_2\text{O}$ . As charged ice builds up at the target electrode, the potential rises and drives increasing proton neutralization; consequently, the  $\text{H}_2^+$  signal increases. After 7 minutes, the composition of the jet was changed to pure  $\text{D}_2\text{O}$ ; however, the response is delayed while the  $\text{D}_2\text{O}$  travels to and fills the relatively large internal volume ( $\sim 3$  mL) of the nozzle apparatus. The  $\text{H}_2^+$  signal then decreases, while the  $\text{HD}^+$  signal increases. As the mixing continues, the  $\text{HD}^+$  signal reaches a maximum and then decreases while the  $\text{D}_2^+$  increases. After 31 minutes, the jet composition is returned to pure  $\text{H}_2\text{O}$  and the process is shown to be entirely reversible.

The  $\text{H}_2^+$ ,  $\text{D}_2^+$ , and  $\text{HD}^+$  mass spectrometer signals are all characterized by intermittent spikes that confirm the production of molecular hydrogen at the jet target. The liquid nitrogen-cooled trap becomes coated with insulating layers of ice that separate what is essentially a charged icicle from the electrically grounded electrode. As the icicles collapse under gravity, or when the potential reaches a point where discharge through the ice becomes possible, a spike of hydrogen is observed. Figure 6 is a photograph of the jet chamber after a hydrogen production experiment. The jet was shooting down into the plane of the photograph and the charged icicle (dark spot in the center of the photo) is climbing up out of the plane of the photograph. At intervals, icicle shoots at right angles to the main icicle are visible. These shoots presumably grew to the chamber wall in order to neutralize the charged icicle. In other experiments, (not shown) hydrogen production closely followed the current measured at the target, including the spikes. It remains possible, but unlikely, that lightning bolt discharge in the charged ice produced solely from impurities is the cause of hydrogen production.

Although the mass spectrometer uses a hot filament to generate electrons that are subsequently accelerated to 70 eV and used to ionize sample molecules, it is not possible that the hydrogen signals observed in Figure 4 resulted either from cracking of water on this hot filament, or from fragmentation of water with 70 eV electrons. Although, a certain percentage of the  $\text{H}_2$  background in the chamber originates from residual water that has been produced by these two mechanisms, they cannot account for the experimentally measured  $\text{H}_2$  and  $\text{D}_2$  signals. The  $\text{H}_2\text{O}^+$ ,  $\text{HDO}^+$ , and  $\text{D}_2\text{O}^+$  signals in Figure 4 show no observable change as the liquid composition varies from  $\text{H}_2\text{O}$  to  $\text{D}_2\text{O}$  and back. These flat signals imply that the marked changes found in the corresponding  $\text{H}_2^+$ ,  $\text{D}_2^+$ , and  $\text{HD}^+$  signals are not being produced at the hot filament or by fragmentation. There is roughly a three orders-of-magnitude difference between the electron ionization cross sections for production of  $\text{H}_2\text{O}^+$  and  $\text{H}_2^+$  from  $\text{H}_2\text{O}$  (similar for  $\text{D}_2\text{O}$ )[25], so changes in the  $\text{H}_2^+$ ,  $\text{D}_2^+$ , and  $\text{HD}^+$  signals originating from fragmentation would unavoidably be associated with changes in the corresponding water signals. Similarly, isotopic changes in hydrogen that is formed at the hot filament would require corresponding isotopic changes in the water background. The flat  $\text{H}_2\text{O}^+$ ,  $\text{D}_2\text{O}^+$ , and

HDO<sup>+</sup> signals confirm that the condensable vapors from the jet chamber are effectively removed by the liquid nitrogen traps before entering the analysis chamber and, consequently, that the observed hydrogen signals originate from the gas produced in the jet chamber.

Figure 7 shows the D<sub>2</sub>O<sup>+</sup> and D<sub>2</sub><sup>+</sup> mass spectrometer signals as a function of time and at various jet velocities. After a build-up phase, at  $t = 0$  the jet flow was reduced to 0.2 mL/min. Afterwards, the pure D<sub>2</sub>O jet was operated for 10 minutes at each of the flow rates indicated (0.2, 0.5, 0.1, 0.4, 0.6, 0.3 mL/min). Again, the D<sub>2</sub><sup>+</sup> signal shows an irregular spiky pattern that indicates D<sub>2</sub> formation as the charged icicles collapse and/or discharge to the grounded electrode surface. Despite the fact that unpredictable ice build-up and discharge give large spikes and depressions, there is an obvious step pattern in the D<sub>2</sub><sup>+</sup> signal as the flow rate is increased or decreased. Again, the D<sub>2</sub>O<sup>+</sup> signal remains constant throughout the experiment, indicating that the D<sub>2</sub> is not formed in the analysis chamber.

The current at the nozzle is also plotted in Figure 7 (secondary axis). As expected, there is a clear relationship between the D<sub>2</sub><sup>+</sup> signal and the electrokinetic current. Figure 8 is a plot of the average D<sub>2</sub><sup>+</sup> signal vs. average current for each flow rate. The hydrogen production exhibits the same (nearly quadratic) velocity dependence as the electrokinetic current. As a result, plotting D<sub>2</sub><sup>+</sup> as a function of current gives a straight line.

While the present experiment was designed to measure hydrogen production from electrokinetic streaming currents, it also gives indirect insight into the nature of the unbiased Pt-water interface. In general, any contact between two materials with different chemical potentials (i.e. work functions) will induce charge transfer from one to the other until equilibrium is reached, and the chemical potentials become equal. Based on the sign of the measured streaming currents, as well as the observation that hydrogen gas is produced at the target, it is logical to conclude that hydroxide binds more favorably to the platinum surface, with partial charge transfer of electrons into the metal. While hydrated protons have recently been shown to preferentially adsorb to the water-air interface,[26] hydroxide ions are known to preferentially adsorb to metal surfaces because of the very large induction interactions attending their large dielectric constants.[12, 13] Recent calculations indicate that hydroxide will contact adsorb to silver with charge transfer to the metal, while hydronium will adsorb in a solvated state.[15, 27] Hydrated protons in the diffuse layer would balance the charge from surface hydroxides; however, as the diffuse layer is sheared away from the surface, charge neutrality is lost and the corresponding potential increase drives the hydroxide ions to fully discharge into the metal. Consequently, electrons flow from the jet nozzle to ground and the streaming current is measured to be positive. As streaming currents at the jet target electrode and hydrogen production can be measured irrespective of whether the nozzle is floating or grounded, it should be noted that hydroxide ions can back conduct through the liquid; however, unless necessary, this process is expected to be small due to the large resistance (~Tera $\Omega$ ).

As hydrogen production was also observed from molybdenum apertures, it is unlikely to be a result of any catalytic properties of the Pt/Ir aperture. Gavis and Koszman indicate that there is little difference between electrokinetic charge generation rates between different metals.[5]

Considering the fact that most of the hydrogen produced at the grounded target electrode is pumped out of the chamber before detection, the efficiency of the energy conversion process could not be directly measured from the mass spectrometer signals. However, as hydrogen production is directly related to the measured current, the current can be used to obtain order of magnitude estimates for efficiency. For a 5  $\mu\text{m}$  aperture flowing at 0.34 mL/min, the backing pressure is about 10 MPa and the streaming current is about 180 nA. These numbers give a total mechanical power input of 0.057 W (flow rate  $\cdot$  pressure). Using the free energy of formation of liquid water and assuming that all the current generates hydrogen molecules, the chemical power for hydrogen production is about  $2 \cdot 10^{-7}$  W. Taking the ratio of chemical/mechanical power gives an efficiency of  $\sim 4 \cdot 10^{-6}$ .

Changes in the nozzle geometry to increase the surface area/volume ratio of the resulting liquid jet should improve the electrokinetic efficiency, as could the use of more exotic nozzle material. Optimization of the pH and ionic strength of the fluid, as well as temperature, flow values, and electrode bias could yield higher efficiency as well. Future experiments will focus on improving the chemical efficiency with different aperture materials and fluid compositions as well as by elucidating the mechanism by which anions are neutralized at the metal water-interface.

## Conclusion

The electrokinetic streaming currents generated from water flowing through micron-sized Pt/Ir apertures can be modeled very well with Equation 11. As evident from the experimental data, as well as the fitting equation, the streaming current scales nearly quadratically with fluid velocity. The physical origin of the streaming current is the overlap of a hydrodynamic velocity gradient with the electrical double layer formed at the Pt-water interface. Although the present experiment did not give direct information about the Pt-water interface, the data indicate that the EDL is formed as hydroxide anions adsorb more favorably to the Pt surface than do hydronium cations, as supported by previous results in the literature.[12, 15] Pressure-driven flow creates a velocity profile that shears charge, the hydrated protons in this case, from the diffuse double layer and carries it out of the aperture. The pressure-induced separation of charge creates large electrical potentials that subsequently cause the ions to be neutralized at the grounded target electrode or in the nozzle. Neutralization (reduction) of the hydronium ions at the target electrode produces gaseous hydrogen molecules. It is suspected that oxygen is formed by oxidation in the jet aperture; however, we could not detect oxygen with the present experimental design. The hydrogen produced from electrokinetic streaming currents reversibly follows fluid composition as the jet is switched between  $\text{H}_2\text{O}$  and  $\text{D}_2\text{O}$ . Hydrogen production also follows jet velocity, with corresponding increases/decreases in hydrogen production as jet flow rate increases/decreases. As could be expected, there is a direct linear relationship between the streaming current and the amount of hydrogen produced. The present efficiency for hydrogen generation is ca.  $10^{-6}$  but can be improved by several design considerations.

## Figures

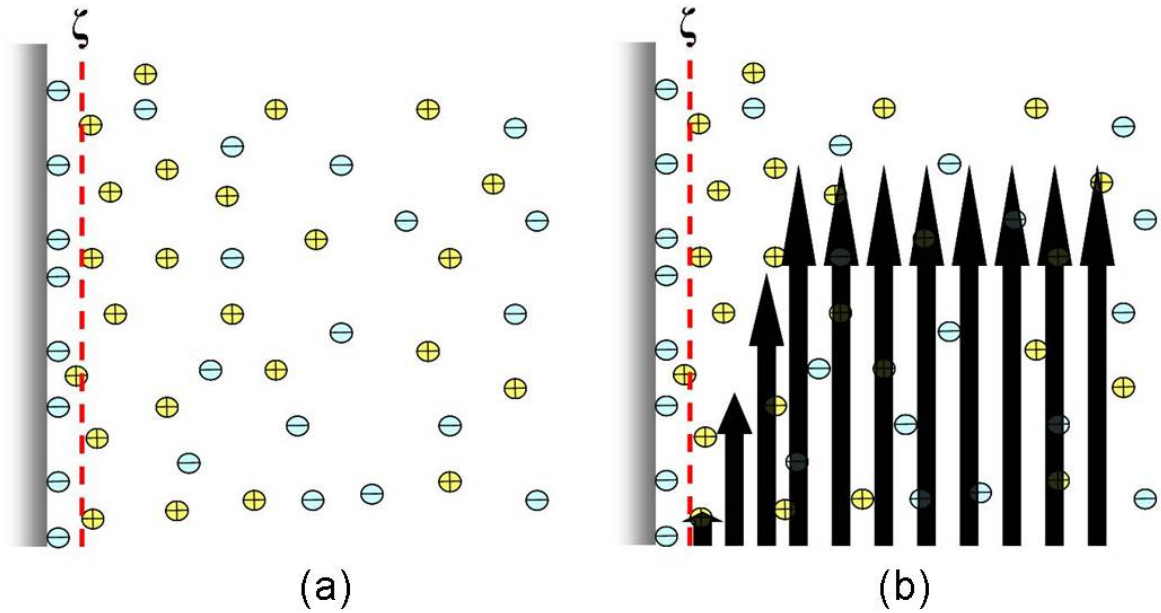


**Figure 1:** Representation of charge distribution at a metal-water interface. (a) Inhomogeneous charge distribution at a metal-water interface resulting from selective adsorption of hydroxide ions to the surface. (b) Overlap of charge distribution with the fluid velocity profile. The arrow height indicates positional liquid flow velocity in microjet nozzle. In both panels, the approximate position of the plane of shear is marked with the dashed line; the zeta potential ( $\zeta$ ) is the electrical potential at this plane with respect to the bulk liquid. Pressure-induced flow shears charge from the diffuse layer and leaves unbalanced negative charges at the metal-water interface, such that the emerging liquid jet is enriched in protons.

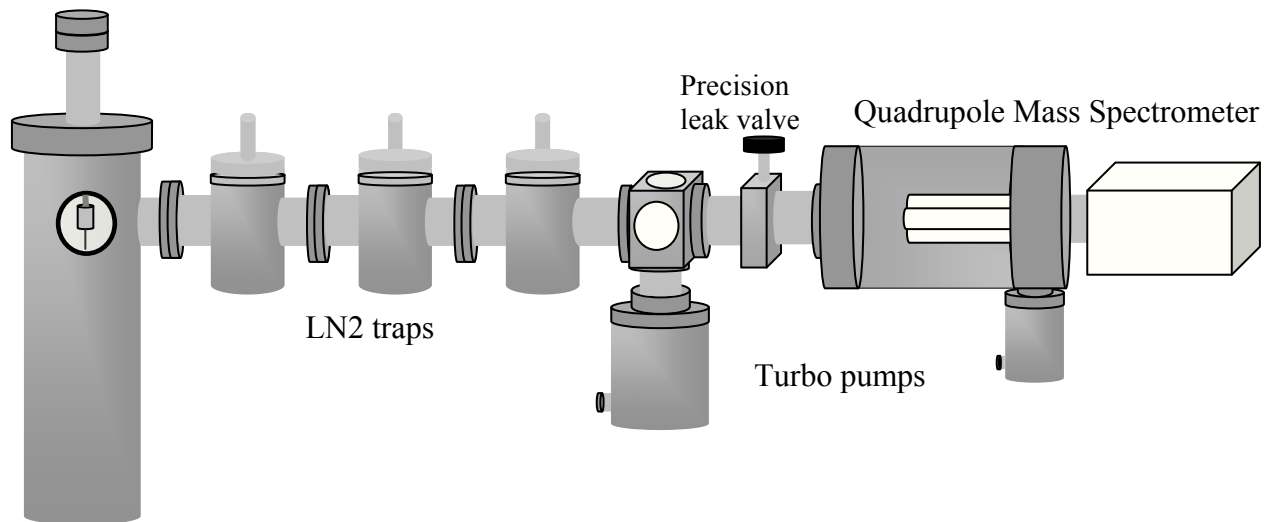


**Figure 2:** Diagram of experimental setup

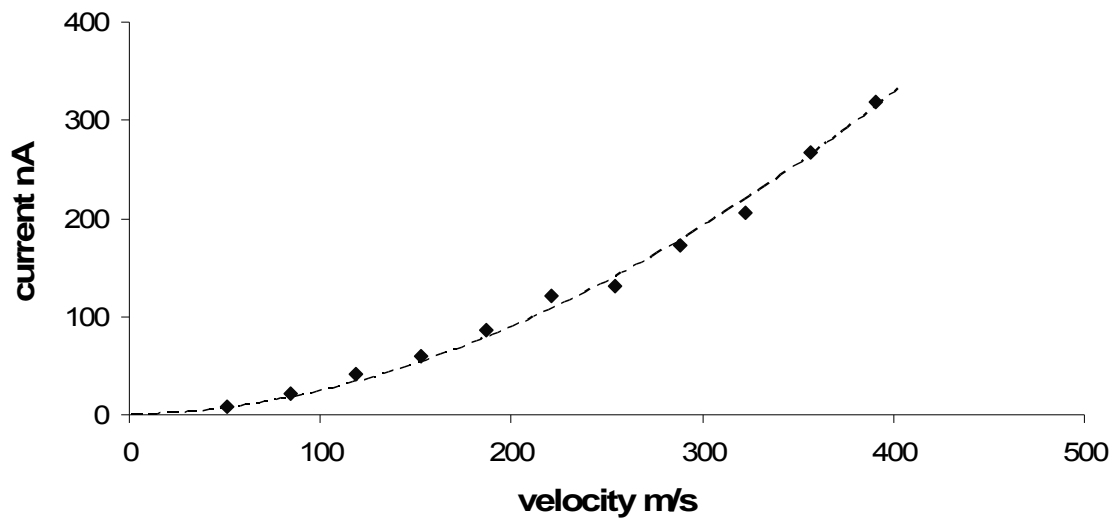


**Figure 3:** Streaming current as a function of jet velocity from a 5 $\mu$ m aperture. (♦) experimental data; (--) streaming current model (Equation 11 in text) with  $\zeta = -0.0275 \pm 0.0004$  V ( $R^2 = 0.9933$ ) The data confirm a nearly quadratic increase in current with fluid velocity, as predicted from theory.



Temp (°C)	Density g/cm <sup>3</sup>	Viscosity μPa s	Dielectric Constant
0	0.99984	1791.1	87.899
10	0.99970	1305.9	83.974
20	0.99821	1001.6	80.223
30	0.99565	797.22	76.634
40	0.99222	652.73	73.201
50	0.98803	546.52	69.916
60	0.98320	466.03	66.774
70	0.97776	403.55	63.770
80	0.97179	354.05	60.898
90	0.96531	314.17	58.152

**Table 1:** Density, viscosity, and dielectric temperature dependence of water.[23]

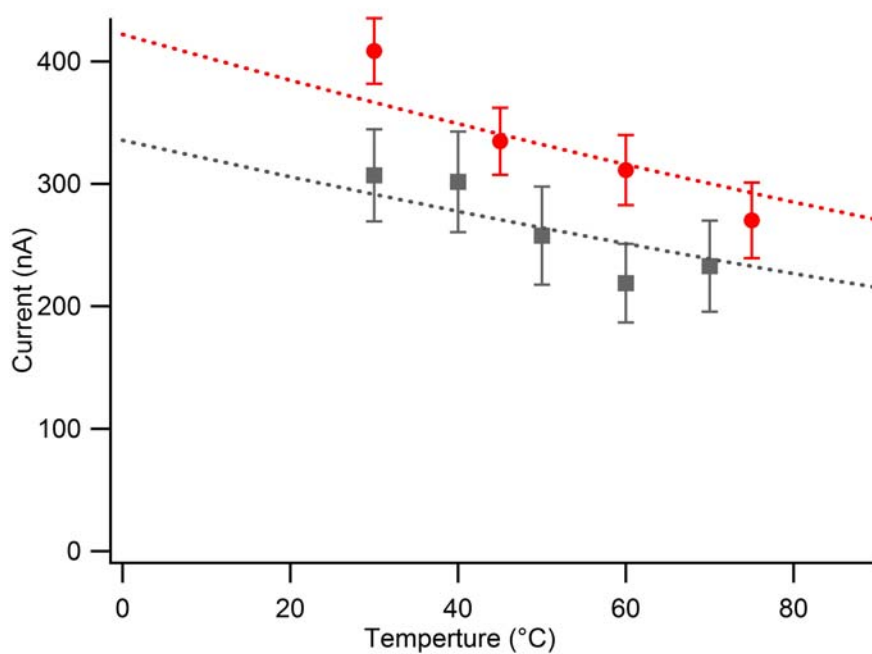


**Figure 4:** Streaming current data (circles and squares) from two similar jets as a function of temperature. The dashed lines fit to each data series are calculated from the streaming current equation with adjustments for the temperature dependence of density and dielectric constant. Changes in viscosity with temperature are excluded indicating that changes in viscosity with temperature do not overcome the structuring of water at a surface.

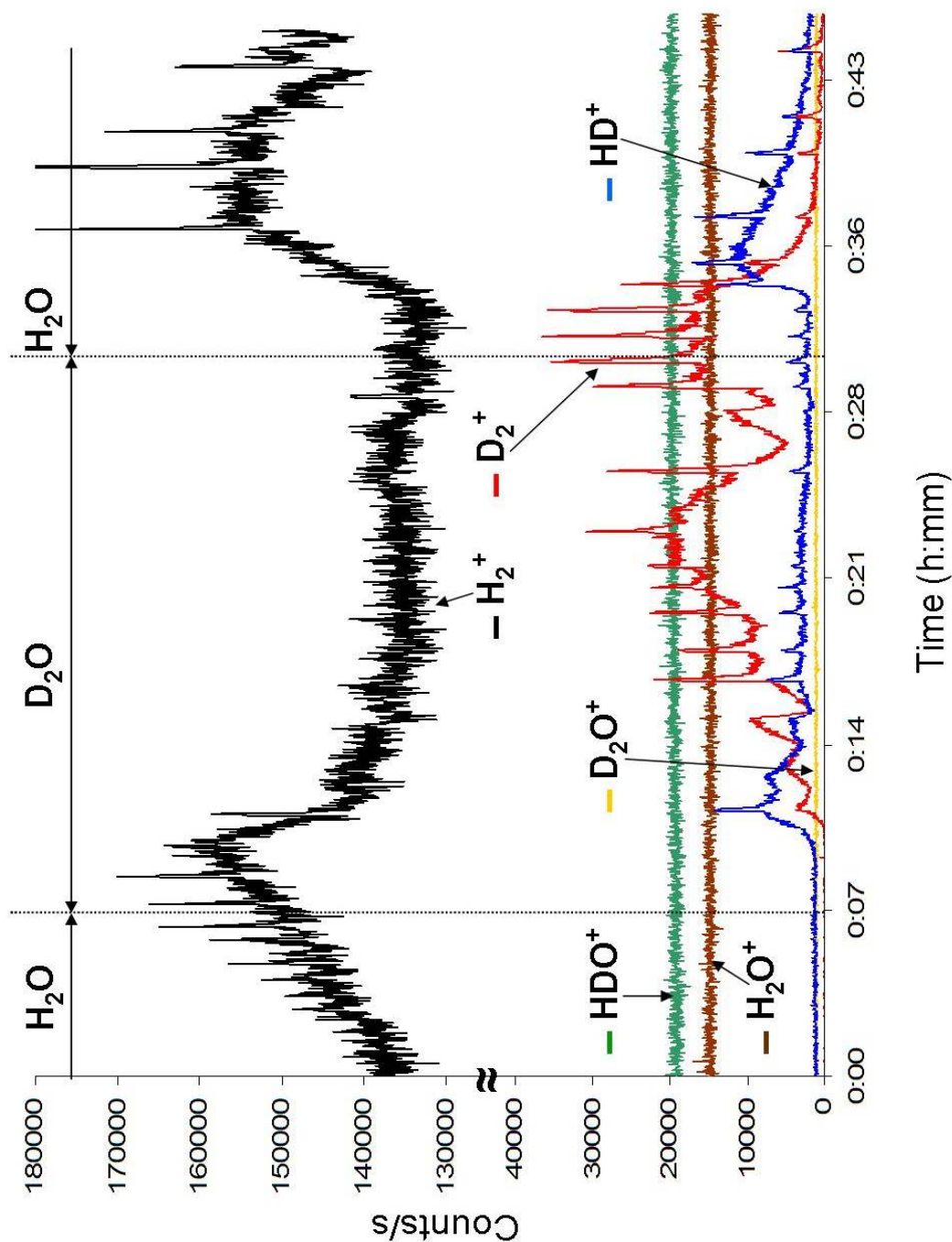


**Figure 5:** Mass spectrometer signals for hydrogen and water isotopes as liquid jet composition is switched from H<sub>2</sub>O (0-7 min) to D<sub>2</sub>O (7-31 min) and back to H<sub>2</sub>O (31-47 min). Black – H<sub>2</sub><sup>+</sup>, Red – D<sub>2</sub><sup>+</sup>, Blue – HD<sup>+</sup>, Brown – H<sub>2</sub>O<sup>+</sup>, Yellow – D<sub>2</sub>O<sup>+</sup>, Green – HDO<sup>+</sup>. Data were collected with a 10 μm diameter jet flowing at 0.5 ml/min. Note that isotopic hydrogen signals follow jet composition while the oxygen-containing water signals are invariant.



**Figure 6:** Photograph of the experimental jet chamber after a hydrogen production experiment. The dark spot in the center is an icicle growing vertically up out of the plane of the picture. Icicle offshoots, at right angles to the main icicle, grew to the chamber wall to more easily neutralize the charged ice.

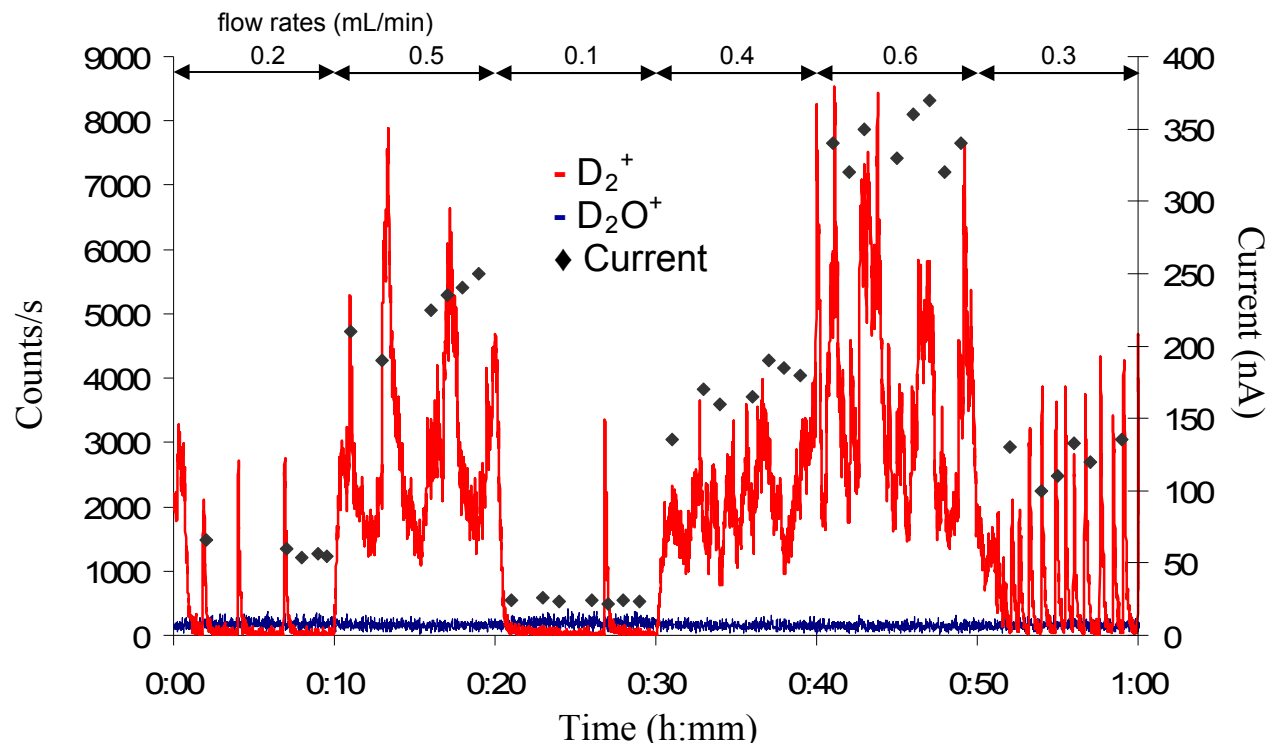


**Figure 7:**  $D_2^+$  and current measurements from a 10  $\mu\text{m}$  jet at varying jet velocities (flow rates indicated at the top). Primary axis:  $D_2^+$  (red) and  $D_2O^+$  (blue) mass spectrometer signals. Note the  $D_2^+$  signal changes with jet velocity while the  $D_2O^+$  is invariant. Secondary axis: electrokinetic current ( $\blacklozenge$ ) measured at nozzle. The  $D_2^+$  signal is found to be proportional to the current, i.e. both scale nearly quadratically on flow velocity.

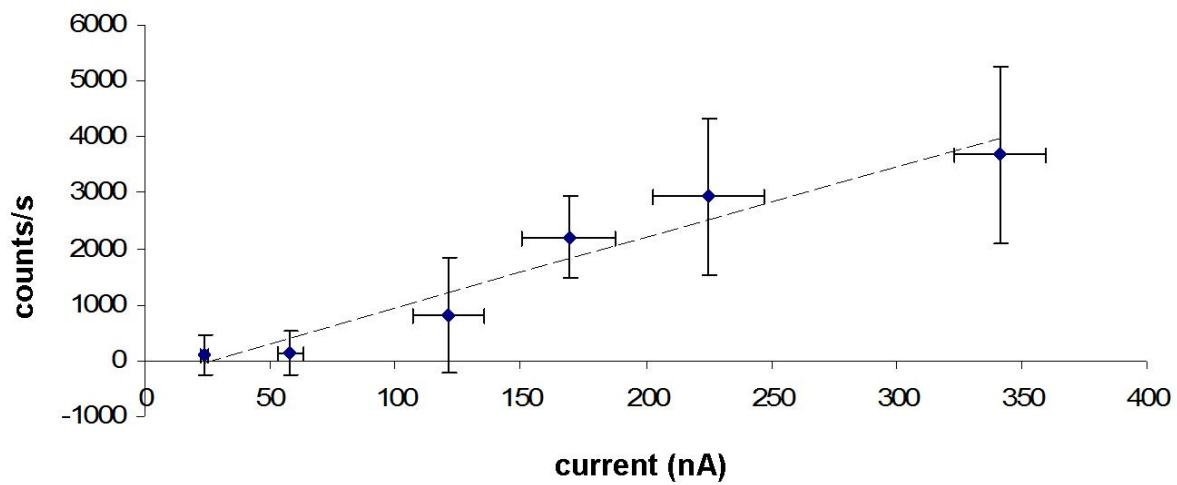


**Figure 8:** Counts  $D_2^+$  plotted as a function of current. Both scale nearly quadratically with flow rate; consequently, there is a linear relationship between current and  $D_2$  production

## References

1. Service, R.F., *The hydrogen backlash*. Science, 2004. **305**(5686): p. 958-961.
2. Stojic, D.L., et al., *Hydrogen generation from water electrolysis - possibilities of energy saving*. Journal of Power Sources, 2003. **118**(1-2): p. 315-319.
3. Davies, J.T. and E.K. Rideal, *Interfacial Phenomena*. 1961, New York: Academic Press.
4. Lyklema, *Fundamentals of Interface and Colloid Science Vol. 2. Solid-Liquid Interfaces*. Vol. 2. 1995.
5. Gavis, J. and I. Koszman, *Development of Charge in Low Conductivity Liquids Flowing Past Surfaces - Theory of Phenomenon in Tubes*. Journal of Colloid Science, 1961. **16**(4): p. 375-&.
6. Rice, C.L. and R. Whitehead, *Electrokinetic Flow in a Narrow Cylindrical Capillary*. Journal of Physical Chemistry, 1965. **69**(11): p. 4017-&.
7. Dolezalek, F., *The Electrical Excitability of Liquids*. Chemistry and Industry, 1913. **36**: p. 33.
8. Klinkenberg, A. and J.L. Van Der Minne, *Electrostatics in the Petroleum Industry-The Prevention of Explosion Hazards*. 1958, New York: Elsevier. 191.
9. Yang, J., et al., *Electrokinetic microchannel battery by means of electrokinetic and microfluidic phenomena*. Journal of Micromechanics and Microengineering, 2003. **13**(6): p. 963-970.
10. Olthuis, W., et al., *Energy from streaming current and potential*. Sensors and Actuators B-Chemical, 2005. **111**: p. 385-389.
11. vanderHeyden, F.H.J., et al., *Power Generation by Pressure-Driven Transport of Ions in Nanofluidic Channels*. Nano Lett., 2007. **7**(4): p. 1022-1025.
12. Bruesch, P. and T. Christen, *The electric double layer at a metal electrode in pure water*. Journal of Applied Physics, 2004. **95**(5): p. 2846-2856.
13. Magnussen, O.M., *Ordered anion adlayers on metal electrode surfaces*. Chemical Reviews, 2002. **102**(3): p. 679-725.
14. Service, R.F., *Chemistry - Platinum in fuel cells gets a helping hand*. Science, 2007. **315**(5809): p. 172-172.
15. Patrito, E.M. and P. Paredes-Olivera, *Adsorption of hydrated hydroxide and hydronium ions on Ag(111). A quantum mechanical investigation*. Surface Science, 2003. **527**(1-3): p. 149-162.
16. Holstein, W.L., et al., *Aspects of electrokinetic charging in liquid microjets*. Journal of Physical Chemistry B, 1999. **103**(15): p. 3035-3042.
17. Delgado, A.V., et al., *Measurement and interpretation of electrokinetic phenomena*. Journal of Colloid and Interface Science
- Elkin 06, International Electrokinetics Conference, June 25-29, Nancy, France, 2007. **309**(2): p. 194-224.
18. White, F.M., *Fluid Mechanics*. 4 ed. 1999: WCB Mcgraw-Hill.
19. Hignett, E.T. and J.C. Gibbins, *Electrostatic Streaming Current Developed in Turbulent Flow through a Pipe*. Journal of Electroanalytical Chemistry, 1968. **16**(2): p. 239-&.

20. Rouse, H. and J.W. Howe, *Basic Mechanics of Fluids*. 1953, London: John Wiley & Sons, Inc.
21. Faubel, M. and B. Steiner, *Strong Bipolar Electrokinetic Charging of Thin Liquid Jets Emerging from 10  $\mu$ m PTFE Nozzles*. *Berichte Der Bunsen-Gesellschaft-Physical Chemistry Chemical Physics*, 1992. **96**(9): p. 1167-1172.
22. Geissler, P.L., et al., *Autoionization in liquid water*. *Science*, 2001. **291**(5511): p. 2121-2124.
23. *CRC Handbook of Chemistry and Physics, 2009-2010, 90th ed.* Journal of the American Chemical Society, 2009. **131**(35): p. 12862.
24. Churayev, N.V.S., V.D.; Zorin, Z.M., *Measurement of Viscosity of Liquids in Quartz Capillaries*. *Special Discussions of the Faraday Society*, 1970. **1**: p. 213-220.
25. Straub, H.C., et al., *Absolute partial cross sections for electron-impact ionization of H<sub>2</sub>O and D<sub>2</sub>O from threshold to 1000 eV*. *Journal of Chemical Physics*, 1998. **108**(1): p. 109-116.
26. Petersen, P.B. and R.J. Saykally, *Evidence for an enhanced hydronium concentration at the liquid water surface*. *Journal of Physical Chemistry B*, 2005. **109**(16): p. 7976-7980.
27. Olivera, P.P., A. Ferral, and E.M. Patrito, *Theoretical investigation of hydrated hydronium ions on Ag(111)*. *Journal of Physical Chemistry B*, 2001. **105**(30): p. 7227-7238.



## 2.2 Electrokinetic Power Generation from Liquid Water Microjets

### Introduction

Electrokinetic hydrogen production, discussed in the previous section, is ultimately limited by low electrokinetic currents. With currents in the nano-Amp range, a macroscopic buildup of hydrogen takes a prohibitively long time. However, as mentioned in the previous section, the current, although very low, can be driven at high voltages. Consequently, the electrical energy conversion obtainable with liquid microjets is not limited as the chemical energy conversion and the conversion is much more efficient.

A central goal of current energy research is to efficiently produce electricity from renewable sources. As mentioned in the previous section, the energy conversion properties of micro- and nanofluidic devices have received increased attention.[1] A number of studies have focused on producing electrokinetic currents by forcing water through porous materials.[2-4] Others have concentrated on the electrical properties of single well-defined channels.[5-11]

The previous chapter included a more detailed introduction into modeling the electrokinetic currents. Only a brief review will be given here. Whether via multiple pores or a single channel, electrokinetic current generation depends on the overlap of a fluid velocity profile and the anisotropic charge distribution existing near a solid-liquid interface. The charge distribution at the surface, or electrical double layer, forms as certain ions in solution preferentially adsorb to a neutral or charged solid surface. This preferential interaction of ions with the surface induces counter ions of the opposite charge to redistribute near the interface. When tangential fluid flow overlaps significantly with the electrical double layer, unbalanced charges are carried downstream. More precisely, the electrokinetic streaming current can be calculated by equating it with the product of the charge density distribution,  $\rho(r)$ , and the fluid velocity profile,  $v(r)$ , integrated over the interface.[7-9, 11-14] For example, the streaming current from a circular channel is given by equation 1, where  $R$  is the channel radius and  $r$  is the distance from the channel wall.

$$I_s = 2\pi R \int_0^R v(r) \rho(r) dr \quad (1)$$

For non-overlapping double layers, the charge density distribution is typically represented using a Poisson-Boltzmann description.[6] For micro and nanofluidic devices, the velocity profile is usually modeled by Poiseuille flow[6]; however, for short channels dominated by entrance effects, an undeveloped “top hat” model is more appropriate.[11] Poiseuille flow leads to streaming currents that vary linearly with the fluid velocity, while undeveloped flow leads to streaming currents that increase nearly quadratically with flow rate. For the latter case, the streaming current is effectively fit with equation 2, where  $\bar{v}$  is the average fluid velocity,  $\delta x$  is a measure of the laminar sublayer thickness ( $\delta x = 116 \cdot R \cdot Re^{(-7/8)}$ ),  $\epsilon$  is the permittivity of the medium times the permittivity of free space, and  $\zeta$  is the potential at the shear plane.  $Re$  is the Reynolds number.[11]

$$I_s = \frac{-2\pi R \bar{\epsilon} \bar{\nu} \zeta}{\delta x}, \quad (2)$$

To date, efforts at using streaming currents to generate electrical power have employed two reservoirs connected by means of a single channel or porous material. Initially, high pressure is applied to one reservoir and charge is moved across the channel, building up in the receiving reservoir. As this polarization evolves, the unbalanced charges in the two reservoirs create a streaming potential and the streaming potential drives ions against the fluid flow. At equilibrium, the net current is zero and back conduction exactly equals the streaming current. A low resistance path between the two reservoirs, or between each reservoir and electrical ground, short circuits back conduction and can be used to measure the streaming current. Alternatively, a high resistance probe inserted between the reservoirs can be used to measure the streaming potential. The streaming potential, together with the streaming current, ultimately determine the electrical power that can be generated from the device. When a load resistor is placed between the reservoirs, it becomes straightforward to calculate the energy conversion efficiency,  $\eta$ , as energy output divided by energy input, or in this case, electrical power divided by volumetric flow rate and pressure differential.

$$\eta = \frac{I_s^2 R_L}{Q \Delta P} \quad (3)$$

In equation 3,  $I_s$  is the streaming current,  $R_L$  is the resistance,  $Q$  is the volumetric flow rate, and  $\Delta P$  is the pressure drop across the channel. Notwithstanding calculations predicting efficiencies as high as 15% [6, 8, 15] experiments have thus far yielded efficiencies of only 3.2% [7] and 0.80% [3] for a single nanochannel and a porous glass plug, respectively.

Low energy conversion efficiency in previous experiments is attributed to surface back conduction of ions [7, 16, 17]. Electrokinetic current generation, like all electrokinetic effects, relies on an anisotropic ion distribution at an interface. Ions at the solid surface engender surface conduction and provide an additional route for dissipating charge, reducing conversion efficiency. Electrokinetic power generation using liquid water microjets eliminates both surface and bulk back conduction via creation of a jet of water that breaks up into a droplet train before reaching the receiving reservoir. Under these conditions, accumulated charge can only dissipate through the load resistor and efficiency is dramatically increased. In addition, the thin metal jet orifice creates flow conditions wherein entrance effects dominate and, consequently, the streaming current increases nearly quadratically with flow rate.

## Experimental

Liquid water microjets are produced by pressurizing water behind a thin metal orifice. Figure 1 presents the experimental design, as well as an enlarged view of the interface, illustrating the electrokinetic charge separation process. The jet orifice is a Pt-Ir electron microscope aperture (Ted Pella Inc.) that is pressed between two stainless steel plates. Clean water (18.2 M $\Omega$  cm, Millipore Milli-Q filtered) is nitrogen-purged and vacuum degassed prior to being pressurized and forced through the aperture with a Jasco PU-2089 HPLC pump. Jet velocity is controlled by changing the volumetric flow rate at the pump (velocity (m/s) = flow rate (m<sup>3</sup>/s) / area (m<sup>2</sup>)). The pump also measures the backing pressure and this pressure is used in Bernoulli's equation to calculate the jet

velocity. The diameter of the jet is determined by matching the velocities calculated from these two methods.

Streaming currents are measured at both the jet nozzle and at a downstream copper plate (2-10 cm from nozzle) that serves as the jet target. At the nozzle, the current,  $I_s$ , is fed into a Keithley 428 current amplifier and the resulting signal is recorded by a computer. Current at the target,  $I_L$ , is recorded in the same manner, with the addition of a variable resistor,  $R_L$  (0-200 Gohms) before the amplifier. Both the nozzle and target are insulated from all other electrical contacts with protective Teflon sheets. For efficiency calculations, the backing pressure and volumetric flow rate from the pump are also recorded as the resistance is stepped from 0 to 200 Gohms in increments of 10 Gohms. This process is repeated at a variety of flow rates and for three different aperture diameters.

## Results and Discussion

The apertures used in the experiments were determined to be 5.6, 10.3, and 19.1  $\mu\text{m}$  in diameter and were all within the 1  $\mu\text{m}$  diameter tolerance from the manufacturer. Hereafter, the apertures are referred to by their nominal diameters of 5, 10, and 20  $\mu\text{m}$ , respectively. Figure 2 gives the streaming current data measured at the nozzle for each aperture. As a result of the undeveloped flow conditions in the aperture, there is a nearly quadratic increase in streaming current with increasing fluid velocity. In addition, there is a clear increase in the magnitude of the streaming current as a function of jet diameter. This increase is proportional to the increase in metal-water interfacial surface area, i.e. aperture circumference.

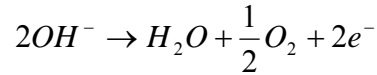
The solid lines in the figure are the best fits to the data using Equation 2, with  $\zeta$  as the only adjustable parameter. Equation 2 yields zeta potentials of -0.108, -0.135, and -0.105 V for the 5, 10, and 20  $\mu\text{m}$  jets, respectively. The accuracy of these measured zeta potentials depends not only on the use of correct aperture diameters, but also on the proper application of double-layer and flow-profile theory. For example, the temperature dependent data in the previous section indicated that viscosity changes as a function of distance from the interface. However, only a single value for viscosity is used to calculate the currents. In spite of the simple models used to develop Equation 2, the excellent fit to the data offers self consistent evidence for the accuracy of both the aperture sizes as well as the zeta potentials themselves. Accordingly, the average of  $-0.12 \pm 0.02$  V is a reasonable estimate of the potential at the shear plane of the water-Pt interface.

In traditional streaming current experiments, the conductive nature of metals gives rise to Faradaic depolarization currents that can cause inconsistencies when measuring electrokinetic properties.[18] Oosterman[19] found the streaming currents from platinum to give particularly irreproducible results and “the tentative explanation correctly referred to the need for controlling the discharge of protons and hydroxyl ions...”[18] Streaming currents from liquid microjets eliminate or minimize Faradaic depolarization currents and give spatial control over the discharge of protons and hydroxide ions. Consequently, liquid microjet techniques may prove to offer accurate measurements of electrokinetic properties for conducting materials.

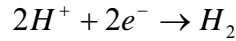
It should be noted that the signs of the currents imply that negative ions discharge at the nozzle interface while positive ions travel downstream and discharge at the target.

Ostensibly due to their large inductive interactions, anions are known to specifically absorb to electrode surfaces. When pure water is used as the electrolyte, auto-dissociated hydroxide ions absorb to the nozzle interface while the associated hydrated protons form the diffuse portion of the double layer. It should also be noted that although Pt-Ir apertures were used, Molybdenum apertures give similar currents and it is unlikely that catalytic effects are responsible for the current generation process. Previous experiments indicate that metals have similar electrokinetic charge generation rates.[13] Adding electrolytes decreased the electrokinetic charge generation rate.

Tangential fluid flow shears the hydrated protons from the surface and leaves unbalanced hydroxide ions at the metal-water interface. Excess, unbalanced charge at the interface induces the hydroxide ions to discharge into the metal and the observed current at the nozzle may be generated according to the process



Similarly, the liquid jet is enriched in unbalanced hydrated protons that extract electrons from the jet target electrode. As discussed in the previous section, reduction of the protons at the metal target leads to production of molecular hydrogen.[11]



When there is no added resistance in the target circuit, the current measured at the target is always equal in magnitude and opposite in sign to the current at the nozzle; that is, when  $R_L = 0$ ,  $I_s = -I_L$ . For a given aperture and flow rate, the nozzle current or the current at the target at zero resistance represent the maximum amount of charge available for energy conversion. Figure 3 shows  $I_s$  and  $I_L$  for the 20  $\mu m$  aperture at a flow rate of 2.5 ml/min. The sign of the target current has been inverted for clarity.  $I_s$ , in figure 3 is invariant while  $I_L$  decreases with resistance. The constant current at the nozzle suggests that external fields from the target reservoir do not interfere with the charge generation process and are not responsible for the decrease in  $I_L$  with  $R_L$ .  $I_s$  data was collected simultaneously with  $I_L$  and used to create the streaming current plots in Figure 2.

Figure 4 is a bar plot and a line plot of  $I_L$  for the 20  $\mu m$  jet as a function of flow rate and resistance. Figure 4 is similar to Figure 3, without  $I_s$  data, and with multiple flow rates. The lower panels of Figure 4 display the calculated voltage across the load resistor. A close inspection of Figure 4 reveals that, for the two lowest flow rates,  $I_L$  remains constant while the voltage increases linearly as a function  $R_L$ . Physically, protons from the liquid jet discharge at the target reservoir. As the resistance to the flow of charge increases, the target reservoir collects more hydrated protons and the voltage increases. In accordance with Ohm's law, the increased voltage compensates for the increased resistance and the current remains constant. For the higher flow rates, the linearity of Ohm's law breaks down and the voltage increases nonlinearly until a maximum of ~23 kV is reached. At these higher flow rates, charge is added to the target reservoir faster than it can dissipate through the load resistor. Under these conditions, the reservoir becomes 'filled' with charge and the voltage reaches a maximum. When the maximum voltage is reached, the current decreases linearly with increasing resistance.

The decreasing current at the target in conjunction with the constant current at the nozzle necessitates the existence of an alternate charge dissipation path that becomes available at high voltages. That is, when the reservoir becomes 'filled,' charge can leak out, possibly by the ionization of ambient air or conduction along the surface of the

receiving vessel. Figure 5 shows a possible circuit diagram that includes an alternate dissipation path in terms of a system resistance,  $R_{\text{sys}}$ , and current,  $I_{\text{sys}}$ . In other words, as the charge/voltage at the target increases, new dissipation pathways become available and/or alternate channels become more favorable. Consequently,  $R_{\text{sys}}$  is a complicated function of  $R_L$ . Moreover, the new dissipation pathways seem to limit the maximum voltage to  $\sim 23$  kV, although it may be possible to increase this value with better insulation techniques. To maintain charge neutrality, the system current and load current,  $I_L$ , must sum to the constant nozzle current,  $I_L + I_{\text{sys}} = I_s$ .

Despite the power losses in the system, knowledge of  $I_L$  and  $R_L$  permit straightforward calculations of power generation and conversion efficiency. Figure 6 shows the plots of both power and efficiency for the three jet diameters measured as a function of flow rate and load resistance. The power scales directly with resistance and with the square of the current. Consequently, for the lower flow rates, where the current remains constant, the power increases linearly with resistance. At higher flow rates, the decreasing current competes with the increasing resistance and for each flow rate the power reaches a maximum. Additionally, the power production is related to the amount of charge that can be separated in the nozzle and, as a result, the peak power should scale with the aperture diameter.

Figure 7 plots the peak power for the three apertures and confirms not only that the highest power is obtained with the largest aperture, but also that there is a linear relationship (correlation coefficient,  $r = 0.999$ ) between peak power production and aperture diameter. Despite the fact that the peak values were found at different velocities and resistances, the linear relationship suggests that the maximum power obtainable for an aperture is directly related to the metal-water interfacial surface area.

The efficiency plots, lower panels in Figure 6, show the same functional form as the power plots, only weighted towards the lower flow rates. The efficiency is simply the power divided by the volumetric flow rate and backing pressure. At a given flow rate, the pressure remains constant and, consequently, the efficiency has the same form as the power, simply scaled according to the flow rate and pressure. As a result, the efficiency involves a competition between the increase in power with aperture size and the corresponding increase in flow rate. Increases in channel diameter necessitate increases in flow rate that scale with the open aperture area (area  $\propto$  diameter<sup>2</sup>). Consequently, the larger diameter apertures require inordinately larger flow rates to obtain the associated increases in power. This leads to a decrease in efficiency, as a larger fraction of the hydrodynamic driving power is “wasted”. Figure 7 also plots the peak efficiency for the three jet diameters. The peak efficiency increases along with peak power when going from the 5  $\mu\text{m}$  jet to the 10  $\mu\text{m}$  jet, but decreases upon moving to the 20  $\mu\text{m}$  jet due to the associated increase in flow rate. For the limited number of jet diameters measured in this study, a maximum efficiency of 10.7% is obtained from a 10  $\mu\text{m}$  diameter jet.

The metal aperture yields a current that is always equal in magnitude and opposite in sign to the current at the downstream target. In addition, separate observations have shown that the current at the target is independent of whether the nozzle is electrically grounded or floating, i.e. voltage can build up on the jet nozzle without affecting the current generation process. These observations imply that resistors placed in the nozzle circuit may be used to create additional electrical energy without affecting the conversion process at the target and without requiring additional mechanical input energy. In

addition, further increases in efficiency may be realized by maximizing surface area at the expense of cross sectional area, i.e. rectangular jets.

The electronic properties of liquid water microjets create what is essentially a high voltage, low current battery.[2] Although the corresponding circuit diagram is useful, it should be remembered that the current generation technique is unusual. In a battery or photovoltaic cell, open circuit conditions will increase the potential and eventually halt the current generation process. In contrast, an open circuit does not affect the charge separation process in a liquid microjet and the maximum voltage should only be limited by the ability of the receiving vessel to hold unbalanced charge. In this way, the voltage that drives the energy conversion process could be used separately for the upstream and downstream circuits.

## **Conclusions**

Liquid microjets, created by forcing water through a small metal orifice, offer marked advantages over the use of channels and porous materials for electrokinetic power generation. By creating a jet of water that breaks up (via Rayleigh instabilities) before reaching the receiving reservoir, both surface conduction and bulk conduction, which otherwise limit conversion efficiency, are eliminated. In addition, the thin metal orifice creates flow conditions wherein entrance effects dominate. Consequently, the streaming current increases nearly quadratically with flow rate, whereas the laminar flow conditions obtained in channels and porous plugs affect only a linear current increase with flow rate. Using a liquid microjet, accumulated charge can only dissipate through the load resistor, and conversion efficiency is significantly increased with respect to channels and porous plugs. However, at high load resistance, sufficient voltage is produced to allow additional dissipation pathways. Despite these high voltage leakage currents, conversion efficiencies above 10% can easily be realized with liquid microjets, and considerable higher values should be achievable with optimization.

## Figures

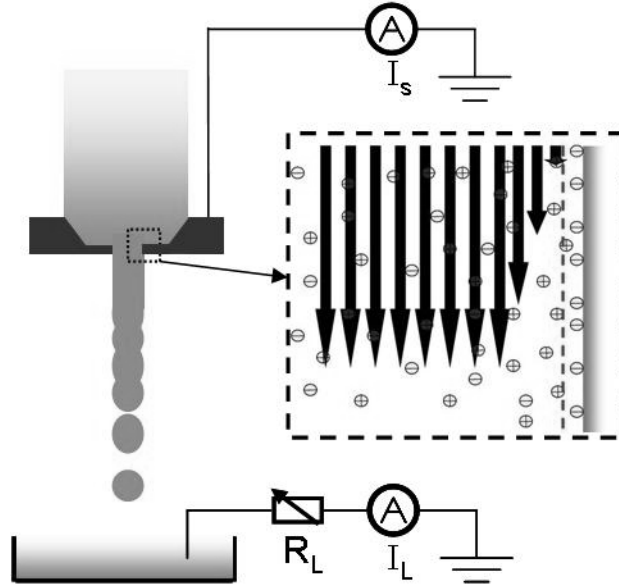


**Figure 1:** Experimental design; the expanded view shows details of the electrokinetic charge separation process

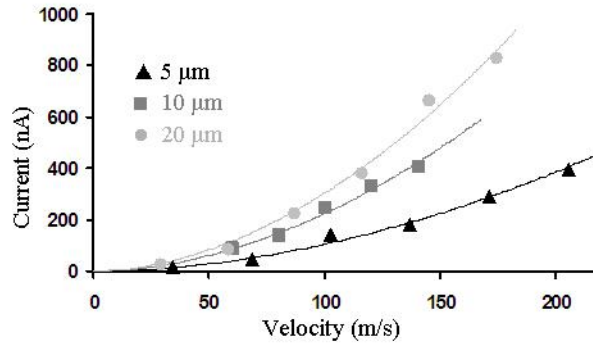


**Figure 2:** Data points indicate streaming current measurements, taken at the jet nozzle, for 5  $\mu\text{m}$  (▲), 10  $\mu\text{m}$  (■), and 20  $\mu\text{m}$  (●) diameter apertures. The solid lines are the best fits to the data using Equation 2, with zeta potentials calculated to be -0.108 V, -0.135 V, and -0.105 V for each diameter, respectively.

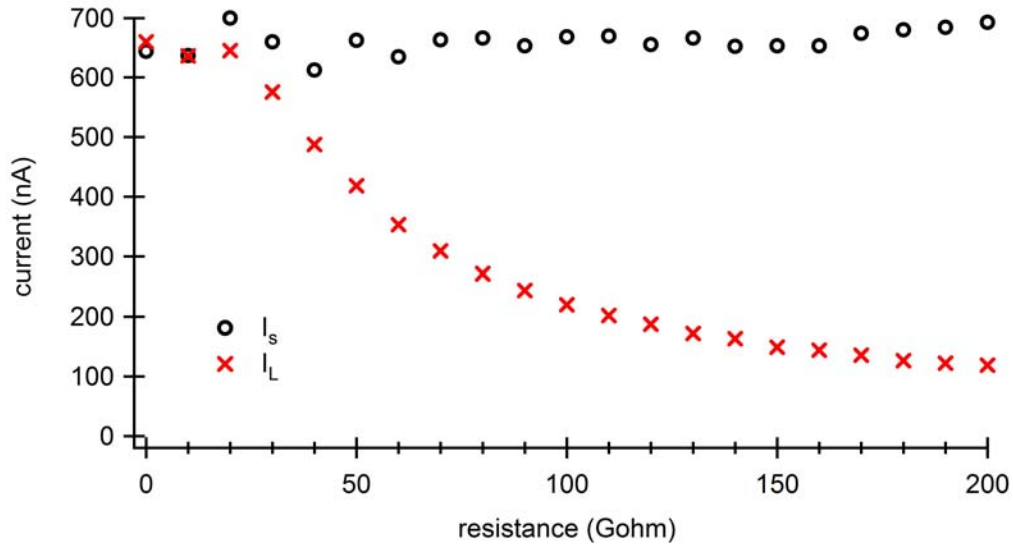


**Figure 3:** Streaming currents collected at the jet nozzle,  $I_s$ , and at the downstream target  $I_L$ . The streaming current at the nozzle is constant, implying that the charge generation process is constant. The target current that dissipates through the load resistor decreases with resistance.



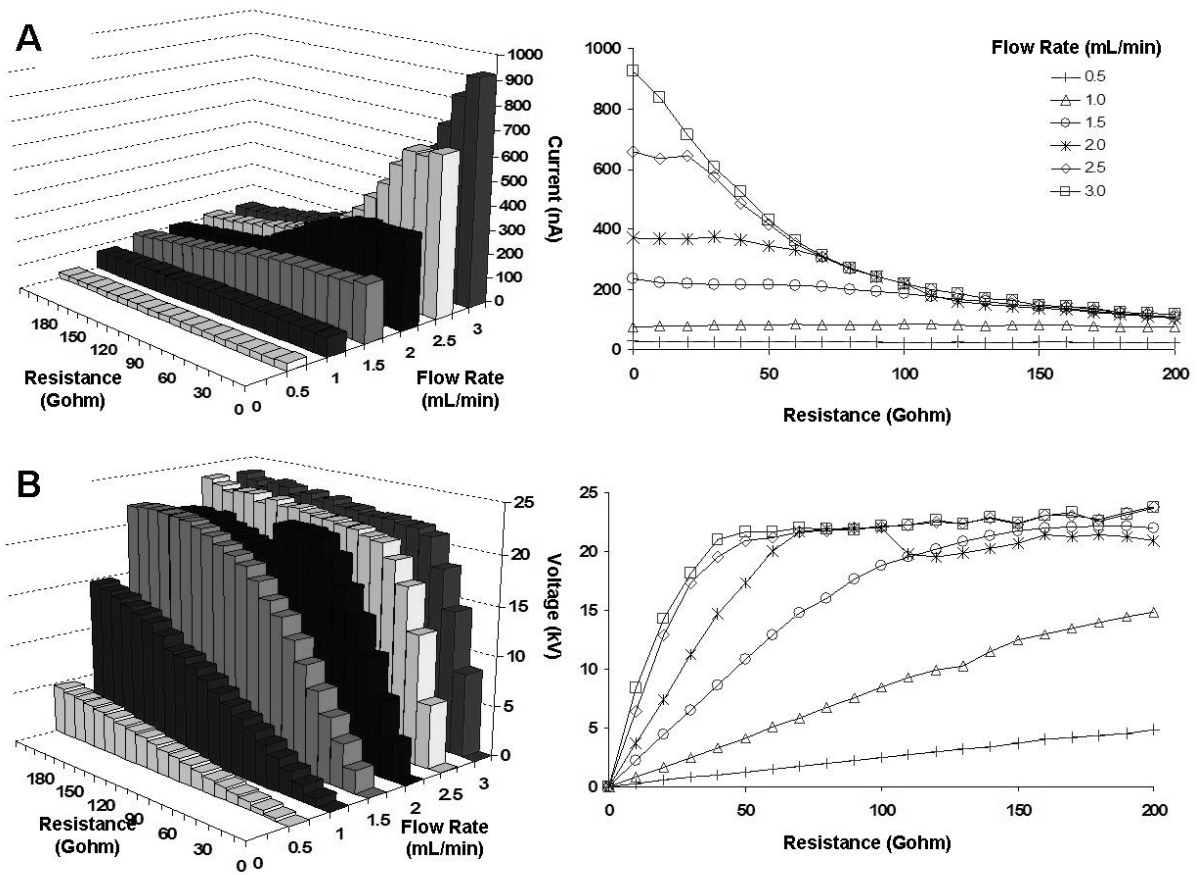


**Figure 4:** A) Inverted target currents from a 20  $\mu\text{m}$  diameter jet measured as a function of flow rate and resistance. B) Calculated voltage at the jet target from a 20  $\mu\text{m}$  diameter jet as a function of  $I_L$ ,  $R_L$ , and flow rate. For the low flow rates, voltage changes linearly with  $R_L$ . For higher flow rates, a maximum voltage is reached and thereafter  $I_L$  changes linearly with  $R_L$ .

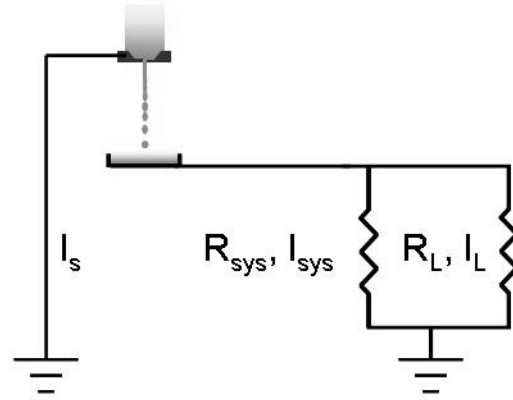


**Figure 5:** Equivalent circuit for power generation from an electrokinetic microjet system.  $I_L$  and  $R_L$  are the current and resistance through the load resistor used to calculate conversion power and efficiency, while  $I_{sys}$  and  $R_{sys}$  are the current and resistance associated with system losses.

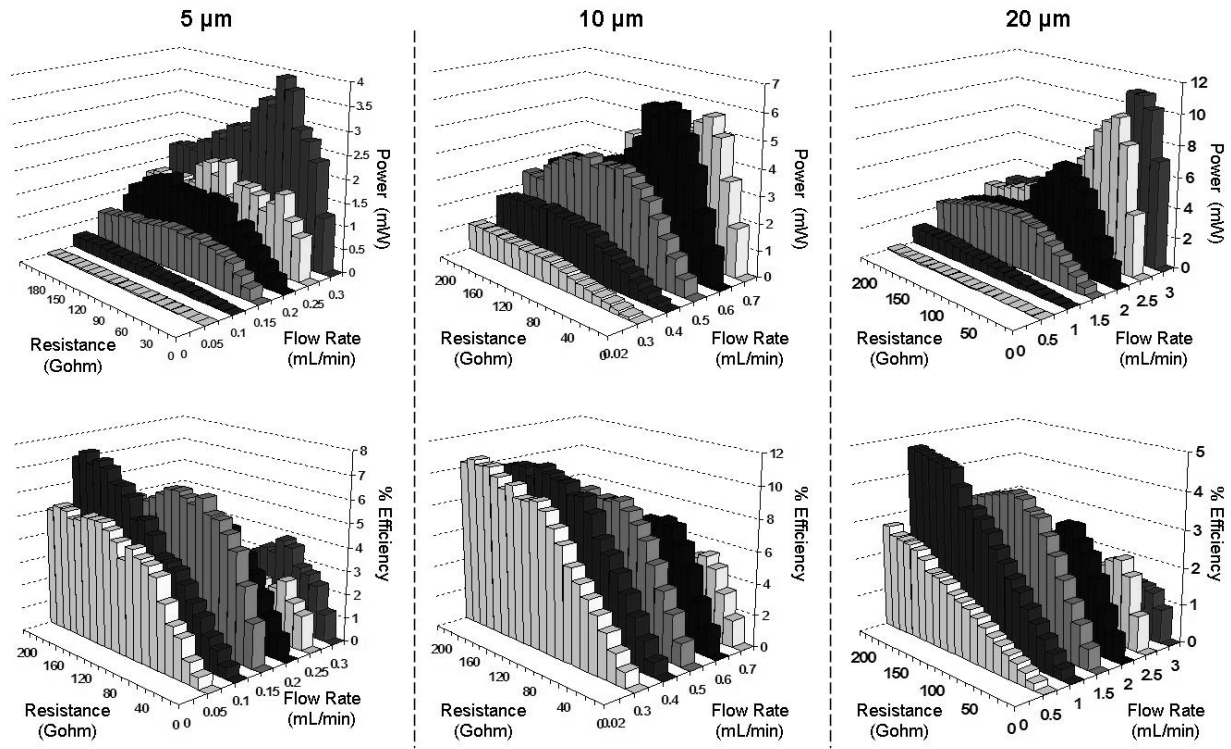


**Figure 6:** Plots of power (top panels) and conversion efficiency (bottom panels) for 5, 10, and 20  $\mu\text{m}$  diameter jets (left to right). Both power and efficiency are plotted as a function of flow rate and resistance. Peak power increases with increasing aperture diameter, noting that the electrical power is only generated at the metal-water interface. Peak efficiency reaches a maximum at the intermediate diameter due to the interplay between increased power production and increased volumetric flow rate.

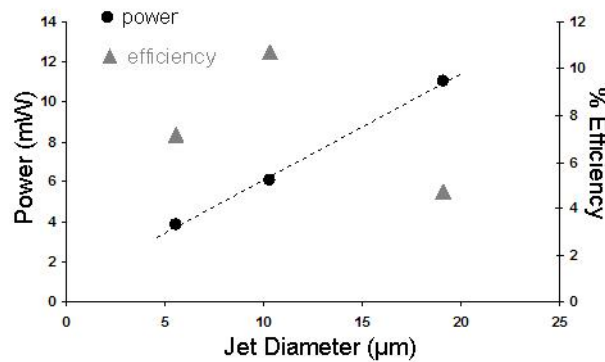


**Figure 7:** Peak power (●) and energy conversion efficiency (▲) measurements for 5, 10, and 20  $\mu\text{m}$  diameter jets (Data taken from the complete plots shown in Figure 5). Peak power increases linearly with jet diameter while peak efficiency is greatest at 10  $\mu\text{m}$ .

## References

1. Pennathur, S., J.C.T. Eijkel, and A. van den Berg, *Energy conversion in microsystems: is there a role for micro/nanofluidics?* Lab on a Chip, 2007. **7**(10): p. 1234-1237.
2. Yang, J., et al., *Electrokinetic microchannel battery by means of electrokinetic and microfluidic phenomena*. Journal of Micromechanics and Microengineering, 2003. **13**(6): p. 963-970.
3. Yang, J., et al., *Electrokinetic power generation by means of streaming potentials: A mobile-ion-drain method to increase the streaming potentials*. Journal of Nanoscience and Nanotechnology, 2005. **5**(4): p. 648-652.
4. Olthuis, W., et al., *Energy from streaming current and potential*. Sensors and Actuators B-Chemical, 2005. **111**: p. 385-389.
5. van der Heyden, F.H.J., D. Stein, and C. Dekker, *Streaming currents in a single nanofluidic channel*. Physical Review Letters, 2005. **95**(11).
6. van der Heyden, F.H.J., et al., *Electrokinetic energy conversion efficiency in nanofluidic channels*. Nano Letters, 2006. **6**(10): p. 2232-2237.
7. van der Heyden, F.H.J., et al., *Power generation by pressure-driven transport of ions in nanofluidic channels*. Nano Letters, 2007. **7**(4): p. 1022-1025.
8. Daiguji, H., et al., *Electrochemomechanical energy conversion in nanofluidic channels*. Nano Letters, 2004. **4**(12): p. 2315-2321.
9. Werner, C., et al., *Extended electrokinetic characterization of flat solid surfaces*. Journal of Colloid and Interface Science, 1998. **208**(1): p. 329-346.
10. Morrison, F.A. and J.F. Osterle, *Electrokinetic Energy Conversion in Ultrafine Capillaries*. Journal of Chemical Physics, 1965. **43**(6): p. 2111-&.
11. Duffin, A.M. and R.J. Saykally, *Electrokinetic hydrogen generation from liquid water microjets*. Journal of Physical Chemistry C, 2007. **111**(32): p. 12031-12037.
12. Rice, C.L. and R. Whitehead, *Electrokinetic Flow in a Narrow Cylindrical Capillary*. Journal of Physical Chemistry, 1965. **69**(11): p. 4017-&.
13. Gavis, J. and I. Koszman, *Development of Charge in Low Conductivity Liquids Flowing Past Surfaces - Theory of Phenomenon in Tubes*. Journal of Colloid Science, 1961. **16**(4): p. 375-&.
14. Delgado, A.V., et al., *Measurement and interpretation of electrokinetic phenomena*. Journal of Colloid and Interface Science  
Elkin 06, International Electrokinetics Conference, June 25-29, Nancy, France, 2007. **309**(2): p. 194-224.
15. Min, J.Y., E.F. Hasselbrink, and S.J. Kim, *On the efficiency of electrokinetic pumping of liquids through nanoscale channels*. Sensors and Actuators B-Chemical, 2004. **98**(2-3): p. 368-377.
16. Lyklema, J., *Surface conduction*. Journal of Physics-Condensed Matter, 2001. **13**(21): p. 5027-5034.
17. Davidson, C. and X.C. Xuan, *Effects of Stern layer conductance on electrokinetic energy conversion in nanofluidic channels*. Electrophoresis, 2008. **29**(5): p. 1125-1130.

18. Duval, J.F.L., et al., *Faradaic depolarization in the electrokinetics of the metal-electrolyte solution interface*. Journal of Colloid and Interface Science, 2003. **260**(1): p. 95-106.
19. Oosterman, J., *Thesis*. 1937, University of Utrecht: The Netherlands.

## 2.3 Photoelectrokinetics and Electrokinetic Spectroscopy

### Introduction

Electrokinetic energy conversion[1] and hydrogen generation[2] are both limited by low currents. The high voltages involved drive up the conversion efficiency, but currents in the nanoamp range with kilovolt potentials are not easily amenable to application. Coupling light into the electrokinetic charge separation process may be a means to improve the efficiency, by exploiting the high voltages inherent in liquid jet electrokinetics.

Traditional photovoltaic devices rely on the creation of a p-n junction and the associated electric field to separate photogenerated electron hole pairs. Briefly, when p-type and n-type semiconductors are brought in contact, the mobile electrons from the n-type semiconductor diffuse into the p-type semiconductor. At the same time, mobile holes from the p-type semiconductor diffuse into the n-type semiconductor. As a result, the interface naturally establishes a charge and electric field. The electric field counteracts further electron-hole diffusion and equilibrium is established across the junction. In other words, charge is transported across the interface until the Fermi energy (chemical potential) is the same on both sides. Charge carriers, both electrons and holes, are depleted in the interfacial region, known as the space charge region. Photogenerated excitons created in the space charge region are separated by the electric field and, when a circuit is present, create a current[3]. This is the basis of photovoltaic cells.

Similar processes occur at semiconductor-electrolyte interfaces. As the electrolyte and semiconductor are placed in contact, charge transfers across the interface until equilibrium is established between the semiconductor Fermi level ( $E_F$ ) and the redox system Fermi level ( $E_{R,redox}$ ) in the liquid[4, 5]:

$$E_F = E_{F,redox} \quad (1)$$

This transfer of charge establishes a potential drop across the interface. With metal-electrolyte interfaces, discussed in previous sections, the potential drop is entirely on the electrolyte side and results in an electrical double layer in solution. With semiconductors, wherein the charge carrier density is much lower than in metals, the potential drop occurs partly in the liquid and partly in the semiconductor, i.e. a space charge region is created in the semiconductor. The basis of photoelectrochemistry is to exploit the photogenerated electrons and holes separated in this space charge region to do chemistry. Considerable research has been done in this regard, especially on photocatalytic water splitting[6, 7]. Photoelectrokinetics, on the other hand, is relatively unstudied and integrates the overlap of a fluid flow profile with the double layer in order to modify/enhance the space charge layer. Figure 1 shows a representation of the photoelectrokinetic processes involved. Photoelectrokinetic spectroscopy is a novel approach to obtaining a relatively surface sensitive spectrum of a dissolved molecule or ion through photo-excited changes in the electrokinetic current.

In line with electrokinetic charge separation discussed in previous sections, water flowing rapidly across a semiconductor-liquid interface separates interfacial charges. As charge of one sign is preferentially carried downstream, the chemical potential (or redox potential) of the liquid is altered. This changes the potential at the solid-liquid interface.

As a result, the space charge layer in the semiconductor is modified. Equation 2 relates the width of the space charge layer,  $W$ , with the surface potential,  $\phi_s$ , the permittivity of the medium,  $\epsilon\epsilon_o$ , the unit charge,  $e_o$ , and the concentration of charge carriers,  $N_D$  [4]:

$$W = \sqrt{\frac{2\phi_s \epsilon\epsilon_o}{e_o N_D}} \quad (2)$$

Considering the large voltages obtainable with liquid water microjets[1] (tens of kilovolts), it is possible to achieve considerable enhancement of the space charge layer. This would increase the effective volume in which light-generated electron-hole pairs could be separated and, hence, the efficiency of the light collection.

Electrokinetic spectroscopy does not seek to modify the space charge layer in a semiconductor; rather it seeks to modulate the electrokinetic current through photo-generated changes in the electric double layer. Ionization of a liquid or solute molecule near a solid-liquid interface would change the anisotropic charge distribution of the electric double layer. As a result, the electrokinetic current measured downstream would change. The changes in current would track the absorption characteristics of the liquid or solute to give an absorption spectrum. This spectrum would only have contributions from molecules near the surface, since electrokinetic currents are only in the interfacial region.

## Experimental

In order to couple light into the electrokinetic process, it was necessary to fabricate glass microchannels and bond these channels to a semiconductor surface. All fabrication work was conducted in the Microfabrication Laboratory at the University of California, Berkeley. The fabrication follows standard glass etching techniques, outlined below. Amorphous, polycrystalline silicon, approximately 2 nm thick, was deposited onto both sides of a 4 inch diameter Pyrex glass wafer. The silicon on the wafer is then silanized with HDMS to promote photoresist adhesion, after which a thin layer ( $\sim 2 \mu\text{m}$ ) of photoresist is spun onto the wafer. Light from a Hg vapor lamp is used to expose the photoresist through a mask and the exposed resist is removed with photoresist developer. The exposed silicon is then removed with  $\text{SF}_6$  in a plasma etching chamber, revealing the glass substrate below. The remaining photoresist is removed with acetone after which the glass itself is etched by immersion in a concentrated HF acid solution. After the glass channels are etched the remaining silicon is removed in the plasma etching chamber.

Access holes are drilled from the back side of the glass wafer to conduct water to the channels. Next, the wafer is diced to separate the channels. A silicon wafer is diced to similar dimensions and the glass channel is anodically bonded to the silicon. The silicon-glass channel is compressed in a stainless steel holder and an o-ring forms a seal around the drilled access hole. Water is fed into the channel with an HPLC pump. Figure 2 is a diagram of the glass-microchannel jet. The outlets of the channels are 50-200  $\mu\text{m}$  wide and 5-10  $\mu\text{m}$  high. Light is admitted to the channel through a notch in the end of the stainless steel holder. Light passes through the upper glass layer, through the water, and impinges on the silicon layer below.

Photoelectrokinetic behavior is investigated with either a tungsten-filament laboratory light or a HeNe laser. For both light sources, a shutter is used to block or allow light to pass to the channel. The shutter is operated continually at sub hertz frequencies, but the light sources were turned on and off in 5 minute intervals to check

the baseline. Figure 3 show a diagram of the experimental setup. The electrokinetic currents for the jet at both the upstream metal holder and downstream target were measured with picoammeters and recorded into a computer. The difference between the current measured with the light on and the current measured with the light shuttered is termed the difference current. Photoelectrokinetic spectroscopy measurements were made by impinging light from a tungsten-filament through a monochromator and onto the channel.

## Results and Discussion

Figure 4 shows current measurements (made in the dark) for two different channel jets, both nominally 50  $\mu\text{m}$  wide and 5  $\mu\text{m}$  high, as a function of backing pressure. The differences in current between the two can be attributed to the variance in channel height and width introduced in the dicing and fabrication process. Figure 4 plots the current measured upstream from the jet, but the downstream current was also measured. As with all electrokinetic currents, the downstream current was equal in magnitude and opposite in sign to the upstream current. The dashed lines in Figure 4 are the best fits to the data, included to highlight the linearity of the data. Micro- and nanofluidic systems are typically characterized by a linear dependence of the electrokinetic currents on flow rate due to laminar flow conditions.[8-10] However, the intercept of the data in Figure 4 is clearly non-zero. Electrokinetic currents are typically measured between two reservoirs connected by one or more channels. In the present experiments, currents cannot be measured until continuous liquid jet formation is established. Clearly, the slope of the electrokinetic current as a function of backing pressure is different in the microjet vs. two reservoir regimes. This difference is presumably due to the elimination of back conduction with jet formation.

The results from a photoelectrokinetic experiment are shown in Figure 5. The upper panel is a plot of the upstream streaming current as a function of time. The downstream current and photocurrent was equal in magnitude and opposite in sign. As indicated on the figure, there are clear changes in the baseline current with changes in flow rate. For the data in Figure 5, the HeNe laser ( $\sim 15\text{ mW}$ ) acting as the light source was alternately blocked or allowed to impinge on the channel in 5 minute intervals. Additionally, a laser shutter was opened and closed in 6 second intervals and the current integrated over the open shutter time was subtracted from the current integrated over the closed shutter time to give the difference current,  $I_d$ . Again, both the downstream streaming current and downstream difference current, not shown, were equal in magnitude and opposite in sign relative to the upstream quantities displayed. There is a clear increase in electrokinetic current when the light impinges on the channel and the increase in difference current tracks the increase in baseline current with flow rate.

The lower left panel of Figure 5 plots the averaged streaming current data and difference current as a function of flow rate. The lower rightmost panel plots the difference current divided by the streaming current,  $I_d \div I_s$ , for each flow rate. For the specific channel investigated, there was a fairly constant 7% increase in the measured electrokinetic current with HeNe illumination.

Measuring an increase in the photoelectrokinetic current upon illumination was commonly observed in these experiments and *some channels even gave significant current increases using only the ambient room lights for illumination!* But despite such



encouraging successes, the photoelectrokinetic measurements were plagued with inconsistency. A number of tested channels gave no observable increase in current upon illumination and some even exhibited small negative photocurrents. A single channel could also give changing results in time, i.e. positive current changing to no current or vice versa with time. To illustrate some temporal changes, Figure 6 shows the electrokinetic current from a channel at startup. After long times, the upstream current remains positive and the downstream current negative. However, as evident in Figure 6, the sign and magnitude of the current is a complicated function of time. With minutes in between changes in sign, chemical changes at the interface are likely involved with the sign reversals. Although not all channels measured gave such complicated initial behavior, the data shown in Figure 6 illustrates some of the inconsistencies leading to irreproducibility encountered while collecting photoelectrokinetic data.

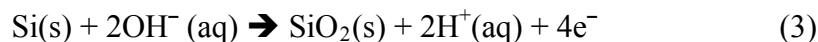
Another interesting aspect of photoelectrokinetics experiments involves the physical location of current collection. Figure 7 plots the upstream and downstream streaming currents and photocurrents (signs of the downstream currents were reversed for clarity). The nearly vertical changes in the streaming currents are results of changing the physical location of current measurements and serve to break the figure into 5 sections. The first, third, and fifth sections were measured by collecting the upstream current at both the metal holder and the exposed silicon wafer. These sections serve as baselines. The second section of Figure 7 measures the current at the exposed silicon by attaching a clip to the silicon with the metal holder grounded. The downstream current remains constant, indicating no change in the current generation process, but the upstream current drops to a fraction ( $\sim 1/7$ ) of the downstream current. Correspondingly, the upstream difference current drops to near zero while the downstream difference current remains constant. These data indicate that the majority of the upstream current, and all of the photocurrent, is discharged in the upstream metal holder.

The fourth section of Figure 7 depicts the upstream current at the holder with the silicon wafer grounded. The increase in upstream current in this configuration is probably due to a grounding loop introduced with grounding the silicon. In spite of this small increase, the difference current remains nearly the same compared to the baseline sections. Again, this suggests that nearly all the photocurrent is collected upstream of the channel. The relatively slow migration of photoelectrokinetic current from the channel to the upstream holder precludes the use of lock-in-amplification and is the reason for the sub-Hertz integration times used in these experiments.

One obvious reason for current migrating upstream from the nozzle to discharge, rather than discharging into the silicon, is the development of an insulating oxide coating on the silicon. In this scenario, no charge crosses the oxide layer. Rather, the light changes the potential in the solid upon the creation of electron-hole pairs. If charge is not allowed to cross the solid-liquid interface, electron-hole pairs separated in the space charge layer will reduce the potential drop in this layer and, consequently, change the potential drop in the liquid. In other words, the photovoltage created under illumination affects the zeta potential and correspondingly, the electrokinetic charge generation process.

In a competing model, the creation and/or thickening of the surface oxide layer could itself be responsible for the photocurrents observed. Based on the signs of the current, positive charges are swept downstream out of the channel while negative

charges, presumable hydroxide ions, discharge upstream. Equation 3 shows the reaction of hydroxide ions with silicon to form silicon-oxide. This reaction constitutes a current doubling. Photo-generated electron-hole pairs are essentially broken bonds in the silicon. Consequently, light would facilitate the oxidation reaction with hydroxide ions and an increase in observed current. That is, current doubling from silicon oxidation could be responsible for the increased electrokinetic current under illumination. However, under this scenario, it would be expected to collect the current from the silicon rather than from the holder upstream.



The long term stability of the channels also indicates that oxidation reactions are prominent in the photoelectrokinetic process. Figure 8 shows the steaming current (top), pump backing pressure (middle), and difference current (bottom), for two channels run for an extended period of time (over 40 hours). In both cases, the jets ran at a fairly steady current and pressure before either clogging or rupturing the glass. The rise in pressure and streaming current, forced by the HPLC pump seeking to maintain a constant flow rate, before the channels stopped functioning indicates a narrowing of the channels, possibly due to volume expansion with oxidation. What is interesting is that for both channels shown in Figure 8, the difference current rises and peaks before the pressure rise. It is reasonable that channel constriction would follow photoelectrokinetic-assisted oxidation.

Initial attempts at collecting a spectrum of a solute by photoelectrokinetic spectroscopy were inconclusive. The electrokinetic current was collected as a function of light wavelength for a few  $\text{Cr}^{3+}$  and  $\text{Fe}^{3+}$  solutions. The ions were chosen because they have strong optical absorption in visible region, accessible with the lamp and monochromator used, but these were probably poor choices. While promoting an electron to an excited state of these highly charged cations is straightforward, ionization is unlikely and this would leave the double layer and electrokinetic current unchanged. A better solute choice for exploring photoelectrokinetic spectroscopy would be anions or cations that can be further oxidized. If the light source can excite and transfer an electron to the solvent, the likelihood of altering the electric double layer and electrokinetic current increases.

## Conclusions and Future Work

With silicon-glass channels, there is clear evidence for photo-enhanced electrokinetic currents. The photo-enhanced currents increase with the flow rate and are likely the result of an increased space charge layer. It is reasonable to assume that the photo-enhanced current is a result of current doubling associated with the oxidation of the silicon. However, the physical location of current collection gives evidence that no (or very little) charge is dissipated through the silicon; rather, the charge travels upstream in the liquid to dissipate through stainless-steel tubing in contact with the liquid. These observations lead to two models for photoelectrokinetic currents. The first is basic photo-assisted oxidation of the silicon. The second is based on a photo-voltage at the interface that alters the electrokinetic current, but with no charge actually crossing the silicon-water interface. In the second model, all charge migrates upstream for dissipation through a

conductor in contact with the liquid. Further experiments are needed to differentiate and/or confirm these models.

Other experiments could be designed to more completely understand the photoelectrokinetic process and current migration in these channels. With advanced microfabrication techniques the silicon surface could be patterned to collect current from individual pixels of a grid, similar to a CCD camera. In this way, a detailed picture of current generation and collection could be obtained.

As discussed above, further experiments are needed to confirm the feasibility of photoelectrokinetic spectroscopy. Initial experiments should focus on anions or oxidizable cations. Photoelectrokinetic spectroscopy would also greatly benefit from employment of a stable surface. This would eliminate potential complications from wavelength-dependent absorption and/or photo-oxidation of silicon. A large bandgap metal-oxide or a thin layer of metal could be used for this purpose.

## Figures

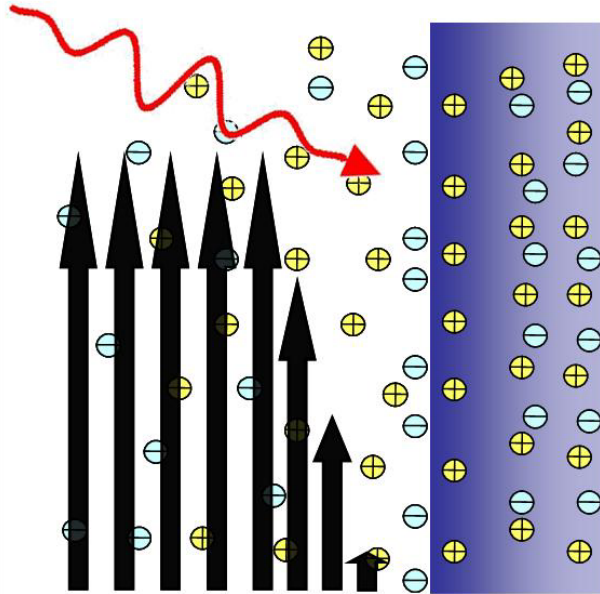


**Figure 1:** Diagram highlighting the electric double layer in the liquid and the space charge layer in the semiconductor. Pressure driven flow moves charge downstream in the liquid and the remaining, unbalanced ions in solution alter the space charge layer. Light generated electron-hole pairs created in the space charge layer can be separated by the associated electric field.

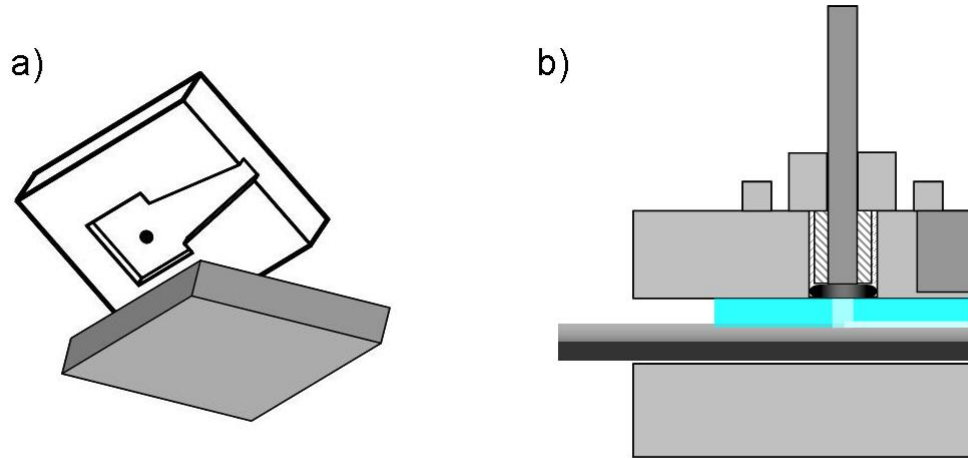


**Figure 2:** Section a is a model of the etched glass microchannel before anodic bonding to silicon plate. Water is fed into the channel through the access hole in the square receiving well. Section b is a cutaway of the channel in the stainless steel holder.

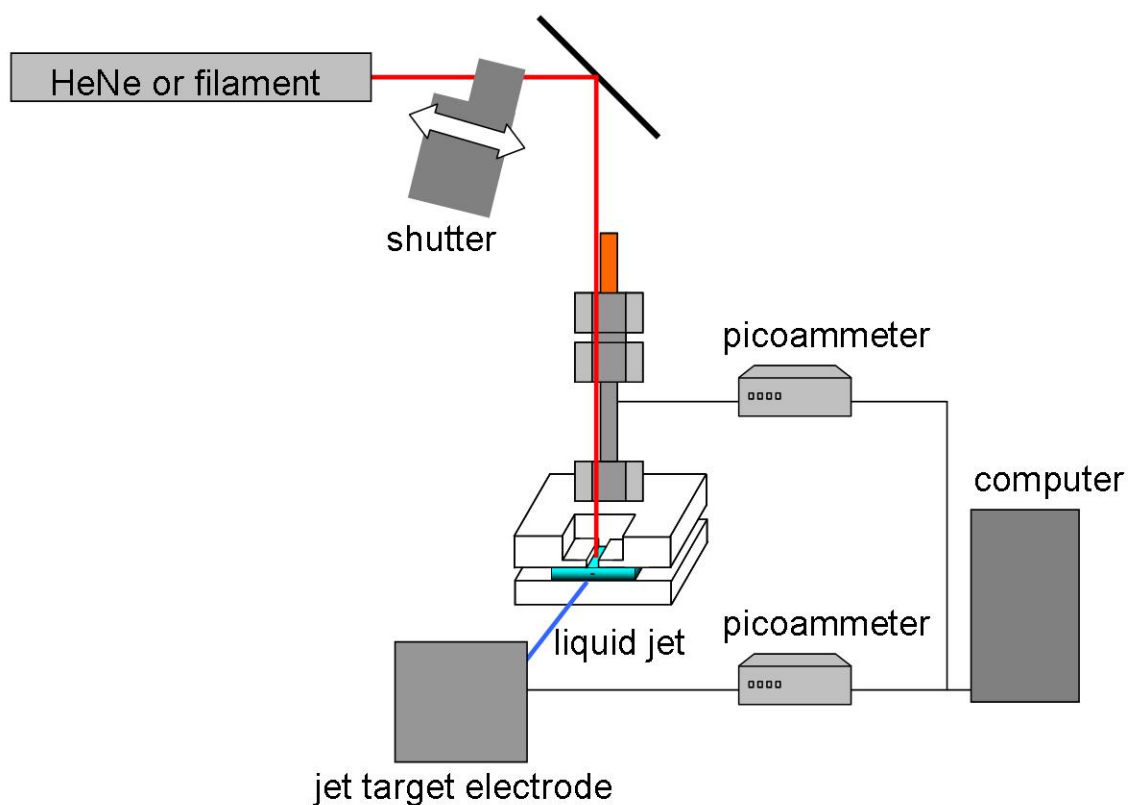


**Figure 3:** Diagram of photoelectrokinetic experiment. A liquid jet is formed at the end of a fabricated glass channel by pressurizing water with an HPLC pump. The upstream and downstream currents are measured simultaneously. Light from a HeNe laser or tungsten filament is modulated with a shutter and impinges on the end of the glass-silicon nozzle.

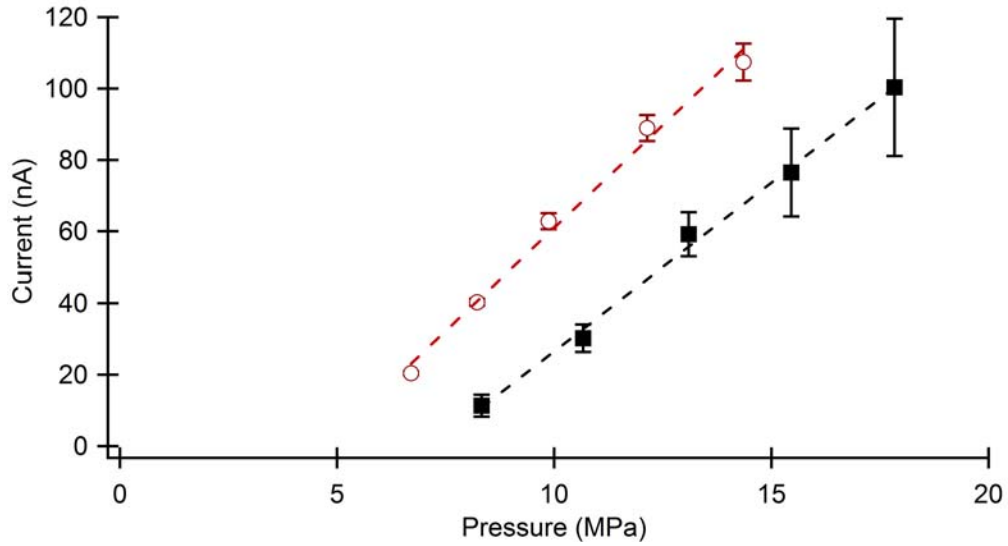


**Figure 4:** Current measured upstream from the channel jet as a function of water backing pressure. The current at the target (not shown) was equal in magnitude and opposite in sign. The open circles and solid squares respectively represent data from two separate channels, both nominally 50  $\mu\text{m}$  wide and 5  $\mu\text{m}$  high. The dashed lines are linear fits to guide the eye and emphasize the linear relationship between the pressure/flow rate and current that is due to laminar flow in the channel.

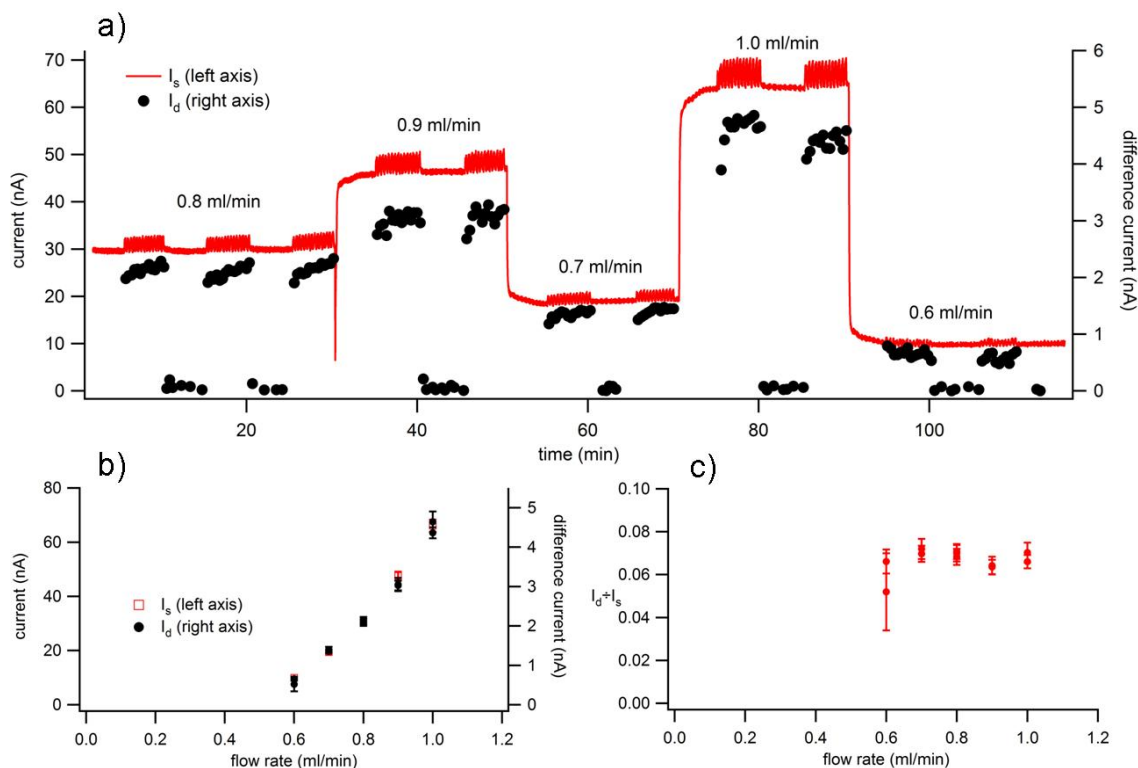


**Figure 5:** The top panel depicts the streaming current (line) and difference current (points) as a function of time and at different flow rates (flow indicated on graph). The difference current was collected continually, but the HeNe light source was blocked every other five minutes. There is clear photo-enhanced current when the light impinges on the channel. The lower left panel, b, replots the data from the top panel as a function of flow rate. Both the streaming current and the difference current scale linearly with flow rate. The lower right panel, c, shows the difference current divided by the streaming current. There was a fairly constant 7% increase in the current with illumination.



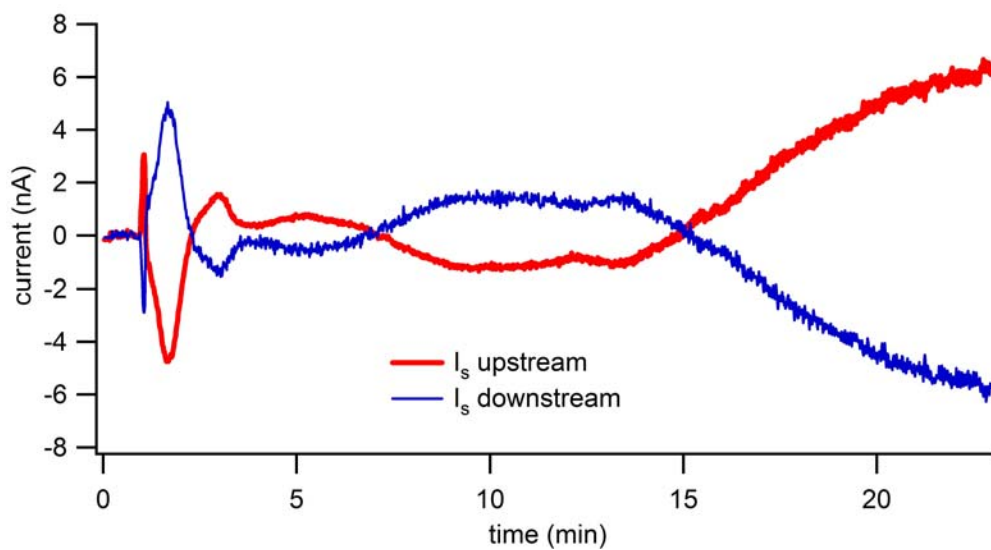


**Figure 6:** The upstream (thick red line) and downstream (thin blue line) streaming current for a channel measured at startup. The currents show a complicated reversal of sign the kinetics of which indicates chemical changes of the interface.

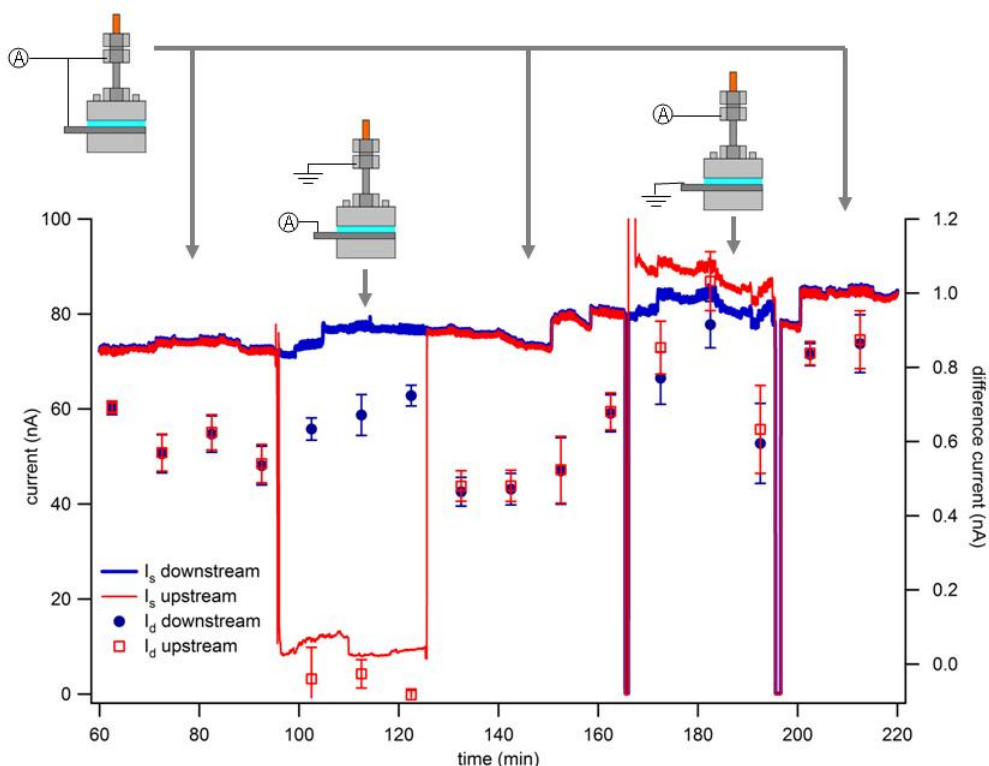


**Figure 7:** Streaming and difference currents as measured from different physical locations. The solid lines in the figure show the downstream (thick blue line) and upstream (thin red line) as a function of time. The downstream (blue dots) and upstream (red squares) difference currents are plotted on the secondary axis. The downstream current is fairly constant throughout the experiment, indicating that the current generation process is unaffected with the change in location of measurements. The upstream current is a fraction of the baseline and the upstream difference current nearly zero when measured through the silicon wafer, but almost unchanged when measured through the upstream metal connector. Most of the electrokinetic current and nearly all of the photocurrent are dissipated upstream from the channel interfaces.

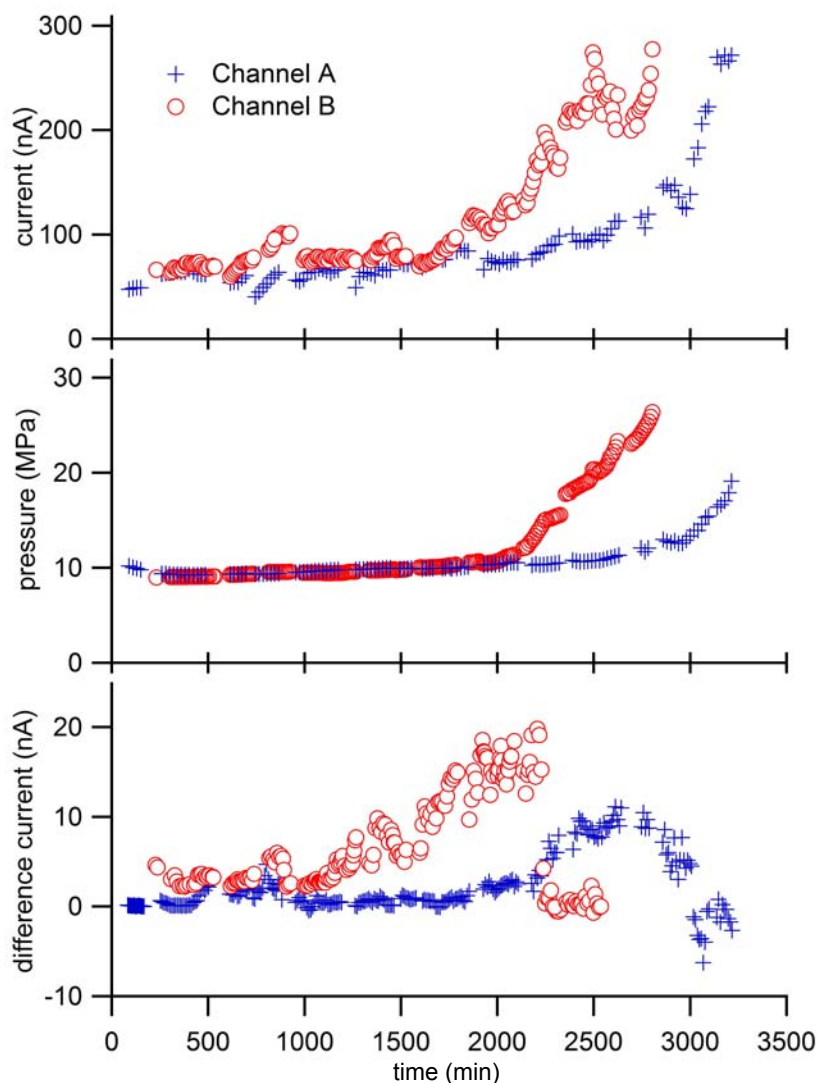


**Figure 8:** The long time characteristics of two photoelectrokinetic channels. The top plot is the streaming current for channels A (blue plusses) and B (red circles) and the middle plot is the backing pressure of the pump supplying water to the same channels. In both cases the backing pressure and current rise before the channel ruptures or clogs completely. The bottom graph is the difference current for the same channels. For both channels, there was a spike of photoelectrokinetic current immediately preceding the pressure and streaming current increases. The increased photo-oxidation could lead the constriction and ultimate failure of the channels.

## References

1. Duffin, A.M. and R.J. Saykally, *Electrokinetic Power Generation from Liquid Water Microjets*. Journal of Physical Chemistry C, 2008. **112**(43): p. 17018-17022.
2. Duffin, A.M. and R.J. Saykally, *Electrokinetic hydrogen generation from liquid water microjets*. Journal of Physical Chemistry C, 2007. **111**(32): p. 12031-12037.
3. Skoog, D.A., F.J. Holler, and T.A. Nieman, *Principles of instrumental analysis*. 1998, Philadelphia; Orlando, Fla.: Saunders College Pub. ; Harcourt Brace College Publishers.
4. Nozik, A.J. and R. Memming, *Physical chemistry of semiconductor-liquid interfaces*. Journal of Physical Chemistry, 1996. **100**(31): p. 13061-13078.
5. Licht, S., *Semiconductor electrodes and photoelectrochemistry*. 2002, Weinheim: Wiley-VCH.
6. Maeda, K. and K. Domen, *Photocatalytic Water Splitting: Recent Progress and Future Challenges*. Journal of Physical Chemistry Letters, 2010. **1**(18): p. 2655-2661.
7. Rajeshwar, K., et al., *Solar hydrogen generation toward a renewable energy future*. 2008, Springer: New York, NY.
8. van der Heyden, F.H.J., et al., *Power generation by pressure-driven transport of ions in nanofluidic channels*. Nano Letters, 2007. **7**(4): p. 1022-1025.
9. Choi, Y.S. and S.J. Kim, *Electrokinetic flow-induced currents in silica nanofluidic channels*. Journal of Colloid and Interface Science, 2009. **333**(2): p. 672-678.
10. Delgado, A.V., et al., *Measurement and interpretation of electrokinetic phenomena*. Journal of Colloid and Interface Science, 2007. **309**(2): p. 194-224.

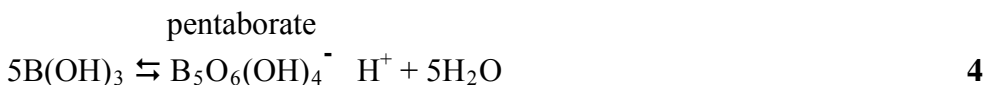
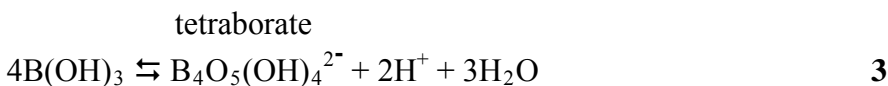
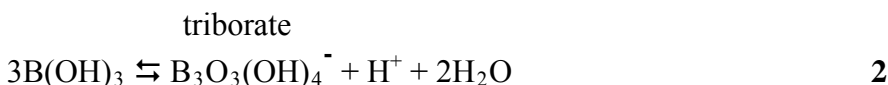
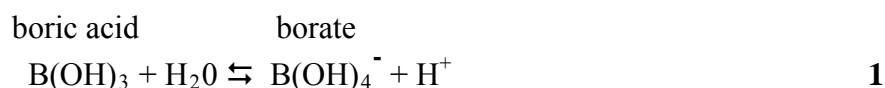
## Chapter 3: Boron Hydration

### 3.1 pH-Dependent X-ray Absorption Spectra of Aqueous Boron-Oxides

#### Introduction

In the past decade, considerable effort has been directed to the study of borohydrides as hydrogen storage materials[1]. Hydrolysis of borohydride produces molecular hydrogen and an oxygenated boron compound. In spite of these efforts, the DOE recently gave a ‘no-go’ recommendation for automotive sodium borohydride system[2, 3]. A significant factor contributing to this recommendation is the excess water required for hydration of hydrolysis reaction products, borate  $[B(OH)_4^-]$  in particular. Borate is significantly less soluble than borohydride, possibly due to the formation of polyborate ions, so excess water is required to keep borate in solution. The excess water reduces the wt % hydrogen storage, one of the main considerations for automotive fuels. In an effort to better understand the hydration of boron-oxides, we performed near edge X-ray absorption fine structure (NEXAFS) spectroscopy experiments to probe boric acid, borate, and polyborate ions in solution. We also compare the experimental boron spectra with calculated spectra generated using the recently developed excited electron and core hole (XCH) method[4].

In their own right, borate and boric acid  $[B(OH)_3]$  are interesting because they comprise an atypical acid/base pair. The change from acid to conjugate base is not a simple deprotonation, but instead involves a reaction with water and a change in boron coordination. In addition, at high concentrations ( $>0.025$  M), boric acid evolves through a series of polyborate anions as a function of pH, as evident in Reactions 1-4.



The reactions involved in aqueous boron chemistry have been extensively studied using NMR and electrochemical techniques[5-13]. Figure 1 depicts the speciation of boron compounds in a 0.5 molar boric acid solution as a function of pH, as derived from

published reaction constants[5-8]. The graph plots the fraction of total boron in each of the four species included in this study (pentaborate ion excluded due to low abundance).

Inspection of aqueous boric acid chemistry clearly shows that the water surrounding boron molecules is vital for the acid/base reaction and the formation of polyborate ions. Boric acid is a trigonal planar molecule with an empty 2p<sub>z</sub> orbital perpendicular to the molecular plane. The conjugate base, borate, is tetrahedrally coordinated. Water reacting with boric acid must hybridize the empty 2p<sub>z</sub> orbital. Consequently, aqueous boric acid would be expected to show considerable hydration-dependent effects compared to solid samples.

Moreover, sodium ions have been shown by a variety of techniques to associate with borate anions in aqueous solutions[14-17], Reaction 5. Beyond effects on solubility, sodium-borate association in water is significant because it affects speciation and isotopic fractionation. This information has been used to model water-rock interactions and to calculate the pH of ancient oceans[17-20]:



XAS spectra of boron-containing minerals and glasses have been studied previously[21-25]. The main peaks in mineral and glass boron samples, attributed to trigonal and tetrahedral boron, are sensitive to ratio of trigonal and tetrahedral boron as well as B-O bond length[21]. The main trigonal boron peak at 194 eV is attributed to the transition of an electron from the B 1s state to the unoccupied B 2p<sub>z</sub> orbital. A second trigonal boron peak at higher energy (204 eV), above the ionization potential (IP), is attributed to transitions from B 1s to unoccupied B-O sigma antibonding ( $\sigma^*$ ) orbitals. The main absorption feature in tetrahedral boron samples (197 eV) is just above the IP and is assigned to the transition of electrons from B 1s to B-O sigma antibonding states[23]. These unoccupied molecular orbitals, directly probed by NEXAFS, typically extend well beyond the excited boron atom/molecule. As a result, NEXAFS of these species should be sensitive to changes in local structure and environment, such as solvation, although, in this case, we find that it is not.

In this study, X-ray absorption spectroscopy (XAS) data for solvated boron compounds was collected using the liquid microjet technique. Microjets allow a thin filament of volatile liquid (~30  $\mu\text{m}$ ) to be injected directly into a high vacuum environment, permitting windowless coupling of the jet chamber to a synchrotron beamline. Incident x-ray photons intersect the liquid filament and the total electron yield (TEY) x-ray absorption spectra are collected with a biased copper electrode, yielding the absorption spectrum of the bulk liquid.

## Methods

### A. Samples

Boric acid with a stated purity of ~99.5% was obtained from FisherChemical and used without further purification. The pH of the 0.5 M boric acid solutions was adjusted with either NaOH or KOH and measured with pH paper. The water for all solutions had a resistivity of 18 M $\Omega$ /cm.

### B. NEXAFS spectroscopy

Boron K-edge total electron yield spectra were obtained on Beamline 8.0.1 of the Advanced Light Source at Lawrence Berkeley National Laboratory. A detailed description of the experimental endstation and data collection has been published elsewhere[26]. Briefly, the undulator at Beamline 8 produces an intense beam ( $>10^{11}$  photons/sec) of highly resolved ( $E/\Delta E > 4000$ ), tunable photons. The soft X-rays from the beamline are focused to a spot size of  $\sim 50\text{ }\mu\text{m}$  onto a liquid jet  $\sim 30\text{ }\mu\text{m}$  in diameter. The x-rays intersect the liquid just as it emerges from the nozzle, yielding a room-temperature absorption spectra. A major advantage of using a liquid jet is that sample volume is continually refreshing and, consequently, sample damage contamination of the measured signal is minimized. The jet itself is created by using a syringe pump (Teledyne-ISCO) to pressurize liquid behind a small piece of fused silica capillary that acts as the jet nozzle. Another advantage to using a liquid jet is that the endstation, with a few differential pumping sections, can be coupled directly to the beamline, without a flux reducing window.

The pressure in the chamber is kept low ( $10^{-4}$  torr) with turbomolecular pumps and by skimming and then cryotrapping the liquid jet. This working pressure is sufficiently low to allow for efficient and sensitive charged particle detection. XAS spectra were collected by incrementing the photon energy (0.2 eV step size) across the boron adsorption edge, 190-215 eV. The total electron yield, in this case providing a bulk measurement, was collected with a biased copper electrode located approximately 1 cm from the jet. The current from the electrode was amplified, converted to a voltage, and then converted to a frequency before being read into the beamline computer.

The TEY signals were normalized to the signal from a gold mesh ( $I^0$ )  $\sim 3$  meters upstream from the jet chamber. A background vapor spectrum, collected off jet, was also subtracted from each sample to correct the baseline. Multiple spectra for each sample were averaged and the resulting spectra area normalized for comparison. Photon energy was calibrated by collecting TEY spectra for solid boric acid.

### C. Calculations.

The ultrafast experimental core level excitation ( $\sim 10^{-18}$  s) essentially samples molecules in frozen structural configurations thermodynamically sampled from the accessible vibrational degrees of freedom. Consequently, the experimental spectra show peaks that are broadened due the thermally occupied vibrational levels (and zero point motion)[27, 28]. To accurately simulate the experimental measurements, multiple molecular dynamics snapshots sampling the natural range of vibrational motion need to be calculated and averaged. To accomplish the vibrational sampling, each molecule is solvated in a periodic box and Quantum Mechanics/Molecular Mechanics (QM/MM) simulations are run at 300 K (Langevin Thermostat) for 10 ns. The periodic boxes contained between 76 and 141 waters depending on the size of the solute. The MNDO hamiltonian was used for the QM calculations of the boron species and snapshots were collected every 100 ps. The nonbonding (Lennard-Jones) parameters for boron were taken from Pletnev[29].

For each of the 100 snapshots generated in the MD simulations, an X-ray absorption spectrum was calculated. The snapshot average was used as the final theoretical spectrum. The methods for calculating XAS spectra have been described previously[4, 27]. Briefly, density functional theory (DFT) employing a plane-wave

basis set and periodic boundary conditions was used to calculate spectra. The exchange-correlation energy was calculated within the generalized-gradient approximation with the Perdew-Burke-Ernzerhof exchange-correlations functional. A plane wave basis set was chosen to accurately predict both localized and delocalized states. The final electronic states were calculated using a boron pseudopotential with a core hole (electronic configuration  $1s^1 2s^2 2p^2$ ) and one extra valence electron. These excited electron and core hole (XCH) calculations explicitly include both the full core hole and the corresponding excited core electron promoted to the lowest energy available valence state. Self consistent charge densities and states were calculated using Plane Wave – Self Consistent Field (PWSCF) calculations on the Franklin supercomputer at the National Energy Research Scientific Computing (NERSC) Center. The transition amplitude was estimated using the single-particle and dipole approximations.

Boron K-edge NEXAFS spectra were calculated for boric acid, borate, triborate, and tetraborate. For the polyborate molecules spectra were separately calculated for the trigonal and tetrahedral boron species. All spectra were uniformly broadened with Gaussians of 0.2 eV full width at half maximum. To correct bandwidth underestimation within DFT, all calculated spectra were stretched along the energy axis by 10%. The calculated spectra were empirically aligned to experiment.

## Results and discussion

The solid lines in Figure 2 show boron K-edge NEXAFS spectra of 0.5 M boric acid solutions for a series of pH values. Similar to mineral and glass samples, solvated boron-oxides show three main spectral features. The lowest energy feature at 194 eV corresponds to the transition from a B 1s state to the empty B 2pz orbital of trigonal boron. As the pH increases, the percentage of trigonal boron decreases. For that reason, the intensity of the low energy peak decreases with increasing pH and is absent at high pH. Trigonal boron has a second broad feature centered around 204 eV that corresponds to transitions from B 1s to B-O sigma antibonding ( $\sigma^*$ ) orbitals. Tetrahedrally coordinated boron-oxides have only one broad absorption feature beginning at about 197 eV that matches with a transition from the B 1s to the B-O sigma antibonding states. As the pH increases, and with it the percentage of tetrahedral boron, the intensity of the feature at 197 eV increases.

The dotted lines in Figure 2 are the calculated spectra. The final calculated spectrum at a given pH is a linear combination of the spectra from individual species combined according to the ratios in Figure 1

In general, the calculated spectra are in excellent agreement with the experimental spectra; although, the high energy sides of the calculations do not reproduce the measured intensity. At these higher energies, multiple scattering resonances may contribute to the experimental intensity, whereas they are absent in the present calculations. In addition, the calculated intensities are too low at high energy due to difficulty in calculating the correct transition probabilities for these highly excited states, since only a limited number of excited states can be included. Furthermore, even though the energy axis has been stretched by 10%, the underestimation of the bandgap and energy scaling by DFT may also contribute to the decreased intensity of the calculated spectra compared to experiment at higher energies.



In addition, the high energy feature for the boric acid sample, pH 5, is broader than evident in the corresponding calculations. Given the propensity for boron-oxides to form polyborate ions, it is reasonable to expect considerable interaction between boric acid monomers. For concentrated boric acid/borate solutions, Ishihara et al.[9] attributed a coalesced NMR signal to a symmetrical dimer transition state between boric acid and borate. If present in sufficient concentrations, dimers similar to those proposed by Ishihara et al.[9] may give detectable concentrations of tetrahedrally bonded boron and result in the broad high energy feature observed in our experiments. The QMMM simulations used for the calculations did not account for short range solute-solute interactions. Analysis of the broad high energy boric acid peak with calculations simulating multiple solute molecules could reveal clues to polyborate ion formation and would constitute an interesting future project.

Figure 3 compares the TEY NEXAFS spectra of hydrated boric acid with mineral boric acid, sassolite[21] (data provided by M. Fleet). The low energy peak at 194 eV is nearly identical in the two samples. Clearly, water does not significantly affect the 2p<sub>z</sub> unoccupied orbital. The acid-base transition from three coordinate (boric acid) to four coordinate (borate) boron requires water to hybridize with this 2p<sub>z</sub> orbital. Consequently, it would be expected that solvation should include water interacting with the B 2p<sub>z</sub> orbital. Water interacting with this nonbonding orbital would shift it in energy relative to the same orbital in the solid. No such shift in energy is observed for the low energy feature in hydrated vs. solid boric acid.

Furthermore, the trigonal boron peak at 194 eV does not show any shifts (within the experimental resolution) associated with pH/incorporation into polyborate ions. Not only is the unoccupied 2p<sub>z</sub> orbital unaffected by solvating water, it is also insensitive to changes in the extended bonding environment. The energy of the transition to the 2p<sub>z</sub> orbital does not change based on whether the trigonal boron is monomeric or part of a polyborate ion. The results are similar for the high energy feature (204 eV). The calculations reveal minor changes in the shape of this high energy trigonal boron feature (204 eV) between monomer and polyborate borons, but if present, these subtle changes cannot currently be determined experimentally. Moreover, spectra calculated by summing only the appropriate spectral contribution from monomers (as apposed to monomers and polyborate ions) are nearly identical to the calculated spectra in Figure 2. Clearly, extended bonding environment, i.e. monomer vs. polyborate ion, makes no observable spectral influence for solvated boron-oxide molecules.

Figure 3 also shows that the solid boric acid sample has a much narrower higher energy feature (204 eV) compared to that of solvated boric acid. Again, solute-solute interactions in the liquid may be responsible for the broad high energy feature in the experimental boric acid spectrum. Interestingly, the spectrum of the solid sample is very similar to the spectrum calculated for solvated boric acid.

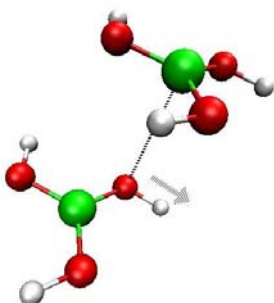
Based on the general environmental insensitivity evident in the solvated boron-oxides, it is not surprising that borate spectra exhibit no cation-dependent changes. Figure 4 shows NEXAFS spectra for sodium borate and potassium borate solutions. Within the noise of the measurement, there is no discernable difference between the two spectra. Increasing the concentration of sodium cations in solution similarly had no effect on the spectrum. The MD simulations of sodium borate indicated that sodium nearly always remains in contact with the borate. The median Na-boron distance from

the simulations was 2.6 Å and no sodium was found farther than 3.3 Å away from the boron. In spite of such a close Na-borate association, calculations also confirm that sodium has no spectral influence. Figure 5 shows the calculated borate spectrum compared to a similar spectrum calculated from simulations run without sodium. Within the error of the calculations, they are identical. Going one step further, Figure 5 also shows calculated spectra for boric acid and borate with all the water molecules removed. Again, within the error of the calculations, water induces no significant spectral changes to the boron-oxide spectra.

Water seems to have no spectral impact on these boron-oxides because they are not strongly hydrated. The presence of hydroxide moieties on boric acid and borate would lead one to believe that these oxides would strongly hydrogen bond with the surrounding water; however, this is not evident in the molecular dynamics simulations. Figure 6 displays various radial distribution functions (RDF) for boric acid, borate, and sodium-borate calculated from the simulations. The radial distribution functions give evidence that there are only weak hydrogen bonds between the oxides and water. For boric acid, the lone pairs on the oxygens donate to the empty  $2p_z$  orbital on the boron, making the lowest energy conformation trigonal planar. Consequently, there are fewer waters that donate a hydrogen bond to the boric acid oxygens. Similarly, the trigonal conformation allows the boric acid hydrogens to partially donate to neighboring oxygens. This limits the number hydrogen bonds that boric acid donates. The data are similar for the borate ion; however, in this case the lack of strong hydrogen bonds is due to cation association rather than confirmation. The conformational freedom of the borate-hydrogens, in conjunction with their ability to associate with borate-oxygens, leads to a relatively broad H to O-water peak that does not change much when the cation is absent. For borate, the O to H-water RDF has a sharp peak, indicative of a narrow range of hydrogen bond structures donated to the borate. Sodium interacts with the borate-oxygens and disrupts these donor hydrogen bonds. The broad peak and lack of peak, respectively, in the B to O-water and O to O-water RDFs confirm that sodium borate does not form strong hydrogen bonds with water. The dip in the B to O-water RDF for sodium borate is due to effects from the cation.

To further investigate the reasons for environmental insensitivity of boron-oxides, we inspect a few states contributing to the main XAS features. Figure 7 shows the calculated spectra and associated states (10% isosurface), both hydrated and bare, for an individual boric acid snapshot. The high energy feature ( $\sim 8$  eV on the unshifted/unstretched axis of Figure 7) comprises of transitions to a myriad of states, but only one is shown for clarity. As expected, the empty  $2p_z$  state (LUMO), is responsible for the sharp peak at 0 eV. This state is nearly identical in the hydrated and bare molecules (leftmost states in upper and lower portions of Figure 7). In spite of the fact that water must change this state to form the conjugate base, there is no evidence that this state interacts with water upon hydration. Also as expected, the higher energy feature (8 eV in Figure 7) is clearly  $\sigma^*$  in character. Even though there is some mixing with water states, for the most part these  $\sigma^*$  states are unaffected by hydration. Similar conclusions can be drawn by inspecting states from bare and hydrated borate ions. As evident by XAS spectra, molecular dynamics simulations, and electronic structure calculations, in general, boron oxides do not strongly interact with water.

A boric acid-borate dimer has already been proposed for the exchange between tetrahedral borate and trigonal boric acid.[9] Initial formation of the dimer may proceed through hydrophobic collapse of boric acid monomers followed by simple deprotonation. Scheme 1 shows a possible mechanism in which a boron from a boric acid coordinates with an oxygen from an adjacent boric acid. The over-coordinated oxygen is then more likely to donate a proton to the surrounding water. Similarly, polyborate ion formation likely proceeds via hydrophobic collapse of a third (and then fourth) boric acid monomer followed by elimination of water. Further information may be gained by measuring and comparing boric acid NEXAFS spectra taken at low and high concentrations. Low concentration data would presumably sample monomers and the spectra may be different from high concentration spectra. Simulations run with multiple solutes would also be very valuable for interpreting the experimental spectra.



Scheme 1

## Conclusions

Since water plays such an integral role in the acid-base and polyborate ion formation reactions of aqueous boron-oxides, it would be expected that these molecules be strongly hydrated. Moreover, the presence of hydroxide moieties on the boron compounds implies that there should be strong hydrogen bonds to water. However, the boron K-edge NEXAFS spectra of aqueous boric acid, borate, and various polyborate ions were measured as a function of pH, and in each case, the spectra and associated calculations gave little indication of strong hydrogen bonding to water. In addition, there is also no observable cation dependence on the spectra of aqueous borate ions, although the MD simulations indicated that sodium borate forms a contact ion pair in water. Our simulations revealed that boron-oxides do not structure the surrounding water molecules, indicating that boric acid and sodium borate (and polyborate ions by extension) are only weakly hydrated. Correspondingly, the states responsible for the observed NEXAFS features are mainly localized on the boron containing molecule. There is very little state mixing between the boron-oxide and the surrounding water.

## Figures

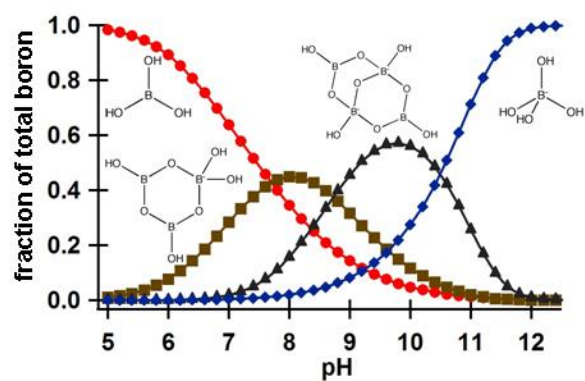


**Figure 1:** Boron-oxide speciation as a function of pH. Calculated for a 0.5 M boric acid solution, the plot shows the fraction of the total boron in each of the species (structure indicated on graph) as a function of pH. Circles – boric acid; squares – triborate; triangles – tetraborate; diamonds – borate.

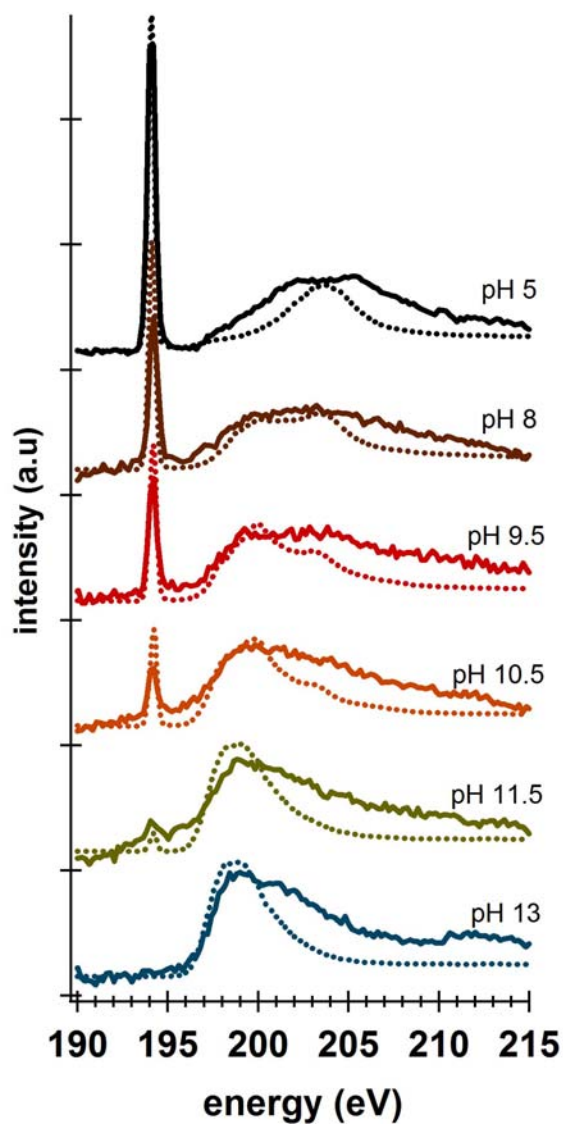


**Figure 2:** Experimental and theoretical B K-edge NEXAFS spectra showing the transition from trigonal to tetrahedrally coordinated boron with pH. The spectra are of 0.5 M boric acid solutions at a series of pH values, increasing pH top to bottom as indicated on figure. For each pH value the solid line is the experimental spectra and the dotted line is the associated spectra from calculations.

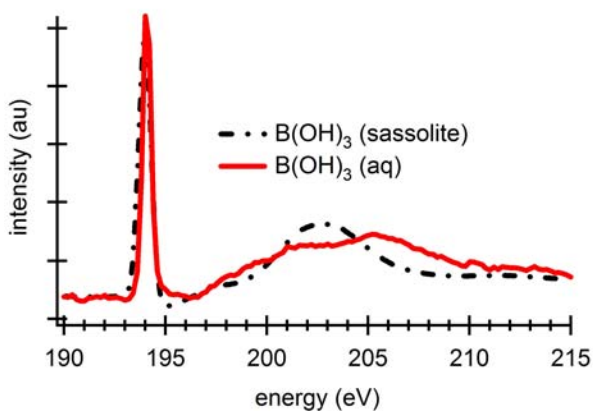


**Figure 3:** Boron K-edge NEXAFS spectra for aqueous (solid line) and solid (dashed line) boric acid. Solid boric acid, sassolite, data provided by M. Fleet: *Physics and Chemistry of Minerals* **2001**, 28, 421

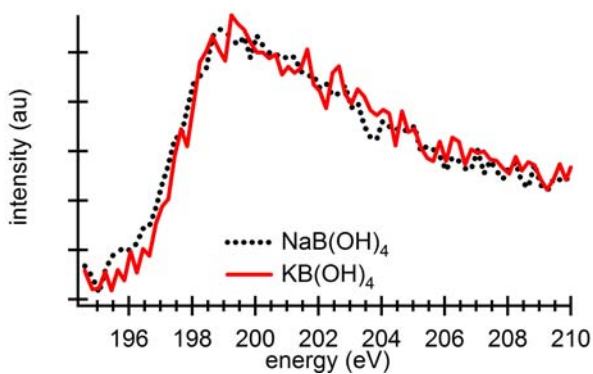


**Figure 4:** Boron K-edge NEXAFS spectra for sodium borate (dashed line) and potassium borate (solid line), with no cation dependence observable.

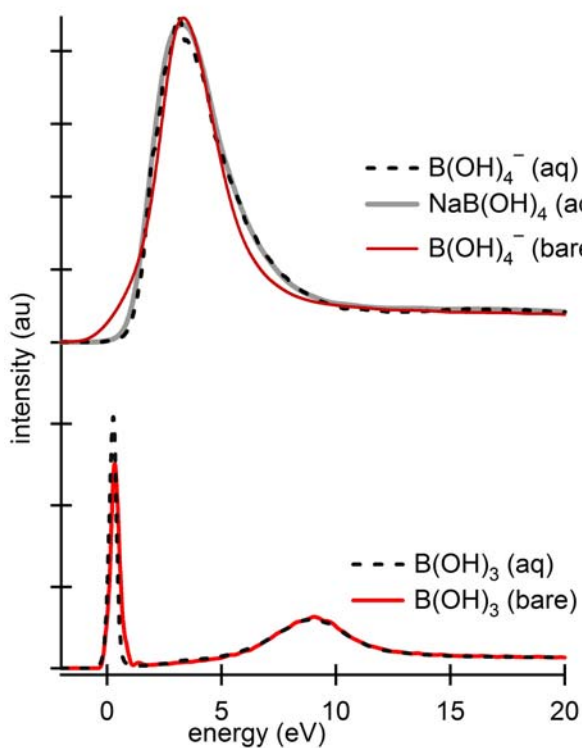


**Figure 5:** Calculations of borate NEXAFS spectra in the presence and absence of sodium cations and/or water. The upper section shows calculations for aqueous borate, aqueous sodium borate, and bare borate. There are no significant spectral changes between the three. Similarly, there are no significant spectral changes between aqueous boric acid and bare boric acid shown in the lower section.

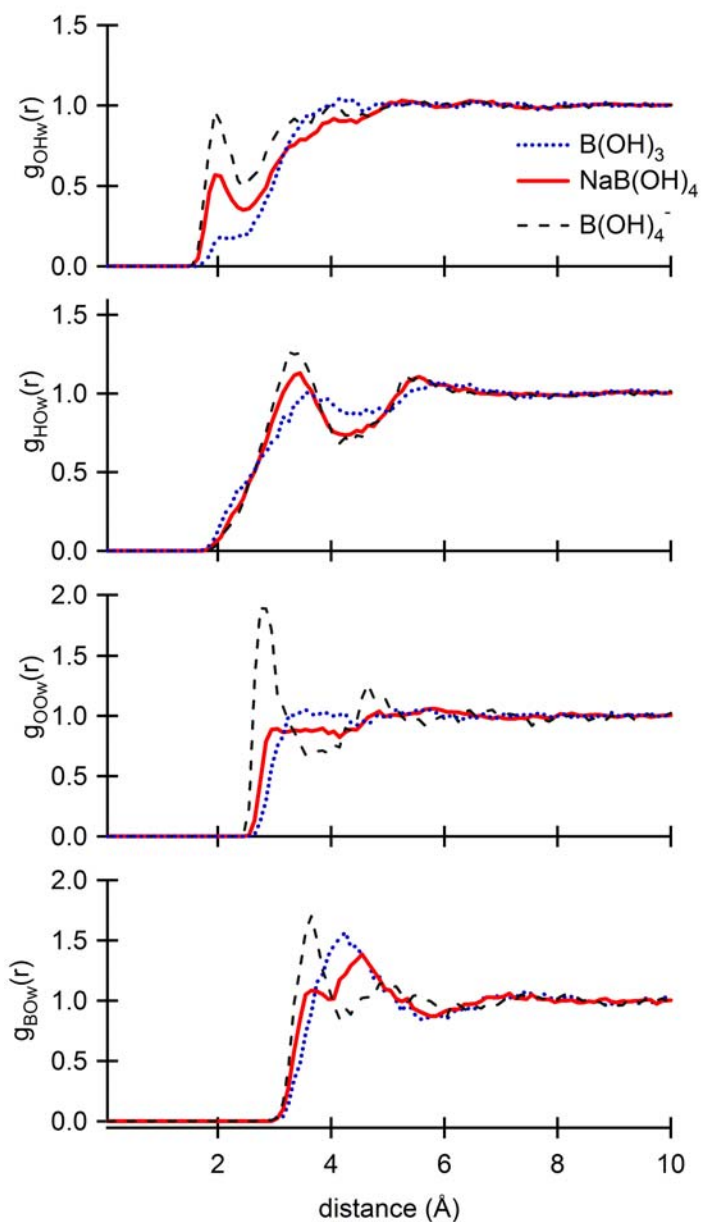


**Figure 6:** Radial distribution functions (RDF) calculated from MD simulations. From top to bottom: O to H-water, H to O-water, O to O-water, and B to O-water. In each plot the dotted blue line is boric acid, the solid red line is sodium borate, and the dashed black line is borate (without sodium). As evidenced by the change in peak height at 2 Å (top plot), the cation disrupts the donation of hydrogen bonds to the borate oxygens. For boric acid there are also few donor hydrogen bonds because the lone pairs on the oxygens contribute to the pi system in the trigonal planar molecule. H to O-water bonds (upper middle plot) are less affected by the cation, but the freely rotating H's on borate lead to greater variability in hydrogen bonds donated to water. Interactions between H's and O's within the molecule also diminish the oxides ability to donate a hydrogen bond to water. The disruption of hydrogen bonds by the cation is even more evident in the O to O-water RDF (lower middle). The B to O-water RDF (bottom) gives a relatively broad peak indicative of weak hydrogen bonding to water.



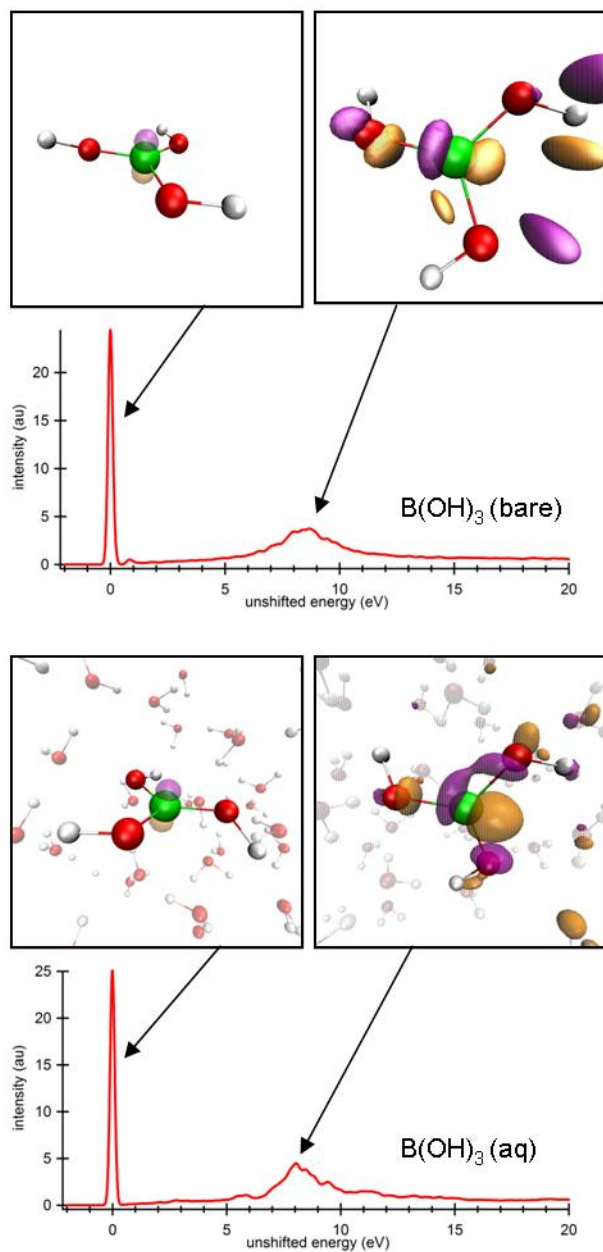


**Figure 7:** Single snapshot spectra and associated states (10% isosurface) for bare boric acid (upper) and fully hydrated boric acid (lower). The LUMO state, the empty 2pz orbital, responsible for the sharp low energy transition at 0 eV (energy adjusted to LUMO energy and unstretched) is nearly identical for the bare and hydrated cases. The LUMO states are the boxed images on the left. Water does not interact significantly with this empty 2pz orbital. The  $\sigma^*$  states to the right are some of the many responsible for the high energy feature ( $\sim 8$  eV). The local  $\sigma^*$  character is preserved upon hydration and there is minimal mixing with water.

## References

1. Demirci, U.B., et al., *Sodium Borohydride Hydrolysis as Hydrogen Generator: Issues, State of the Art and Applicability Upstream from a Fuel Cell*. Fuel Cells, 2010. **10**(3): p. 335-350.
2. *Go/No-Go Recommendation for Hydrolysis of Sodium Borohydride for On-Board Vehicular Hydrogen Storage* <http://www.hydrogen.energy.gov/pdfs/42220.pdf>. 2007.
3. Demirci, U.B., O. Akdim, and P. Miele, *Ten-year efforts and a no-go recommendation for sodium borohydride for on-board automotive hydrogen storage*. International Journal of Hydrogen Energy, 2009. **34**(6): p. 2638-2645.
4. Prendergast, D. and G. Galli, *X-ray absorption spectra of water from first principles calculations*. Physical Review Letters, 2006. **96**(21).
5. Salentine, C.G., *High-Field B-11 Nmr of Alkali Borates - Aqueous Polyborate Equilibria*. Inorganic Chemistry, 1983. **22**(26): p. 3920-3924.
6. Maya, L., *Identification of Polyborate and Fluoropolyborate Ions in Solution by Raman-Spectroscopy*. Inorganic Chemistry, 1976. **15**(9): p. 2179-2184.
7. Spessard, J.E., *Investigations of Borate Equilibria in Neutral Salt Solutions*. Journal of Inorganic & Nuclear Chemistry, 1970. **32**(8): p. 2607-&.
8. Ingri, N., *Equilibrium Studies of Polyanions .10. On First Equilibrium Steps in Acidification of B(OH)<sub>4</sub>, an Application of Self-Medium Method*. Acta Chemica Scandinavica, 1963. **17**(3): p. 573-&.
9. Ishihara, K., et al., *Kinetic-Study of Boric Acid-Borate Interchange in Aqueous-Solution by B-11 Nmr-Spectroscopy*. Inorganic Chemistry, 1994. **33**(17): p. 3811-3816.
10. Mesmer, R.E., C.F. Baes, and F.H. Sweeton, *Acidity Measurements at Elevated-Temperatures .6. Boric-Acid Equilibria*. Inorganic Chemistry, 1972. **11**(3): p. 537-&.
11. Hirao, T., et al., *Raman-Spectra of Polyborate Ions in Aqueous-Solution*. Journal of Inorganic & Nuclear Chemistry, 1979. **41**(8): p. 1217-1220.
12. Momii, R.K. and Nachtrieb, N.H., *Nuclear Magnetic Resonance Study of Borate-Polyborate Equilibria in Aqueous Solution*. Inorganic Chemistry, 1967. **6**(6): p. 1189-&.
13. Ingri, N., *Equilibrium Studies of Polyanions .11. Polyborates in 3.0 M Na(Br), 3.0 M Li(Br) and 3.0 M K(Br), a Comparison with Data Obtained in 3.0 M Na(ClO<sub>4</sub>)*. Acta Chemica Scandinavica, 1963. **17**(3): p. 581-&.
14. Reardon, E.J., *Dissociation-Constants for Alkali Earth and Sodium Borate Ion-Pairs from 10 to 50 Degrees C*. Chemical Geology, 1976. **18**(4): p. 309-325.
15. Corti, H., R. Crovetto, and R. Fernandezprini, *Mobilities and Ion-Pairing in LiB(OH)<sub>4</sub> and NaB(OH)<sub>4</sub> Aqueous-Solutions - a Conductivity Study*. Journal of Solution Chemistry, 1980. **9**(8): p. 617-625.
16. Rowe, L.M., L.B. Tran, and G. Atkinson, *The Effect of Pressure on the Dissociation of Boric-Acid and Sodium-Borate Ion-Pairs at 25-Degrees-C*. Journal of Solution Chemistry, 1989. **18**(7): p. 675-689.

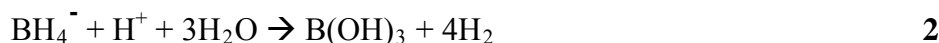
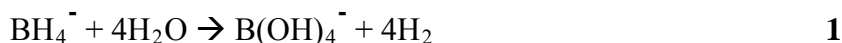
17. Pokrovski, G.S., J. Schott, and A.S. Sergeyev, *Experimental-Determination of the Stability-Constants of  $\text{NaSO}_4^-$  and  $\text{NaB}(\text{OH})_4(0)$  in Hydrothermal Solutions Using a New High-Temperature Sodium-Selective Glass-Electrode - Implications for Boron Isotopic Fractionation*. Chemical Geology, 1995. **124**(3-4): p. 253-265.
18. Sanyal, A., et al., *Evidence for a Higher Ph in the Glacial Ocean from Boron Isotopes in Foraminifera*. Nature, 1995. **373**(6511): p. 234-236.
19. Hemming, N.G. and G.N. Hanson, *Boron Isotopic Composition and Concentration in Modern Marine Carbonates*. Geochimica Et Cosmochimica Acta, 1992. **56**(1): p. 537-543.
20. Pagani, M., et al., *A critical evaluation of the boron isotope-pH proxy: The accuracy of ancient ocean pH estimates*. Geochimica Et Cosmochimica Acta, 2005. **69**(4): p. 953-961.
21. Fleet, M.E. and X. Liu, *Boron K-edge XANES of boron oxides: tetrahedral B-O distances and near-surface alteration*. Physics and Chemistry of Minerals, 2001. **28**(6): p. 421-427.
22. Carboni, R., et al., *Coordination of boron and phosphorous in Borophosphosilicate glasses*. Applied Physics Letters, 2003. **83**(21): p. 4312-4314.
23. Fleet, M.E. and S. Muthupari, *Boron K-edge XANES of borate and borosilicate minerals*. American Mineralogist, 2000. **85**(7-8): p. 1009-1021.
24. Fleet, M.E. and S. Muthupari, *Coordination of boron in alkali borosilicate glasses using XANES*. Journal of Non-Crystalline Solids, 1999. **255**(2-3): p. 233-241.
25. Kasrai, M., et al., *Surface modification study of borate materials from B K-edge X-ray absorption spectroscopy*. Physics and Chemistry of Minerals, 1998. **25**(4): p. 268-272.
26. Wilson, K.R., et al., *Investigation of volatile liquid surfaces by synchrotron x-ray spectroscopy of liquid microjets*. Review of Scientific Instruments, 2004. **75**(3): p. 725-736.
27. Uejio, J.S., et al., *Effects of vibrational motion on core-level spectra of prototype organic molecules*. Chemical Physics Letters, 2008. **467**(1-3): p. 195-199.
28. Schwartz, C.P., et al., *On the importance of nuclear quantum motions in near edge x-ray absorption fine structure spectroscopy of molecules*. Journal of Chemical Physics, 2009. **130**(18).
29. Otkidach, D.S. and I.V. Pletnev, *Conformational analysis of boron-containing compounds using Gillespie-Kepert version of molecular mechanics*. Journal of Molecular Structure-Theochem, 2001. **536**(1): p. 65-72.

## 3.2 Borohydride-Water Interactions Characterized by X-ray Absorption Spectroscopy

### Introduction

With large wt% hydrogen capacity, stable reactants, and benign reaction products, borohydride salts are exciting candidates for transportable hydrogen storage materials[1-5]. Sodium borohydride, in particular, has been closely examined, but despite its promise, has only yielded limited success[5-8]. One problem is the relatively poor solubility of the product oxides.[9] While solvation of these oxides is important for applications, and has been addressed in a companion study[9], it is the solvation and subsequent hydrolysis of the borohydride ion itself that leads directly to hydrogen production. Clearly, the details of hydration of sodium borohydride are vital for fully understanding and exploiting the hydrolysis reaction. Towards this end, we have investigated sodium borohydride with a combination of molecular dynamics simulations, near edge x-ray absorption fine structure spectroscopy (NEXAFS), and calculations of NEXAFS spectra generated with the excited electron and core hole method (XCH)[10].

In aqueous solution, borohydride reacts with water to yield molecular hydrogen (Reaction 1). This hydrolysis reaction is also catalyzed with acid to give boric acid  $[B(OH)_3]$  rather than borate  $[B(OH)_4^-]$  as the reaction product (Reaction 2). In both cases, based on kinetic and isotopic data, it is reasoned that the hydrolysis reaction proceeds via a 5-coordinate  $BH_5$  intermediate[11, 12]. Other experiments[13, 14] and calculations[15-17] have shown the feasibility of the  $BH_5$  intermediate, with analogies drawn to the more well-established  $CH_5^+$  carbocation. However, in condensed phases, the reaction intermediate is difficult to observe. More detailed information about borohydride hydration could yield more insight into the hydrolysis mechanism.



Relatively few studies have been performed on borohydride hydration and these have produced conflicting conclusions. Based on Raman spectra in various solvents, Shirk et al.[18] reasoned that there were no strong hydrogen bonds formed between borohydride and water. Strauss et al.[19] reached the opposite conclusion and suggested that the “solvation was tetrahedral... with the water protons pointing towards the faces of the  $BH_4^-$  tetrahedron.” More recently, borohydride hydration has been studied as part of a large group of molecules that form dihydrogen bonds[20-25]. These more recent studies that dealt specifically with borohydride confirmed the existence of a bond between a proton donor and a borohydride hydrogen, but they did not specifically examine borohydride in water[24, 25]. With regards to solvation, these experiments were interpreted as yielding “indirect evidence for [a] linear structure”[20], referring to solvation along the tetrahedral corners. Calculations on borohydrides evidenced a linear  $X-H \cdots H$  bond, but a bent  $H \cdots H-B$  bond[23, 24]. Crystal structure data from

$\text{NaBH}_4 \cdot 2\text{H}_2\text{O}$  also give evidence for water bonding to the hydride hydrogen, as opposed to a B-H sigma bond or to the boron itself[26].

XAS spectra of solid sodium borohydride have been studied previously; However, the spectrum was presented without assignment of the salient spectral features[27]. Boron-containing minerals and glasses have also been studied and the spectral features assigned[28-32]. Trigonally coordinated boron exhibits a sharp pre-edge feature around 194 eV, which is attributed to the transition of an electron from the B 1s core state to the unoccupied B  $2p_z$  orbital (oriented perpendicular to the trigonal plane). There is also a higher energy peak above the ionization potential (IP) that is attributed to transitions from B 1s to sigma antibonding ( $\sigma^*$ ) orbitals. Tetrahedrally coordinated boron has one main feature above the IP which is assigned to the transition of electrons from B 1s to sigma antibonding ( $\sigma^*$ ) states[30].

Here we investigate borohydride in basic solution using near edge x-ray absorption fine structure (NEXAFS) spectroscopy of liquid microjets[33]. The unoccupied molecular orbitals probed in NEXAFS experiments extend beyond the boron-containing molecule itself and, as a result, are sensitive to changes in local structure and environment, viz. aqueous solvation. We compare the experimental boron spectra with calculated spectra generated using the recently developed excited electron and core hole (XCH) method[10].

## Methods

### A. Samples

$\text{NaBH}_4$  from Aldrich (99% pure) was added to a 1 M NaOH solution to slow the hydrolysis reaction and evolution of hydrogen gas. The water was Millipore filtered and had a resistivity of 18 M $\Omega$ /cm.

### B. NEXAFS spectroscopy

The boron K-edge (180-220 eV) is in the soft x-ray region, accessible only in high vacuum environments. Volatile liquids, such as an aqueous borohydride solution, are typically incompatible with high vacuum; however, using liquid microjets, we are able to inject a thin liquid filament into vacuum. With this approach, and a few differential pumping sections, we are able to windowlessly couple the liquid jet chamber to Beamline 8.0.1 at the Advanced Light Source at Lawrence Berkeley National Laboratory. The soft x-rays from the undulator beamline are focused to a spot size of  $\sim 50$   $\mu\text{m}$  and a liquid jet nominally 30  $\mu\text{m}$  in diameter is positioned to intersect the x-ray beam. The cascade of electrons from the x-ray absorption process is collected on a biased copper electrode. Collected in this manner, the total electron yield is a bulk-sensitive measurement[34, 35].

Because the sample volume is continually renewing, contamination of the sample due to x-ray damage is minimized. In the present experiment, the liquid jet is created by using a Teledyne-ISCO syringe pump to pressurize solutions behind a nozzle made from a small section of fused silica capillary. Immediately after the x-rays interact with the liquid in vacuum, the liquid passes through skimmer and is cryotrapped onto a liquid nitrogen cooled surface. The cryotrapping, in conjunction with the use of turbomolecular pumps, keeps the pressure in the interaction chamber in the low  $10^{-4}$  torr range, and allows for the windowless coupling to the beamline.

X-ray absorption spectra are collected by scanning the x-ray energy from the beamline in 0.2 eV steps. The current collected at the biased electrode is first amplified and converted to a voltage with a picoammeter and then converted into a frequency before being read into a beamline computer. The spectra collected in this manner are normalized to the current from a gold mesh located ~3 meters upstream. The baseline was further corrected by subtracting a vapor spectrum taken off the liquid jet. Multiple spectra were collected, averaged, and area normalized for comparison. The calibration of the beamline monochromator was checked against a spectrum of solid boric acid. A more detailed description of the experimental endstation and data collection has been published elsewhere[33].

### C. Calculations.

Because core level excitations are fast compared to nuclear motion, the experimental spectra are an instantaneous average of all thermally populated vibrational degrees of freedom and solvent structure. Consequently, to accurately simulate the experimental spectra, it is necessary to account for solute configuration and the structure of the solvent[36, 37]. To this end, sodium borohydride was solvated in a periodic box with TIP3P water and a molecular dynamic simulation run at 300K (Langevin thermostat) for 10 ns. The borohydride was treated quantum mechanically with the MNDO Hamiltonian and the surrounding water was treated classically in a mixed quantum mechanics/molecular mechanics (QM/MM) simulation. The nonbonding (Lennard-Jones) parameters for boron were taken from Otkidach and Pletnev[38]. Molecular configurations were collected from 100 snapshots every 100 ps.

Using the atomic positions from a snapshot, we calculated an x-ray absorption spectrum. The spectra from all 100 snapshots were averaged to produce a theoretical x-ray absorption spectrum. The details concerning these x-ray absorption calculations have been published previously[10]. Briefly, the electronic structure of the system was calculated using density functional theory. The exchange-correlation energy was calculated with the Perdew-Burke-Ernzerhof exchange-correlation functional within the generalized-gradient approximation. A plane wave basis set with periodic boundary conditions was employed to best model both localized and delocalized states. To reduce to calculation cost, pseudopotentials were used to model all core electrons. To simulate the experimental excitation of a boron 1s electron to an unoccupied molecular orbital, the boron pseudopotential included a core hole (electronic configuration  $1s^1 2s^2 2p^2$ ) and an extra electron was included with the valence electrons. That is, these XCH calculations explicitly include a full core hole and an extra electron in the lowest energy valence state. Self consistent energies and states were calculated with PWscf on the Franklin supercomputer at NERSC. Transition amplitudes for the calculated spectra were calculated within the single particle and dipole approximations.

The calculated spectra were all uniformly broadened with Gaussians of 0.2 eV full width at half maximum. To help correct for known bandgap underestimation in DFT, the energy axis for all calculated spectra was stretched by 10%. Since only relative energies are obtained, the calculations were empirically aligned to experiment.

## Results and Discussion

Figure 1 shows experimental NEXAFS spectra of solvated sodium borohydride, solvated boric acid, and solid sodium borohydride. The spectra for the aqueous systems are overlaid on top of those of solid sodium borohydride from Hallmeier et al.[27]. The solvated borohydride sample exhibits a relatively sharp peak at 191 eV and a broader second feature at 198 eV. Because sodium borohydride is hygroscopic and reacts with water, contamination from boric acid is evident in the spectra from the solid sample. The uppermost data in Figure 1 were collected after intentional atmospheric water contamination and show a clear increase in the boric acid peak at 194 eV. Spectra and analysis for solvated boric acid as well as solvated sodium borate [ $\text{NaB}(\text{OH})_4(\text{aq})$ ] have been published previously[9]. One pertinent conclusion from that study was that the boric acid pre-edge peak at 194 eV showed no shifts in energy between the solid and solvated samples[9]. Because the solid and solvated boric acid peaks align, it is easy to see the shift to lower energy and narrowing of the borohydride peak at 191 eV that result directly from water solvation.

The spectrum of the solvated boric acid is replotted in Figure 2 along with spectra produced from the theoretical calculations. The calculated borohydride spectrum matches well with experiment at the 191 eV feature, but misses the higher energy peak. Although the hydrolysis reaction should be negligibly slow in 1 M NaOH[13], borohydride reacts with water to form borate; so, it is possible that the peak around 198 eV is due to borate contamination. However, the borate spectrum does not cleanly subtract from the borohydride spectrum. In addition, the X-ray absorption spectra of solid sodium borohydride from Hallmeier et al.[27] show a second high energy peak around 200 eV. The nature of the second peak in the borohydride spectrum remains uncertain.

The relatively sharp peak at 191 eV in the solvated borohydride spectrum is uncharacteristic of tetrahedral boron molecules. For example,  $\text{NaB}(\text{OH})_4$ [9, 29, 30],  $\text{KBF}_4$ , and  $\text{NH}_4\text{BH}_4$ [27, 39] all have more typical tetrahedral boron K-edge NEXAFS spectra with a sharp rise at the absorption onset and a more gradual decline in the post-absorption edge. The peak at 191 eV in the borohydride spectrum resembles a much narrower and more symmetric transition to a p state, similar to the boric acid peak at 194 eV. Clearly, water drastically alters the electronic structure of borohydride.

To illustrate the spectral effects of hydration, Figure 2 also presents a calculated NEXAFS spectrum from bare borohydride anions. The bare ion calculations were performed from the same snapshots as the fully hydrated system, but with all the water molecules (and sodium atoms) removed. In this way, comparing the bare borate spectrum with the fully hydrated spectrum reveals the spectral effects of the surrounding water molecules. The shifting to lower energy and narrowing of the peak at 191 eV are reproduced in the bare vs hydrated calculations, confirming that water is directly responsible for these effects.

To further investigate borohydride hydration, spectra were calculated from small clusters. Figure 3 shows spectra from a minimized  $\text{BH}_4^- \cdot 5\text{H}_2\text{O}$  cluster evolving down to a  $\text{BH}_4^- \cdot \text{H}_2\text{O}$  cluster by successively removing water. The same shift in peak energy and width observed in the fully hydrated and bare calculations are observed in a stepwise fashion in the clusters. The five-water cluster has a peak that is red-shifted and much narrower compared to the one-water cluster. The shifting of the peak in Figure 3 is

explained by the creation of dihydrogen bonds. The borohydride hydrogens carry a partial negative charge and interact favorably with the partial positive charges on the hydrogens of water. As electron density is transferred to the new H-H bond, the B-H bond is weakened. Consequently, the overlap between the borohydride hydrogen and boron is lessened and the antibonding orbitals shifts to lower energy. With each additional solvating water, antibonding states are created at lower energy and the absorption feature shifts to lower energy.

The fact that the 191 eV borohydride peak narrows with the addition of water is more unexpected. Schwarz et al.[39] point out that when a tetrahedral system is distorted, some of the spherical states can and adopt p character. Transitions from the B 1s state to water-dependent p states may account for the relatively sharp transition near the absorption edge. The sharp feature could also be due to confinement of the wavefunction near the boron atom. States above the LUMO can have local p character, but transitions to these states remain weak due to poor spatial overlap. The lower portion of Figure 4 shows the LUMO+2 state from one molecular dynamics snapshot with the waters removed. While there is local p character around the boron, the orbital is highly diffuse. As a result, overlap between the core level and this expansive state is small and there is no sharp feature associated with this transition. In contrast, the upper part of Figure 4 shows some of the states responsible for the sharp spectral feature in the solvated borohydride spectrum. With water present, the local p character remains intact, but the wavefunction is more localized around the boron and a few of the surrounding waters. The arrows in the figure indicate the energy where the visualized states contribute to the spectrum. When surrounded by water, spatial overlap between the core state and the spatially confined excited states is increased and, consequently, a relatively intense and narrow peak appears.

To illustrate the structure of water surrounding borohydride, Figure 5 shows randomly chosen snapshots from the MD calculations, from which it is clear that borohydride is mainly hydrated along the tetrahedral corners and edges. On average, borohydride is tightly bound to 2.42 waters with a  $H_{BH4}-H_{wat}$  bond of less than 2.1 Å; 43% of the water protons within 2.1 Å were also closely associated (<2.4 Å) with a second borohydride hydrogen, i.e. edge hydration. Only 6% of the bonded protons were within 2.4 Å of three borohydride hydrogens. That is, very few waters are bound to borohydride at the tetrahedral faces. That borohydride is predominantly hydrated along the tetrahedral corners and edge is consistent with previous conclusions that the O-H...H angle would be fairly linear, while the B-H...H angle is bent[23, 40]. This leads to a configuration “convenient for the interaction with stronger proton donors in which the hydride molecule is susceptible to proton transfer and side-on dihydrogen ligand formation.”[23] In other words, hydration along the tetrahedral edges is consistent with the formation of a 5-coordinate hydrolysis transition state.

Radial distribution functions (RDFs) calculated from the molecular dynamics simulations of sodium borohydride system are shown in Figure 6. Given that the average B-H bond length in borohydride is just less than 1.2 Å, the peaks in the B- $H_{wat}$  and B- $O_{wat}$  RDFs clearly indicate that water is closely bound to and structured around the borohydride. The molecular dynamics simulation also reveals that sodium ions are in contact with the borohydride. This observation is consistent with previous hydration studies[18, 19] and calculations done on borohydride in methanol[41]. Regardless of



close association with borohydride ions, the presence of sodium is spectroscopically inconsequential. Molecular dynamics simulations and x-ray absorption spectra from the resulting snapshots were also calculated for solvated borohydride in the absence of  $\text{Na}^+$ . Figure 7 shows the hydrated borohydride spectrum in the presence and absence of  $\text{Na}^+$ . Consistent with the analysis above, there is a slight red shift in the no-sodium case due to the fact that more water can surround the borohydride. In spite of this shift, within the error of the calculations, the two spectra are identical. Sodium's effect seems confined to the occlusion of water around the borohydride.

There is evidence from the simulations that borohydride is solvated along the tetrahedral corners (although skewed from complete linearity), tending toward the tetrahedral edges. Unfortunately, the nature of the second peak (198 eV) in the experimental spectrum remains unclear. Figure 8 shows three idealized clusters used to compare hydration around borohydride. Static DFT calculations on these clusters give the energy of the face centered water-borohydride cluster at 1.5 eV above the energy of both the corner and edge hydration. This energy difference for these three clusters is consistent with the results obtained from the molecular dynamics simulations. However, Figure 8 also shows the spectra associated with each idealized cluster. It is interesting that the tetrahedral corner cluster (and to a lesser extent the tetrahedral face cluster) exhibit a higher energy feature  $\sim 7$  eV above the main feature, as observed in the experiments. It is possible that these configurations are under-sampled in the QM/MM simulations.

Unfortunately, only one of the 100 full system snapshots exhibited an intense high energy feature. This snapshot had a water along a borohydride face as well as water closely associated with the opposite corner. Moreover, in the simulations done in the absence of  $\text{Na}^+$ , there was a greater number of snapshots exhibiting high energy peaks; although this feature still did not show up in the average. Again, these snapshots had water along a tetrahedral face and on the opposite corner. Because sodium excludes water from around the borohydride, combination face and opposite corner hydration is more likely in the absence of sodium ions. It is also possible that this geometry of hydration leads most directly to the hydrolysis transition state. Interestingly, lithium borohydride is not stabilized in basic solution[18], likely because lithium is more strongly solvated by water. Not only would  $\text{Li}^+$  be less likely to form a contact pair with borohydride, but also the water around  $\text{Li}^+$  is more easily hydrolyzed. The protons from this hydrolysis would catalyze borohydride's reaction with water. Clearly, the cation influences the formation of the hydrolysis transition state.

While the QM/MM calculations sampled thermally accessible borohydride vibrations, there remained a boundary between the quantum mechanical borohydride and the classical water. Calculations that allow for explicit interaction of the water and borohydride may be necessary to properly identify all the features in aqueous sodium-borohydride NEXAFS spectrum. First principles molecular dynamics calculations constitute an interesting future project in this area.

## Conclusions

The boron K-edge NEXAFS spectra of aqueous sodium-borohydride was measured. The borohydride spectra exhibited a sharp peak near the absorption edge (191 eV) that is a direct result of hydration, and this peak is red-shifted compared to solid

sodium-borohydride. This red-shift is direct evidence for strong dihydrogen bonding between a proton from water and a borohydride hydrogen. As a result of this dihydrogen bond formation, the B-H bond in borohydride is weakened and the antibonding states move to lower energy. Concomitantly, the absorption feature moves to lower energy. The narrow peak at 191 eV is also due to interactions with water. States above the LUMO have p character, but transitions to these orbitals are relatively weak due to poor spatial overlap. Water surrounding borohydride tends to confine these excited state orbitals such that the overlap between the B 1s the excited state is increased. In other words, water increases the local p character of the excited states around the boron atom. Consequently, the solvated borohydride NEXAFS spectra has an absorption onset peak that is uncharacteristically sharp for a tetrahedral molecule. QM/MM calculations favor borohydride hydration along the tetrahedral corners and edges, but there is a high energy peak in the spectrum (198 eV) that is unaccounted for in the calculations. The assignment of this high energy feature may be key to gaining further insight into the hydrolysis reaction mechanism. Calculations on borohydride solid and first principles molecular dynamics on solvated borohydride may give insight into the nature of the high energy NEXAFS feature.

## Figures

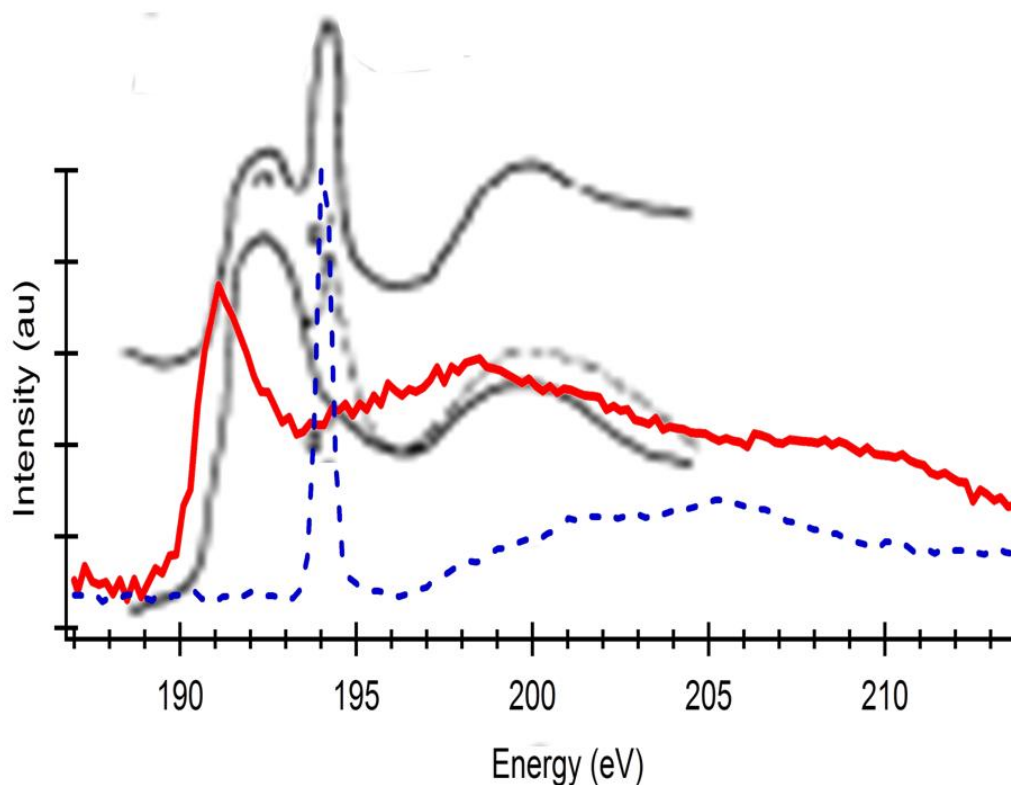


**Figure 1:** Boron K-edge NEXAFS spectrum of aqueous (0.5 M)  $\text{NaBH}_4$  (solid red line) and aqueous  $\text{B(OH)}_3$  (dashed blue line). The spectra in the background (gray lines) from Hallmeier et al[27] are of solid  $\text{NaBH}_4$ . Solid  $\text{NaBH}_4$  reacts with ambient water vapor to produce  $\text{B(OH)}_3$  and a sharp peak at 194 eV. The uppermost spectrum was taken after intentional water contamination. The  $\text{B(OH)}_3$  peaks serve as a standard and highlight the shift in energy of the  $\text{NaBH}_4$  peaks upon solvation. The low energy  $\text{NaBH}_4$  peak (191 eV) also appears to be much narrower than in the solid and is uncharacteristic of a tetrahedral molecule.

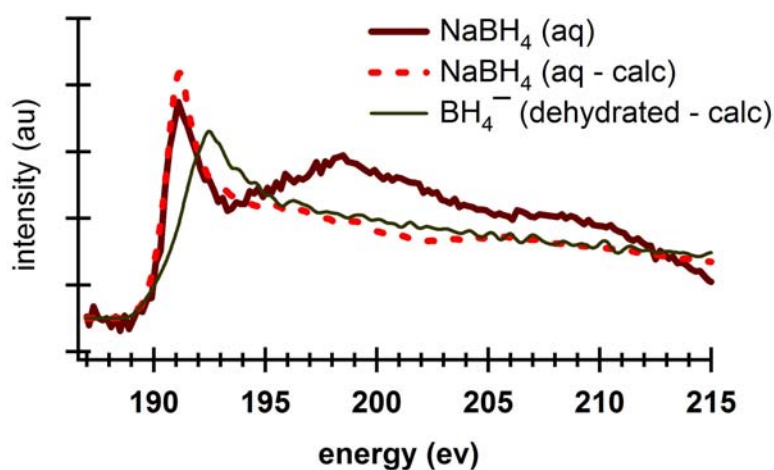


**Figure 2:** Aqueous  $\text{NaBH}_4$  NEXAFS spectrum (thick line) compared with theoretical calculations (dashed line) of the same system. The calculations are in excellent agreement with experiment at the low energy peak (191 eV) but fail to reproduce the high energy feature (198 eV). Calculated spectra for bare  $\text{BH}_4^-$  (thin line) are inconsistent with experiment and the main feature is much broader than for the liquid.

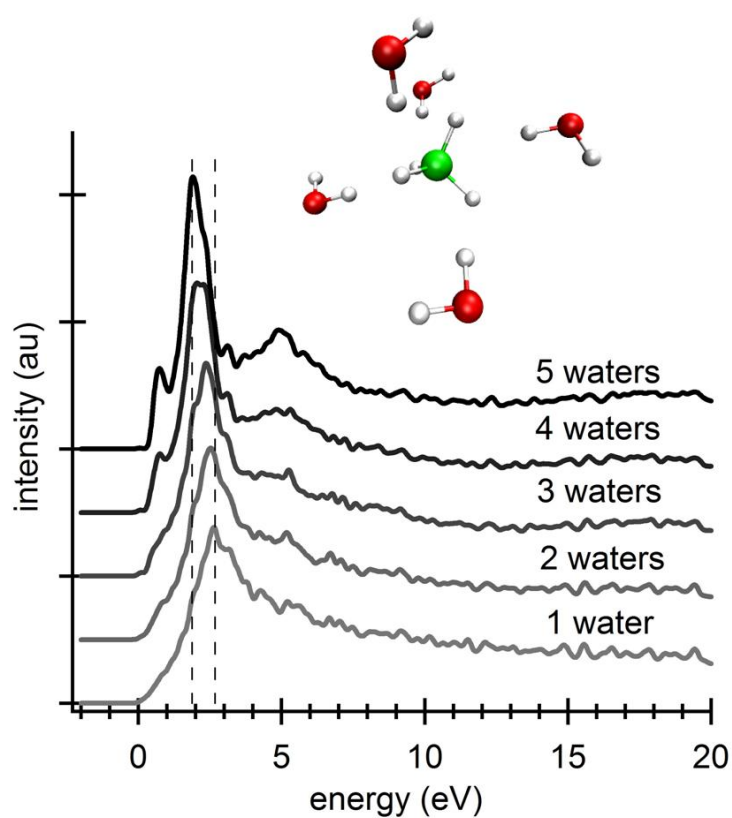


**Figure 3:** Depiction of a  $\text{BH}_4^- \cdot 5\text{H}_2\text{O}$  cluster and corresponding calculated spectrum. The spectra moving down were calculated after successive removal of water from the 5-water cluster. The main absorption feature moves to higher energy and broadens upon removal of water. Dihydrogen bonds between the water and borohydride are responsible for the shift in energy.

**Figure 4:**

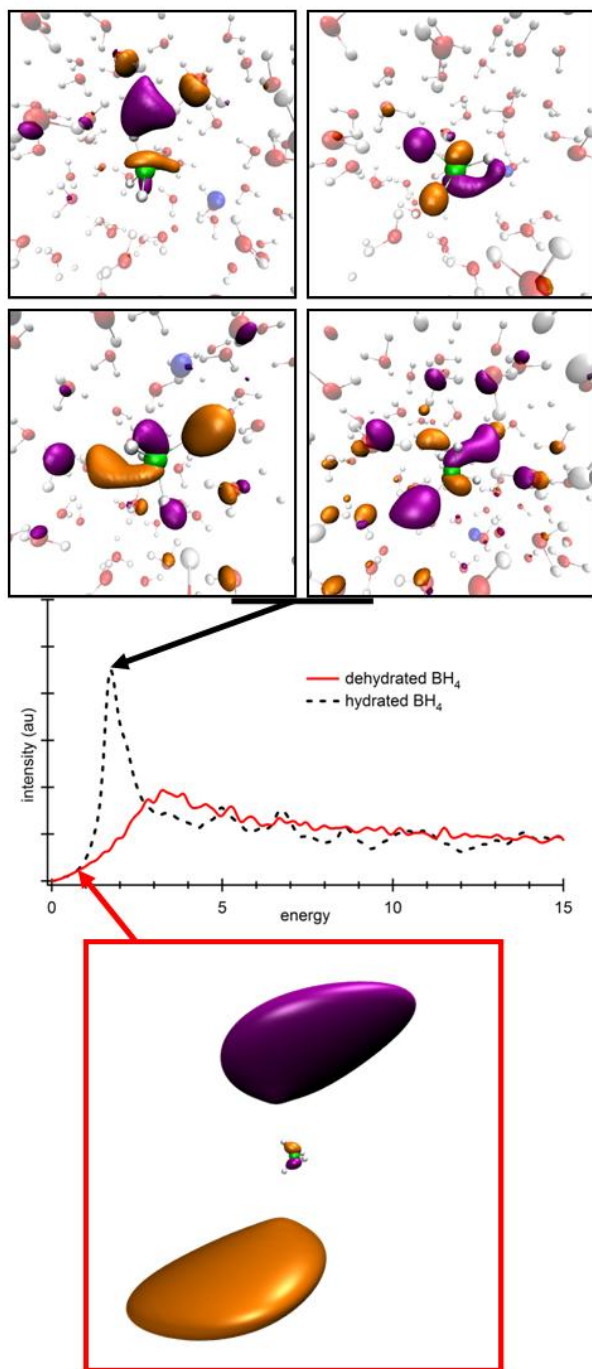


**Figure 4:** Spectra and states from a single molecular dynamics snapshot of aqueous NaBH<sub>4</sub> (dashed line and top) and bare BH<sub>4</sub><sup>-</sup> (solid line and bottom). In both cases the states show p character around the boron, but the diffuse nature of the bare ion orbital makes transitions to this state relatively weak. The arrow indicates the energy of the state in the calculated spectrum. With water present, these excited state orbitals are confined near the boron atom and the spatial overlap with the core state is increased. Consequently, the spectrum shows a sharper peak in water.

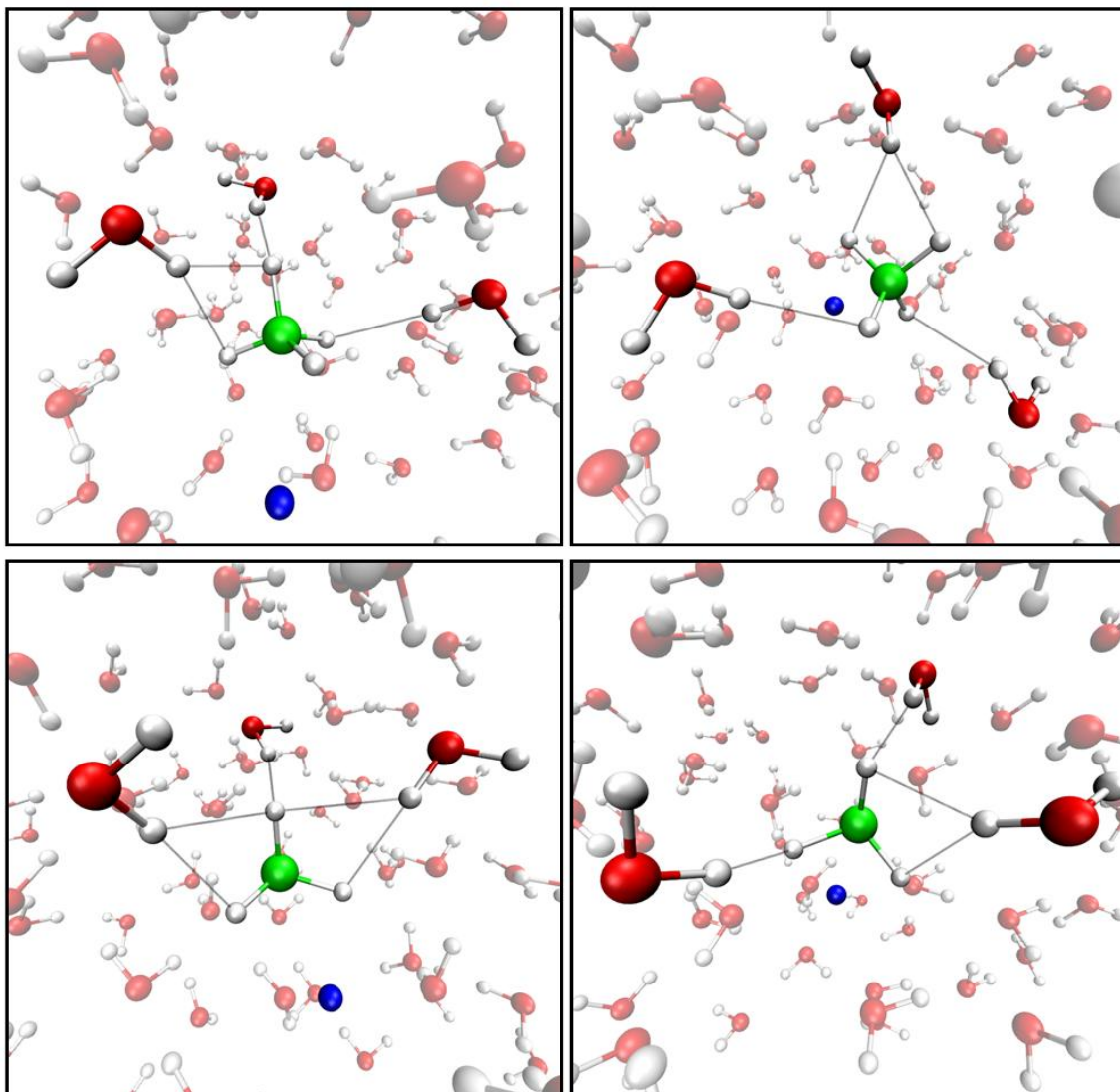


**Figure 5:** MD snapshots from the QMMM simulation of the sodium borohydride system. The snapshots are dominated by hydration along the borohydride tetrahedral corners and edges. Hydration along tetrahedral faces is less common. Green: boron, red: oxygen, white: hydrogen, and blue: sodium.

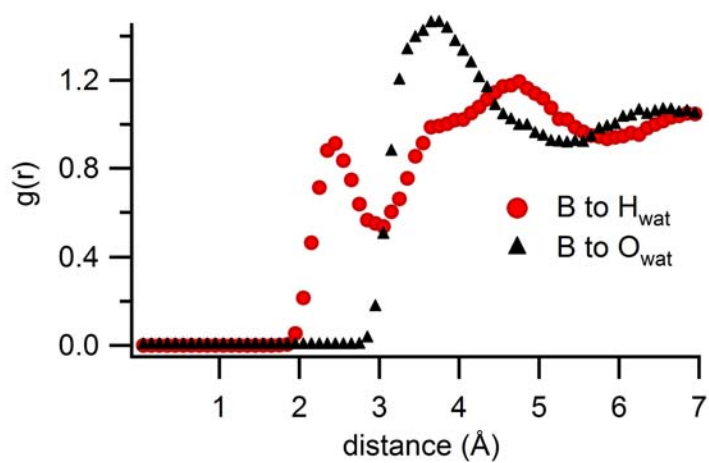


**Figure 6:** Boron to water-oxygen and boron to water-hydrogen radial distribution functions. The peaks in the distribution functions show clear structuring of the first solvation shell around borohydride and are evidence for strong  $\text{BH}_4$ -water interactions.



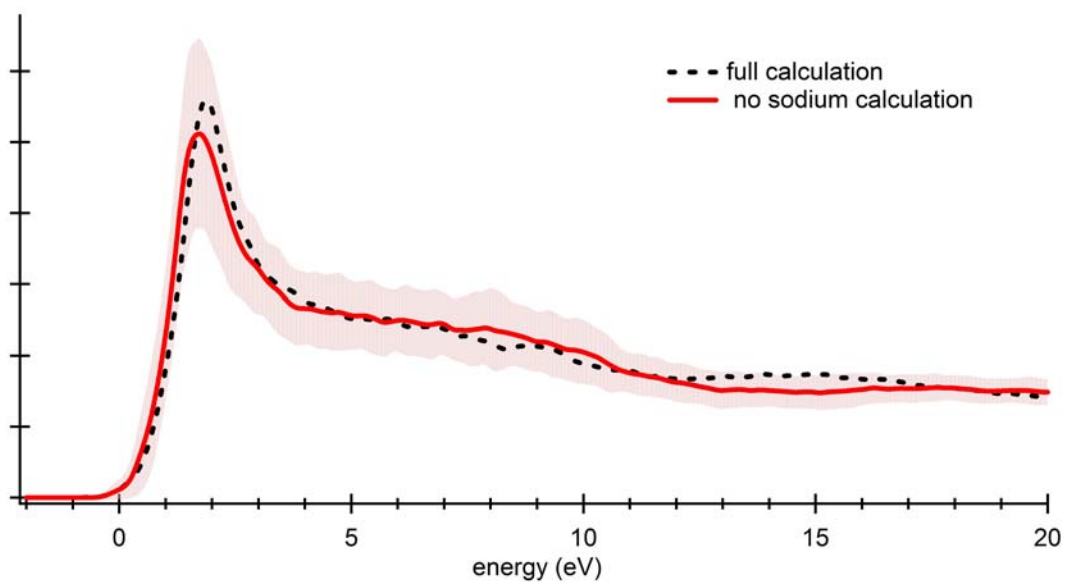


**Figure 7:** Calculated spectra from the full  $\text{NaBH}_4 \cdot 118\text{H}_2\text{O}$  system (dashed line) and a  $\text{BH}_4^- \cdot 118\text{H}_2\text{O}$  system (solid line). Without  $\text{Na}^+$ , the spectrum has a slight shift to lower energy, however the two are equal within the error of the calculations (shaded area). The  $\text{Na}^+$  forms a contact ion pair with the  $\text{BH}_4^-$  and excludes water from around the borohydride. Consequently, the red shift is consistent with the observation that water shifts the spectrum to lower energy.

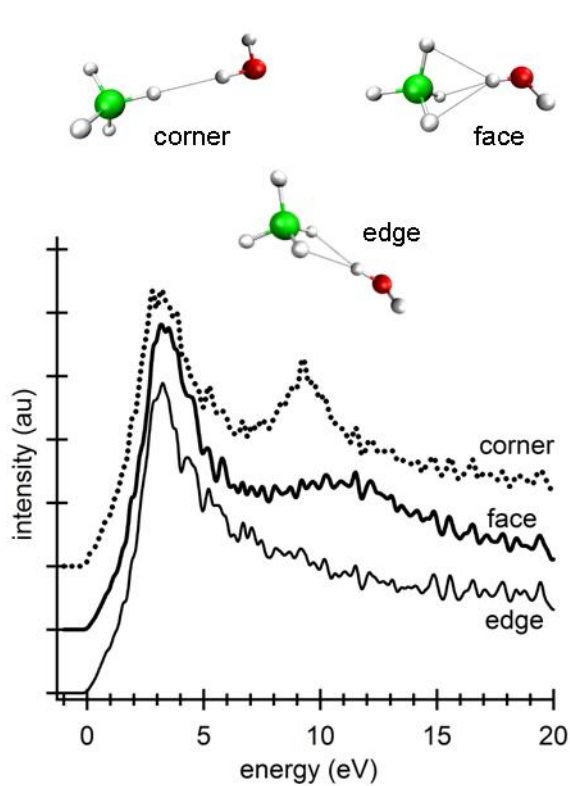


**Figure 8:** Idealized one water-borohydride clusters and associated NEXAFS spectra with the water in contact with a borohydride tetrahedral corner (dotted line), edge (thin line), and face (bold line). The tetrahedral corner and face hydration give a peak at higher energy that is observed in experiment, but not reproduced by calculations

## References

1. Amendola, S.C., et al., *An ultrasafe hydrogen generator: aqueous, alkaline borohydride solutions and Ru catalyst*. Journal of Power Sources, 2000. **85**(2): p. 186-189.
2. Kim, J.H., et al., *Reversible hydrogen storage in calcium borohydride  $\text{Ca}(\text{BH}_4)_2$* . Scripta Materialia, 2008. **58**(6): p. 481-483.
3. Severa, G., E. Ronnebro, and C.M. Jensen, *Direct hydrogenation of magnesium boride to magnesium borohydride: demonstration of > 11 weight percent reversible hydrogen storage*. Chemical Communications, 2010. **46**(3): p. 421-423.
4. Demirci, U.B. and P. Miele, *Sodium tetrahydroborate as energy/hydrogen carrier, its history*. Comptes Rendus Chimie, 2009. **12**(9): p. 943-950.
5. Liu, B.H. and Z.P. Li, *A review: Hydrogen generation from borohydride hydrolysis reaction*. Journal of Power Sources, 2009. **187**(2): p. 527-534.
6. *Go/No-Go Recommendation for Hydrolysis of Sodium Borohydride for On-Board Vehicular Hydrogen Storage* <http://www.hydrogen.energy.gov/pdfs/42220.pdf>. 2007.
7. Demirci, U.B., et al., *Sodium Borohydride Hydrolysis as Hydrogen Generator: Issues, State of the Art and Applicability Upstream from a Fuel Cell*. Fuel Cells, 2010. **10**(3): p. 335-350.
8. Demirci, U.B., O. Akdim, and P. Miele, *Ten-year efforts and a no-go recommendation for sodium borohydride for on-board automotive hydrogen storage*. International Journal of Hydrogen Energy, 2009. **34**(6): p. 2638-2645.
9. Duffin, A.M., et al., *X-ray Absorption Spectroscopy of Aqueous Boron-Oxides*. (In preparation).
10. Prendergast, D. and G. Galli, *X-ray absorption spectra of water from first principles calculations*. Physical Review Letters, 2006. **96**(21).
11. Mesmer, R.E. and W.L. Jolly, *Hydrolysis of Aqueous Hydroborate*. Inorganic Chemistry, 1962. **1**(3): p. 608-&.
12. Pecsok, R.L., *Polarographic Studies on the Oxidation and Hydrolysis of Sodium Borohydride I*. Journal of the American Chemical Society, 1953. **75**(12): p. 2862-2864.
13. Kreevoy, M.M. and J.E. Hutchins,  *$\text{H}_2\text{bh}_3$  as an Intermediate in Tetrahydridoborate Hydrolysis*. Journal of the American Chemical Society, 1972. **94**(18): p. 6371-&.
14. Tague, T.J. and L. Andrews, *Reactions of Pulsed-Laser Evaporated Boron Atoms with Hydrogen - Infrared-Spectra of Boron Hydride Intermediate Species in Solid Argon*. Journal of the American Chemical Society, 1994. **116**(11): p. 4970-4976.
15. Filippov, O.A., et al., *Proton-transfer and H-2-elimination reactions of main-group hydrides  $\text{EH}_4^-$  ( $\text{E} = \text{B}, \text{Al}, \text{Ga}$ ) with alcohols*. Inorganic Chemistry, 2006. **45**(7): p. 3086-3096.
16. Kim, Y., J. Kim, and K.H. Kim, *Theoretical study for the potential energy surface of  $\text{BH}_5$  using the multicoefficient correlated quantum mechanical methods*. Journal of Physical Chemistry A, 2003. **107**(2): p. 301-305.

17. Schuurman, M.S., et al., *The highly anharmonic BH5 potential energy surface characterized in the ab initio limit*. Journal of Chemical Physics, 2005. **122**(10).
18. Shirk, A.E. and D.F. Shriver, *Solvent and Cation Dependence of Tetrahydroborate, Bh4-, Raman-Spectrum*. Journal of the American Chemical Society, 1973. **95**(18): p. 5901-5904.
19. Strauss, I.M., M.C.R. Symons, and V.K. Thompson, *Solvation Spectra - .53. Ir and Nuclear Magnetic-Resonance Studies of Tetrahydroborate Anion in Various Pure Solvents and Binary Aqueous Mixtures*. Journal of the Chemical Society-Faraday Transactions I, 1977. **73**: p. 1253-1259.
20. Belkova, N.V., E.S. Shubina, and L.M. Epstein, *Diverse world of unconventional hydrogen bonds*. Accounts of Chemical Research, 2005. **38**(8): p. 624-631.
21. Custelcean, R. and J.E. Jackson, *Dihydrogen bonding: Structures, energetics, and dynamics*. Chemical Reviews, 2001. **101**(7): p. 1963-1980.
22. Filippov, O.A., et al., *Intermolecular HH vibrations of dihydrogen bonded complexes H3EH-center dot center dot center dot HOR in the low-frequency region: Theory and IR spectra*. Journal of Physical Chemistry A, 2008. **112**(35): p. 8198-8204.
23. Epstein, L.M. and E.S. Shubina, *New types of hydrogen bonding in organometallic chemistry*. Coordination Chemistry Reviews, 2002. **231**(1-2): p. 165-181.
24. Epstein, L.M., et al., *Unusual hydrogen bonds with a hydride atom in boron hydrides acting as proton acceptor. Spectroscopic and theoretical studies*. Inorganic Chemistry, 1998. **37**(12): p. 3013-3017.
25. Shubina, E.S., et al., *Intermolecular hydrogen bonds BH center dot center dot center dot HX in solution*. Mendeleev Communications, 1997(2): p. 83-84.
26. Filinchuk, Y. and H. Hagemann, *Structure and properties of NaBH4 center dot 2H(2)O and NaBH4*. European Journal of Inorganic Chemistry, 2008(20): p. 3127-3133.
27. Hallmeier, K.H., et al., *Investigation of Core Excited Quantum Yield Spectra of High Symmetric Boron-Compounds*. Spectrochimica Acta Part a-Molecular and Biomolecular Spectroscopy, 1981. **37**(12): p. 1049-1053.
28. Carboni, R., et al., *Coordination of boron and phosphorous in Borophosphosilicate glasses*. Applied Physics Letters, 2003. **83**(21): p. 4312-4314.
29. Fleet, M.E. and X. Liu, *Boron K-edge XANES of boron oxides: tetrahedral B-O distances and near-surface alteration*. Physics and Chemistry of Minerals, 2001. **28**(6): p. 421-427.
30. Fleet, M.E. and S. Muthupari, *Boron K-edge XANES of borate and borosilicate minerals*. American Mineralogist, 2000. **85**(7-8): p. 1009-1021.
31. Fleet, M.E. and S. Muthupari, *Coordination of boron in alkali borosilicate glasses using XANES*. Journal of Non-Crystalline Solids, 1999. **255**(2-3): p. 233-241.
32. Kasrai, M., et al., *Surface modification study of borate materials from B K-edge X-ray absorption spectroscopy*. Physics and Chemistry of Minerals, 1998. **25**(4): p. 268-272.

33. Wilson, K.R., et al., *Investigation of volatile liquid surfaces by synchrotron x-ray spectroscopy of liquid microjets*. Review of Scientific Instruments, 2004. **75**(3): p. 725-736.
34. Cappa, C.D., et al., *Revisiting the total ion yield x-ray absorption spectra of liquid water microjets*. Journal of Physics-Condensed Matter, 2008. **20**(20).
35. Wilson, K.R., et al., *X-ray spectroscopy of liquid water microjets*. Journal of Physical Chemistry B, 2001. **105**(17): p. 3346-3349.
36. Schwartz, C.P., et al., *On the importance of nuclear quantum motions in near edge x-ray absorption fine structure spectroscopy of molecules*. Journal of Chemical Physics, 2009. **130**(18).
37. Uejio, J.S., et al., *Effects of vibrational motion on core-level spectra of prototype organic molecules*. Chemical Physics Letters, 2008. **467**(1-3): p. 195-199.
38. Otkidach, D.S. and I.V. Pletnev, *Conformational analysis of boron-containing compounds using Gillespie-Kepert version of molecular mechanics*. Journal of Molecular Structure-Theochem, 2001. **536**(1): p. 65-72.
39. Schwarz, W.H.E., et al., *K-Shell Excitations of Bf<sub>3</sub>, Cf<sub>4</sub> and Mbf<sub>4</sub> Compounds*. Chemical Physics, 1983. **82**(1-2): p. 57-65.
40. Klooster, W.T., et al., *Study of the N-H center dot center dot center dot H-B dihydrogen bond including the crystal structure of BH<sub>3</sub>NH<sub>3</sub> by neutron diffraction*. Journal of the American Chemical Society, 1999. **121**(27): p. 6337-6343.
41. Suzuki, Y., D. Kaneno, and S. Tomoda, *Theoretical Study on the Mechanism and Diastereoselectivity of NaBH<sub>4</sub> Reduction*. Journal of Physical Chemistry A, 2009. **113**(11): p. 2578-2583.

## Chapter 4: Conclusion

Section 1 of Chapter 2 presents a proof of principle study for the production and characterization of hydrogen from liquid jet electrokinetic streaming currents. Water, rapidly flowing water past a metal-water interface, entrains hydrated protons from the electric double layer and neutralization of the entrained protons at a downstream electrode produces molecular hydrogen. The streaming currents and hydrogen production both scale nearly quadratically with flow rate, as predicted by a relatively simple streaming current equation, derived from the overlap of the fluid velocity profile and an anisotropic charge distribution. Given that the streaming currents are in the nanoamp range, the conversion efficiency of the hydrogen production is only ca. 10-6.

Future experiments seeking to optimize hydrogen production from liquid microjets should focus on eliminating the spikes of hydrogen resulting from ice buildup in the jet chamber. Various schemes could be devised to heat the downstream target electrode that also keeps water from the analysis chamber. Since charge separation only occurs in the water-metal interfacial region, it would also be worthwhile to adjust the geometry of the jet aperture in order to maximize the surface to volume ratio.

Section 2 of Chapter 2 presented an exploration of electrical energy conversion efficiency experiments with liquid water microjets. Because liquid microjets break up into a droplet train before reaching the downstream electrode, both surface and bulk conduction of ions against the liquid flow is impossible. Consequently, the conversion efficiency is greatly enhanced compared to other techniques and is measured at over 10%.

Of course, the electrical conversion efficiency would also benefit from geometry optimization of the jet. An interesting experiment would test jet aperture geometries with the same nominal area, but with different perimeters. Ultrathin channels would have the greatest surface-to-volume ratio and ability to separate charge, but they would also require more energy in the form of backing pressure to operate. Parameters for optimal conversion efficiency would balance the surface-to-volume and backing pressure. Another untested hypothesis is that channels act independently and energy conversion scales linearly with the number of channels. The research conducted up to this point has only dealt with single apertures and it is unclear whether or not the charge separation process in one channel would affect the same process in an adjacent channel.

Hydrogen generation and conversion efficiency are both limited by the low (nanoamp) electrokinetic currents. Currents of this magnitude are prohibitively small for practical application, but the associated voltages are large (tens of kilovolts). The study presented in Part C of Chapter 2 represents attempts to exploit the high voltage and low current by coupling light into the electrokinetic process. Glass-silicon channels were fabricated to allow light to impinge on the electrokinetic surface and the light affected an increase the streaming current. A few channels even gave a positive response from the ambient room lights, although the research was hampered with inconsistent results.

Future work on photoelectrokinetics should employ a water-stable surface. The silicon channels used in the initial experiments were prone to oxidation and eventual collapse or rupture. Creating the channel out of an semiconducting oxide, such as  $\text{TiO}_2$ , or depositing an optically thin layer of metal on the semiconductor would protect against corrosion and offer a more stable platform to measure photoelectrokinetic phenomena. It would also be interesting to more definitively ascertain where the electrokinetic currents are produced. The experiments gave increases in the streaming current based on illumination at the channel aperture. However, the charge was actually measured well upstream from the aperture. Patterning the electrokinetic surface to create a grid, whereon the current could be read from individual pixels, would give very detailed information concerning the physical location of electrokinetic current generation.

Another area explored in this thesis research is photoelectrokinetic interfacial spectroscopy. Rather than changes in electrokinetic current induced by absorption of light at a semiconductor interface, photoelectrokinetic spectroscopy would monitor changes in electrokinetic current as affected by optical absorption of a species in the electric double layer. Absorption of light by a molecule or ion can transfer an electron from the molecule to the solvent. Such transitions in the bulk liquid would likely recombine and go undetected. However, a charge-transfer-to-solvent absorption in the electric double layer could alter the streaming current. Consequently, by monitoring the electrokinetic current, an absorption spectrum that would be inherently surface sensitive could be measured.

The first section of Chapter 3 presented experimental and theoretical NEXAFS results for hydrated boric acid, borate ion, and a few polyborate ions. Despite the fact that the boric acid/borate acid/base pair is connected through a reaction with water and that these oxides are terminated with hydroxide moieties, the experimental and theoretical results indicate that they are not strongly associated with water. Spectra of boric acid yield no observable change in the pre-edge feature between solvated and solid boric acid. Molecular dynamics simulations of these systems suggest that water arranges itself isotropically around these oxides, similar to the case of hydrophobic systems. These results correlate with the tendency of boron-oxides to collapse into polyborate ions in solution.

Further information about the boric acid/borate system could be gained by collecting boron K-edge NEXAFS spectra on boric acid solutions at low concentrations. Comparing spectra from a series of concentrations may reveal features that change based on condensation into polyborate clusters. To help interpret the experimental spectra, it would be helpful to run molecular dynamics simulations and XCH calculations on systems with multiple boric acid monomers in solution. Furthermore, molecular dynamics simulations using a level of theory in which the boric acid monomers were allowed to react could lead to a better understanding of the acid/base reaction as well as polyborate ion formation.

NEXAFS spectra and calculations of sodium borohydride, presented in Section 2 of Chapter 3, are quite distinct from the results for boron-oxides. The spectral changes in

this case, a shift to lower energy and narrowing of the features, are directly related to the formation of strong dihydrogen ( $\text{H}\cdots\text{H}$ ) bonds between water and borohydride. The dihydrogen bonds weaken the B-H bonds of the borohydride, repel the antibonding orbitals to a lower energy, and, consequently, the NEXAFS peak shifts to lower energy. Molecular dynamics simulations of the sodium borohydride-water system suggest that water mainly coordinates to the borohydride along the tetrahedral corners and edge.

Future work regarding borohydride hydration should focus on characterizing the still unexplained feature at 198 eV. The QM/MM calculations used heretofore, retain a boundary between the borohydride and the surrounding water that does not allow for electron transfer between the two. Considering the reaction between borohydride and water, this represents a serious limitation and calculations at a higher level of theory, e.g. DFT-based, would greatly improve the accuracy of the simulations. Experimentally, it would be interesting to follow the hydrolysis reaction as a function of time. Sodium borohydride is stable for years in basic solution, but reacts almost instantly in acidic solutions. The rate of the hydrolysis reaction is a sensitive function of pH and there should be a convenient pH that would allow the reaction to be followed with liquid microjet techniques. Mixing borohydride with an acidic solution immediately prior to liquid jet formation should allow the hydrolysis reaction to proceed while the jet is in vacuum. Probing the jet at different distances from the nozzle may allow one to follow the reaction for borohydride to boron-oxide.